Università degli Studi di Parma
Dipartimento di Ingegneria Civile,
dell'Ambiente, del Territorio e Architettura

Dottorato di Ricerca in Ingegneria Civile (XXVIII ciclo)
Curriculum: Protezione Idraulica del Territorio

Susanna Dazzi

Numerical modelling of unsteady mixed flow

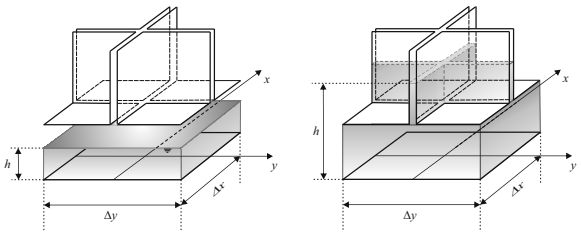

Dissertazione per il conseguimento del titolo di Dottore di Ricerca

Tutor: Dott. Andrea Maranzoni
Co-tutor: Prof. Paolo Mignosa
Coordinatore del Dottorato: Prof. Gianfranco Forlani

Parma, Gennaio 2016

Abstract

This thesis concerns mixed flows (which are characterized by the simultaneous occurrence of free-surface and pressurized flow in sewers, tunnels, culverts or under bridges), and contributes to the improvement of the existing numerical tools for modelling these phenomena. The classic Preissmann slot approach is selected due to its simplicity and capability of predicting results comparable to those of a more recent and complex two-equation model, as shown here with reference to a laboratory test case. In order to enhance the computational efficiency, a local time stepping strategy is implemented in a shock-capturing Godunov-type finite volume numerical scheme for the integration of the de Saint-Venant equations. The results of different numerical tests show that local time stepping reduces run time significantly (between -29% and -85% CPU time for the test cases considered) compared to the conventional global time stepping, especially when only a small region of the flow field is surcharged, while solution accuracy and mass conservation are not impaired. The second part of this thesis is devoted to the modelling of the hydraulic effects of potentially pressurized structures, such as bridges and culverts, inserted in open channel domains. To this aim, a two-dimensional mixed flow model is developed first. The classic conservative formulation of the 2D shallow water equations for free-surface flow is adapted by assuming that two fictitious vertical slots, normally intersecting, are added on the ceiling of each

integration element. Numerical results show that this schematization is suitable for the prediction of 2D flooding phenomena in which the pressurization of crossing structures can be expected. Given that the Preissmann model does not allow for the possibility of bridge overtopping, a one-dimensional model is also presented in this thesis to handle this particular condition. The flows below and above the deck are considered as parallel, and linked to the upstream and downstream reaches of the channel by introducing suitable internal boundary conditions. The comparison with experimental data and with the results of HEC-RAS simulations shows that the proposed model can be a useful and effective tool for predicting overtopping and backwater effects induced by the presence of bridges and culverts.

Acknowledgements

Desidero innanzitutto ringraziare Andrea Maranzoni per la disponibilità e competenza con cui ha seguito e indirizzato il mio lavoro in questi tre anni. Un grazie va poi al Prof. Mignosa per il prezioso contributo, nonché a tutto il gruppo di ricerca di Idraulica e Costruzioni Idrauliche, in particolare a Renato, per il supporto ricevuto. Vorrei inoltre ricordare Roberta, Fausto, Paolo e gli altri dottorandi con cui ho condiviso questo percorso, che non mi hanno mai fatto mancare il loro sostegno. Infine, non posso non ringraziare i miei amici e la mia famiglia per la vicinanza e l'affetto che mi hanno sempre dimostrato.

I also would like to thank Prof. Tomáš Picek for kindly providing experimental measurements of the free-surface profiles used in Chapter 4.

Contents

List of Figures

List of Tables

List of Acronyms

1D, 2D, 3D	One-, Two-, Three-dimensional
2E	Two-equation
CFL	Courant-Friedrichs-Lewy
EL	Energy Line
GTS	Global Time Stepping
HGL	Hydraulic Grade Line
IBC	Internal Boundary Condition
LTS	Local Time Stepping
PS	Preissmann Slot
TPA	Two-component Pressure Approach
VOF	Volume of Fluid

Introduction

Mixed flows are characterized by the simultaneous presence of free-surface and pressurized flow, and potentially occur in sewers, tunnels, and other pipe systems. This is the case of storm water systems, where pressurization may occur when inflow due to intense rainfalls exceeds the pipe capacity. A correct prediction of surcharging events is of great importance for the design and maintenance of these hydraulic structures (Politano et al., 2007), given that damages and operational problems have been reported in some cases (Hamam and McCorquodale, 1982; Guo and Song, 1990, 1991; Li and McCorquodale, 1999; Zhou et al., 2002). Other notable situations involving mixed flows are pipe filling in water mains, flood propagation in culverted watercourses or under bridges, and transients induced by abrupt operations on hydraulic machineries or gates in pipe networks or in waste and supply pipes of hydroelectric plants.

The numerical modelling of mixed flows is not trivial. First, the two flow regimes are usually modelled by means of two different sets of governing equations (de Saint-Venant equations for free-surface flow, and water hammer equations for pressurized flow). Second, the celerity at which waves propagate inside each region of the flow field assumes values which span from a few meters per second (for free-surface flow) up to hundreds of meters per second (for pressurized flow).

This thesis aims at contributing to the improvement of the existing numerical

tools for mixed flows. Particular attention is devoted to the integration of potentially pressurized hydraulic structures in open channel domains, but also to the improvement in model efficiency.

In fact, among the problems related to mixed flow modelling, one which has never been given full consideration in the literature is the lack of computational efficiency that a mixed flow model presents if coupled with an explicit numerical scheme. This is due to the fact that, if the numerical simulations are performed with realistic pressure wave speeds, a very small computational time step must be adopted to fulfil the Courant-Friedrichs-Lewy (CFL) stability condition, while the allowable time step in the free-surface part of the flow field can be some orders of magnitude greater than the one calculated in the pressurized region. Hence, the application of a local time stepping strategy to mixed flow modelling is tested in this work. The performances of the local and global time stepping schemes are compared in terms of computational efficiency and solution accuracy.

Although mixed flows mainly occur in closed conduits, for which a one-dimensional (1D) approximation is suitable, the opportunity of coupling free-surface and pressurized flow can also be useful for modelling two-dimensional (2D) flooding phenomena in which the pressurization of bridges, culverts, and other crossing structures can be expected. In this thesis, the classic conservative formulation of the 2D shallow water equations for free-surface flows is adapted to mixed flows by assuming that two fictitious vertical slots, aligned along the two Cartesian plane directions and normally intersecting, are added on the ceiling of each integration element. Accordingly, flow regime transitions can be handled in a natural and straightforward way by using the same set of governing equations. After the validation, performed by simulating idealized tests with reference solution, the model is used to simulate the partial pressurization of an arch bridge as an example of real-field application.

Unfortunately, the proposed approach does not allow for the possibility of

bridge overtopping, not even if the slot height is limited and the current cell dimensions are restored above the slot. Indeed, the assumption of a uniform flow velocity over the cell does not hold in this case, since the pressure flow under the bridge or culvert may be totally separate from the flow over it. To overcome this problem, the possibility of integrating the shallow water equations with internal boundary conditions is considered in this work. However, only the case of 1D flow is tested at the moment. Numerical simulations of pressurization and overtopping processes through bridges and culverts are performed in order to test the model's reliability.

The thesis is structured as follows. Chapter 1 briefly reviews the current knowledge about mixed flows and presents the validation and comparison of two existing 1D mixed flow models. One of these models is also upgraded with the introduction of a local time stepping strategy, presented in Chapter 2. In Chapter 3 the 2D mixed flow model is presented and validated. Finally, Chapter 4 proposes a 1D model with internal boundary conditions that allow for bridge or culvert pressurization and overtopping. The main results and future prospects are summarized in the Conclusions.

Chapter 1

1D numerical modelling of mixed flows in pipes

1.1 Introduction

Over the last few decades, several researchers have shown interest in the analysis of mixed flows, from both experimental and numerical perspectives. Section 1.2 is dedicated to a brief literature review about mixed flow numerical modelling. Two different 1D models are then described in this chapter. Both derive from previous works, but their effectiveness in simulating a complex mixed flow phenomenon is here compared on the basis of a common data set. In particular, the benchmark test case presented by Aureli et al. (2015) is chosen for the models' validation. Both models are based on finite volume numerical schemes (e.g. Toro, 1999; LeVeque, 2002), often employed in the literature, in both open channel (e.g. Toro, 2001) and water hammer problems (e.g. Guinot, 2000; Hwang and Chung, 2002; Zhao and Ghidaoui, 2004), due to their shock-capturing property. The

application of Godunov-type methods is usual also for the simulation of mixed flows in storm sewers (e.g. Vasconcelos et al., 2006; León et al., 2009).

This chapter is derived in part from Aureli et al. (2015).

1.2 Literature Review

Different configurations may characterize the flow regime transition. In particular, Cardle et al. (1989) defined "negative" or "retreating" interface the transition wave that moves towards the pressurized region; in this case, the pipe is undergoing depressurization. On the other hand, if the transition wave moves towards the free-surface region, it is defined as a "positive" or "advancing" interface (the pipe is pressurizing). Moreover, pressurization may be either gradual or occur in the form of a pipe-filling bore (Wright et al., 2008); these pressurization patterns are also defined as "smooth" or "abrupt" (Ferreri et al., 2014a). Numerical schemes must be able to accurately resolve all types of discontinuities.

The numerical modelling of mixed flows is particularly challenging since the two flow regimes, although governed by the same basic physical principles (mass and momentum conservation), are traditionally described by two different sets of governing equations, namely the de Saint-Venant equations for open channel flow and water-hammer equations for pressurized flow. Hence, in theory, the two sets of equations must be somehow linked at flow regime interfaces.

Bousso et al. (2013) presented a critical literature review about this topic, where the models currently available are classified on the basis of the number of governing equations into single- and two-equation models. The former class includes methods that extend the effectiveness of the de Saint-Venant equations to the case of pressurized flow, while the latter comprises models that adopt open channel flow equations and pressurized flow equations in different portions of the domain and link them at the transition points.

The most widely used method that belongs to the category of single-equation models is the classic Preissmann slot (PS) approach, originally proposed by Cunge and Wegner (1964) according to a Preissmann suggestion, and later widely used in the literature (e.g. García-Navarro et al., 1994; Capart et al., 1997; Trajkovic et al., 1999; Kerger et al., 2011a) and in commercial software packages (e.g. DHI, 2002; HEC, 2010). This approach hypothesizes the presence of a fictitious narrow slot above the crown of the conduit. Thanks to this artifice, a surcharged flow is simulated as an open channel flow with the water surface located into the slot, and flow pressurization can be modeled on the basis of the open channel flow equations. In the case of surcharged flow, the slot induces an additional pressure head and increases the storage capacity of the closed structure, allowing both the fluid compressibility and the pipe deformability to be taken into account, albeit approximately. The PS model is described in detail in Section 1.3.

The main shortcoming of this method lies in its inability to handle sub-atmospheric pressures. This problem was addressed by Kerger et al. (2011a), through the adoption of a "negative" slot, i.e. the slot is exteded below the pipe crown when negative pressures need to be simulated. Moreover, the model is unable to handle air-water interactions and air pocket entrapment, thus it can only be used to perform one-phase simulations and is unsuitable if ventilated conditions are not assured and air pressurization effects cannot be neglected. However, in spite of its limitations, the Preissmann slot model is widely accepted for unsteady mixed flow modelling due to its overall intrinsic simplicity, and is often assumed as a reference model to assess the predicting capabilities of new mixed flow solvers (e.g. Vasconcelos and Wright, 2007).

Another model belonging to this class is the Two-component Pressure Approach (TPA) by Vasconcelos et al. (2006), which decouples hydrostatic pressure from surcharged pressure when the pipe is full. The fluid is assumed incompressible, but the pipe is allowed to expand or shrink under pressurized conditions; in

this way, sub-atmospheric pressures can be handled automatically, provided that ventilation conditions are specified. The original model was also modified to take into account the influence of the free-gas content on the estimate of acoustic wave speed (Vasconcelos and Marwell, 2011). Moreover, subsequent developments of the model include the entrapment of a single air pocket during transients (Vasconcelos and Wright, 2009; Trindade and Vasconcelos, 2013; Vasconcelos et al., 2015).

Both PS and TPA models, coupled with shock-capturing schemes, suffer from spurious post-shock oscillations which arise at pipe-filling bore fronts, due to the sudden jump in wave celerity. The stability of the numerical simulation may be compromised. The origin of this behaviour was analyzed by Vasconcelos et al. (2009), and different strategies were proposed to overcome this limitation, including numerical filtering and using a hybrid flux scheme. Other authors assume low pressure wave celerity values (e.g. Capart et al., 1997; Trajkovic et al., 1999), or gradual transitions between the pipe and the slot (León et al., 2009). More recently, Malekpour and Karney (2015) further investigated the origin of the numerical oscillations for the PS approach, and proposed a strategy to suppress them by enhancing the numerical viscosity in the vicinity of the flow regime transition.

Pressurized flow can also be treated without the approximations introduced for single-equation models, for example by employing shock-fitting techniques. Wiggert (1972) solved the free-surface flow by applying the Method of Characteristics (MOC), while treating the pressurized flow as plug flow; moreover, the two regimes were connected by means of mass and momentum equations, and the interface position was explicitely tracked. The model was validated by comparison with laboratory data and applied to simulate flow in a tail-race tunnel. Song et al. (1983) extended Wiggert's model, using the MOC for both flow regimes and making a distinction between the treatment of negative and positive surge fronts, and applied it for the simulation of a storm sewer system (Guo and Song, 1990).

Other notable works on interface tracking models include those of Fuamba (2002) and Politano et al. (2007). In particular, the latter introduced a special treatment to model gradual regime transitions, which are otherwise poorly described by shock-fitting models. All these models do not consider the air phase and become complex when several interfaces need to be tracked.

Noto and Tucciarelli (2001) introduced a methodology to handle the transition between free-surface and pressurized flows in the DORA solver. This model neglects the inertial terms in the momentum equation, and is based on the decoupling of the solution into kinematic and diffusive components.

The rigid column theory can also be used to model mixed flow pressure transients (Li and McCorquodale, 1999). In this case, the entrapment and motion of a single air pocket undergoing compression and expansion can be taken into account.

Finally, Bourdarias and Gerbi (2007) recently introduced a novel dual model, which employs the finite volume method to solve the mass and momentum equations, written in conservative form, for both flow regimes. Due to its shock-capturing properties, the model automatically detects the wavefront position. A detailed description of this approach is presented in Section 1.4. A similar model was presented in León et al. (2010), where the entrapment and release of air pockets was also considered.

Numerical models are usually validated by comparison with reference solutions in order to assess their predictive capabilities. In the context of mixed flows, analytical solutions are available only for some simple theoretical test cases (see, for example, the exact solutions of the Riemann problem presented by Kerger et al., 2011b for the PS approach). Although valuable, these tests concern idealized situations characterized by frictionless horizontal conduits and elementary boundary conditions. The simulation of experimental cases represents a more realistic test. Laboratory studies of mixed flows have been conducted since the

early 1960s to provide data for the validation of numerical models (Wiggert, 1972; Trajkovic et al., 1999; Vasconcelos and Wright, 2005; Erpicum et al., 2009), as well as to improve the understanding of the physics of the transition phenomenon (e.g. Cardle et al., 1989; Ferreri et al., 2014b). Field data are particularly valuable for validation purposes but unfortunately they are seldom available. Some data concerning real events are reported in Guo and Song (1991), and in Trindade and Vasconcelos (2013).

The laboratory study of Wiggert (1972) is the basis of a benchmark test case that is still widely used in the literature. Experiments were performed in a rectangular flume whose central portion was provided with a roof in order to create a tunnel, and the opening of an upstream gate induced a transient pressurized flow in the culvert. Other authors equipped their laboratory devices with upstream and downstream sluice gates or weirs in order to generate hydraulic transients in circular pipes (e.g. Cardle et al., 1989; Li and McCorquodale, 1999; Capart et al., 1997; Trajkovic et al., 1999). The flow condition most frequently reproduced is generated by the sudden closure of a downstream gate (usually starting from steady conditions), which triggers a pipe filling bore; interface reversals were observed after the subsequent gate re-opening. Transients were also created by rapidly opening the downstream gate starting from pressurized conditions in the pipe (Cardle et al., 1989). In this case a negative interface appears. Other sets of experiments involve a rapid increase in the inflow discharge (Capart et al., 1997). Typically, pressure time series are acquired at instrumented sections while velocities are measured in few experimental studies only (e.g. Vasconcelos and Wright, 2005).

Reference test cases are generally a simplification of actual phenomena occurring in closed conduits, such as pump failures or start-ups and pipe filling due to intense rainfalls. Nevertheless, they are often considerably affected by the conditions imposed at the boundaries. In the Wiggert (1972) test case, for

example, depth measurements in the upstream and downstream reservoirs must be assumed as boundary conditions in numerical simulations. In other cases, gate manoeuvres must be somehow simulated (e.g. Trajkovic et al., 1999). The specification of correct information at the boundaries (such as inflow or outflow hydrographs, fixed-level reservoirs, and so on) is obviously crucial for accurate modelling of flow characteristics. A laboratory study which does not involve boundary conditions was presented by Aureli et al. (2015). The experimental set-up consisted of a V-shaped Plexiglas conduit whose upstream and downstream branches were characterized by positive and adverse slopes, respectively. A series of transitions from free-surface to pressurized flow and vice versa was observed in the device as a consequence of the water release caused by the sudden opening of a sluice gate placed along the upstream branch. In this way, mixed flow could be induced without imposing specific conditions at the pipe ends. This test case is used as a benchmark for model validation in this work.

A final brief remark must be dedicated to the fact that, in the experimental test case of Aureli et al. (2015), air inflow and outflow were allowed at the pipe ends in order to avoid entrapment of air pockets and air pressurization. The literature review confirms that many factors have a significant influence on the amplitude of the transient pressure pulses, first of all air entrapment (Cardle et al., 1989). In fact, the effect of the air phase cannot be neglected in rapidly filling tunnels unless adequate venting conditions are provided (Vasconcelos and Wright, 2005), and remarkable pressure oscillations may arise (Zhou et al., 2002). In many experimental works (e.g. Trajkovic et al., 1999; Vasconcelos et al., 2006) air–water interactions were not the subject of the investigation, and the interference of the air phase was then limited by installing suitable vents. Conversely, other works focused on the influence of air pocket entrapment and poor ventilation on hydraulic transients in rapidly filling pipes (e.g. Hamam and McCorquodale, 1982; Li and McCorquodale, 1999; Vasconcelos and Wright, 2009; Chosie et al., 2014);

the related experimental data were used for the validation of numerical models able to simulate the interaction between air and water (e.g. Zhou et al., 2002; Kerger et al., 2012; Trindade and Vasconcelos, 2013). In this work, however, only single-phase models are considered.

1.3 Preissmann slot model

1.3.1 The de Saint-Venant equations

Unsteady open channel flows are traditionally described by mass and momentum conservation laws, under the following assumptions (Cunge et al., 1980):

- the fluid is incompressible;
- the velocity is uniform over the cross-section and the water level across the section is horizontal (one-dimensional flow);
- the pressure distribution is hydrostatic (small streamline curvatures and negligible vertical accelerations);
- the channel bed slope is small;
- friction can be accounted for through steady-state resistance laws;
- the effect of viscosity and surface tension is negligible.

In vector conservative form the governing equations may be written as (e.g. Cunge et al., 1980):

$$\frac{\partial \mathbf{U}}{\partial t} + \frac{\partial \mathbf{F}}{\partial x} = \mathbf{S} \tag{1.1}$$

where x is the distance along the channel (positive downstream), t is time, $\mathbf{U}$, $\mathbf{F}$ and $\mathbf{S}$ are the vectors of conserved variables, of fluxes and of source terms

respectively:

$$\mathbf{U} = \begin{bmatrix} A \\ Q \end{bmatrix}, \quad \mathbf{F} = \begin{bmatrix} Q \\ \dfrac{Q^2}{A} + gI_1 \end{bmatrix}, \quad \mathbf{S} = \begin{bmatrix} 0 \\ gA(S_0 - S_f) + gI_2 \end{bmatrix}. \tag{1.2}$$

In Eq. (1.2) A is the flow area, Q is the flow discharge, g is the gravitational acceleration, I_1 is the hydrostatic pressure force term, defined as:

$$I_1 = \int_0^{h(x)} (h(x) - \eta)\, \sigma(x, \eta)\, \mathrm{d}\eta \tag{1.3}$$

where h represents the water depth, and $\sigma(x, \eta)$ is the cross-sectional width at elevation η above the bottom. Moreover, $S_0 = -\mathrm{d}z_b/\mathrm{d}x$ is the bottom slope (z_b is the bottom elevation), and S_f is the friction slope, which may be evaluated as:

$$S_f = n_m^2 \frac{u|u|}{R_h^{4/3}} \tag{1.4}$$

where n_m is Manning's roughness coefficient, u is the cross-sectional average velocity, and R_h is the hydraulic radius. Finally, the term I_2 takes into account the channel width variation along x (which is null for prismatic channels), and is defined as:

$$I_2 = \int_0^{h(x)} (h(x) - \eta)\, \frac{\partial \sigma(x, \eta)}{\partial x}\, \mathrm{d}\eta. \tag{1.5}$$

This term is neglected in the following.

1.3.2 Extension to pressurized flows

Equation (1.1), coupled with statements (1.2), is used for the simulation of free-surface flows not only in rivers and channels, but also in sewers and other conduit systems as long as the water depth is not expected to reach the pipe crown. When the flow becomes pressurized, the de Saint-Venant equations can

still be employed if the Preissmann slot (PS) approach is adopted (Cunge and Wegner, 1964). The cross-sectional geometry is modified through the introduction of a fictitious narrow vertical slot above the top of the closed conduit (Fig. 1.1). In pressurized conditions, the water depth exceeds the pipe crown and represents the pressure head with reference to the bottom. Provided that small slot widths are chosen, the water volume stored in the slot is negligible, and the mass balance is not significantly affected (Cunge et al., 1980).

For a circular pipe of diameter D, the geometrical relations for the new composite cross-section can be synthetized as follows:

$$A = \begin{cases} \dfrac{D^2}{8}\left(\theta - \sin\theta\right) & \text{if } h < D \\ A_{\max} + \left(h - D\right) T_s & \text{if } h \geq D \end{cases} \tag{1.6a}$$

$$b = \begin{cases} D \sin\left(\dfrac{\theta}{2}\right) & \text{if } h < D \\ T_s & \text{if } h \geq D \end{cases} \tag{1.6b}$$

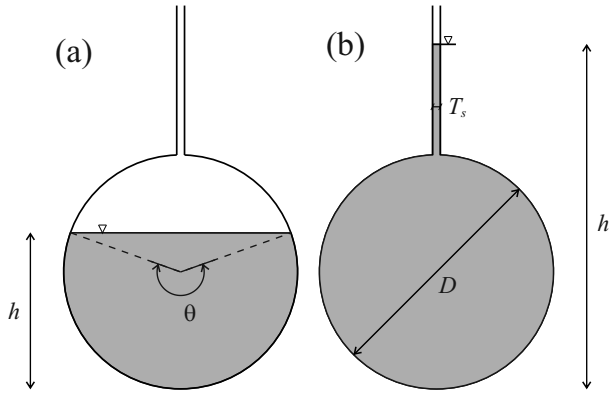

FIGURE 1.1 – Sketch of a circular cross-section with the Preissmann slot

$$P = \begin{cases} \dfrac{D}{2}\theta & \text{if } h < D \\ \pi D & \text{if } h \geq D \end{cases} \tag{1.6c}$$

$$R_h = \frac{A}{P} = \begin{cases} \dfrac{D}{4}\left(1 - \dfrac{\sin\theta}{\theta}\right) & \text{if } h < D \\ \dfrac{D}{4} & \text{if } h \geq D \end{cases} \tag{1.6d}$$

$$I_1 = \begin{cases} \dfrac{D^3}{24}\left[3\sin\left(\dfrac{\theta}{2}\right) - \sin^3\left(\dfrac{\theta}{2}\right) - 3\left(\dfrac{\theta}{2}\right)\cos\left(\dfrac{\theta}{2}\right)\right] & \text{if } h < D \\ A_{\max}\left(h - \dfrac{D}{2}\right) + T_s\dfrac{(h-D)^2}{2} & \text{if } h \geq D \end{cases} \tag{1.6e}$$

$$c = \sqrt{\frac{gA}{b}} = \begin{cases} \sqrt{\dfrac{gD\,(\theta - \sin\theta)}{8\sin(\theta/2)}} & \text{if } h < D \\ \sqrt{\dfrac{gA}{T_s}} & \text{if } h \geq D \end{cases} \tag{1.6f}$$

In Eq. (1.6), $A_{\max}$ is the full pipe cross-sectional area, P is the wetted perimeter (note that the slot is not accounted for in its computation), b is the free-surface width, T_s is the slot width, c is the speed of gravity waves, and θ is the wetted angle, which depends on the water depth h:

$$\theta = 2\arccos\left(1 - 2\frac{h}{D}\right). \tag{1.7}$$

Actually, the transition from free-surface to pressurized flow is assumed to take place for a slightly smaller water depth than the pipe diameter, precisely at the value corresponding to a free-surface width equal to the slot width. This approximation avoids division by zero in the celerity evaluation when the water surface reaches the pipe crown, and does not sensibly affect mass conservation, due to the minimal reduction in the pipe area. Some authors (e.g. León et al., 2009) even introduce a smooth transition between the pipe crown and the slot, so that the celerity value increases gradually from free-surface to pressurized flow.

Similar relations can be obtained for other cross-sectional shapes, e.g. rectangular, elliptical, etc.

1.3.3 Slot width

Pressure waves propagate as gravity waves when the PS approach is used, hence, in order to model the physics of the phenomenon correctly, the slot width T_s should be set in such a way that the speed of gravity waves c equals the pressure wave speed a, according to the relation:

$$T_s = \frac{gA}{a^2}\,. \tag{1.8}$$

In practical applications, pressure wave speed depends on many factors, including fluid compressibility, pipe deformability, and also air entrainment. In particular, the presence of air may lead to considerable uncertainties in the definition of this value. If high frequency pressure fluctuations or water hammer transients need to be modelled, the slot width should be set according to Eq. (1.8), giving a the value of the physical pressure wave speed. However, this constraint generally leads to the estimate of very narrow slots, which on the one hand ensure negligible mass error and correct pressure wave speed computation, but on the other hand induce spurious numerical oscillations at flow regime transitions if shock-capturing schemes are used (Vasconcelos et al., 2009), and also reduce the allowable time step for stability if explicit schemes are used (thus increasing the computational time).

To overcome this problem, some authors (e.g. Trajkovic et al., 1999; DHI, 2002) set the slot width at $1 - 2\%$ of the pipe diameter, accepting a significant reduction in the pressure wave celerity value, but still obtaining satisfactory results in the simulation of experimental test cases.

The influence of the slot width on the propagation speed of transition bores

can be assessed considering a simple test case with analytical solution. Let us consider a square pipe (1 m × 1 m), where two uniform free-surface flows with the same water depth but opposite velocities collide. The impingement of the two incoming flows produces a pressurized intermediate state which expands thanks to two transition shock waves traveling in opposite directions. If only one half of the domain is considered, this situation is equivalent to the propagation of a pipe-filling surge originated by the sudden closure of the downstream end of a conduit. The domain is $[-10, 10]$ m.

In Fig. 1.2, the analytical profiles of pressure head at $t = 1$ s, obtained from the exact Riemann solver of Kerger et al. (2011b) using different values of the slot width ($T_s/B = 0.10$, 0.02, 0.01, 0.004, 0.001, and 0.0001), are compared for the case of a high initial filling ratio ($h/D = 0.8$) and velocity u equal to 2 m/s. In particular, Table 1.1 shows the influence of the Preissmann slot width on the accuracy of the exact solver in predicting the pressure head $h^\star$ in the intermediate (star) region, as well as the shock wave speed $S^\star$. Errors are computed with reference to the solution obtained with the narrowest slot. The introduction of the Preissmann slot, due to the additional volume made available, noticeably affects both the propagation speed and the strength of the reflected surge: in fact, wave celerity and jump height decrease with the increasing of the slot width. The Preissmann slot model seems capable of accurately describing the propagation of the transition wave as long as the slot is narrow enough to guarantee that the water volume contained within the slot is negligible. In this work, a dimensionless slot width equal to 0.01 is then preferably assumed, as a reasonable compromise between accuracy and computational stability.

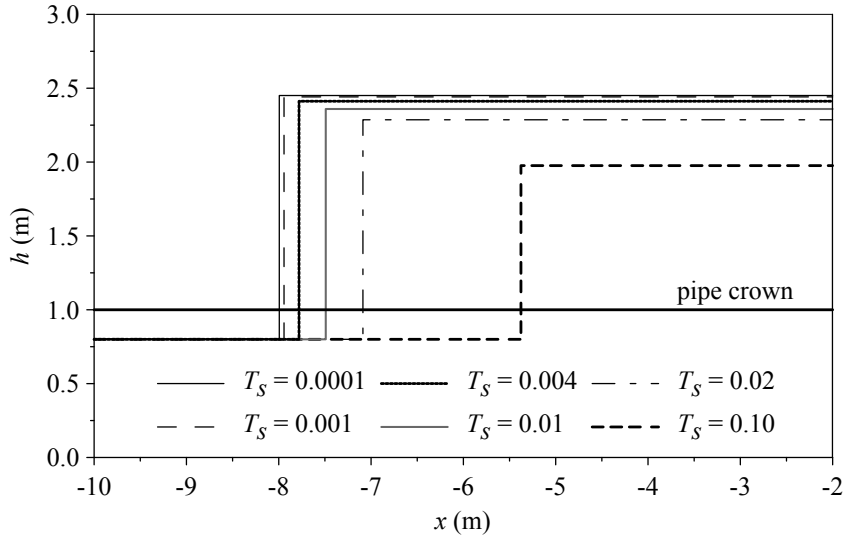

FIGURE 1.2 – Analytical solutions for pressure head at $t = 1$ s calculated with different values of the slot width

TABLE 1.1 – Errors on pressure head and propagation speed of the bore for the analytical test case, calculated with different values of the slot width

T_s/D	a(m/s)	$\Delta h^\star$(%)	$\Delta S^\star$(%)
0.10	10	−19.4	−32.7
0.02	22	−6.7	−11.3
0.01	31	−3.7	−6.3
0.004	50	−1.6	−2.7
0.001	100	−0.4	−0.6
0.0001	310	–	–

1.3.4 Numerical scheme

Equation (1.1) is discretized using an explicit, Godunov-type, first-order accurate, finite volume method. For the ith cell of length Δx, the solution is updated in the time step Δt according to the following expression:

$$\mathbf{U}_i^{n+1} = \mathbf{U}_i^n - \frac{\Delta t}{\Delta x}(\mathbf{F}_{i+1/2} - \mathbf{F}_{i-1/2}) + \Delta t\, \mathbf{S}_i \tag{1.9}$$

where $\mathbf{U}_i$ and $\mathbf{S}_i$ indicate cell-averaged values for the vector of the conserved variables and for the source term respectively, while $\mathbf{F}$ denotes the numerical flux at the interface between neighbouring cells. Superscripts n and $n+1$ refer to time levels t and $t + \Delta t$, respectively.

Numerical fluxes are estimated by solving the Riemann problem at each cell edge. The evaluation of the left and right states is performed through the reconstruction algorithm suggested by Sanders and Bradford (2011) and originally applied to a TPA-based model. For the $i + 1/2$ interface:

$$\begin{aligned} h_L &= h_i + \frac{1}{2}\Delta h_i \qquad & Q_L &= Q_i \\ h_R &= h_{i+1} - \frac{1}{2}\Delta h_{i+1} & Q_R &= Q_{i+1} \end{aligned} \tag{1.10}$$

For wet cells, the change of h inside the ith cell is calculated as:

$$\Delta h_i = \begin{cases} 0 & \text{if } s_i \geq s^\star \\ -\dfrac{\Delta z_i}{2}\left[1 + \cos\left(\pi \dfrac{s_i}{s^\star}\right)\right] & \text{if } s_i < s^\star \end{cases} \tag{1.11}$$

where $\Delta z_i = z_{i+1/2} - z_{i-1/2}$, s_i is the ratio of friction to bottom slope, and $s^\star$ is a critical value, set equal to 0.01 in this work. On the basis of the ratio $s_i/s^\star$, it is therefore decided whether a piecewise constant or a piecewise linear water depth reconstruction (assuring constant free-surface elevation) is performed. According

to Sanders and Bradford (2011), a cell should be considered as "wet" if $s_i/s^\star > 1$ or if the cell-averaged value of the flow area A, which represents the volume stored in the computational cell, exceeds the minimum value to submerge both cell vertices. For a dry cell, as well as for a wet cell in water at rest condition, $s_i = 0$, and thus $\Delta h_i = -\Delta z_i$; in this case, the momentum equation is not updated.

The HLL approximate Riemann solver (Toro, 2001) is used for flux evaluation at cell interfaces:

$$\mathbf{F} = \begin{cases} \mathbf{F}_L & \text{if } S_L > 0 \\ \dfrac{S_R\mathbf{F}_L - S_L\mathbf{F}_R + S_L S_R(\mathbf{U}_R - \mathbf{U}_L)}{S_R - S_L} & \text{if } S_L \leq 0 \leq S_R \\ \mathbf{F}_R & \text{if } S_R < 0 \end{cases} \tag{1.12}$$

Wave speeds S_L and S_R are estimated according to León et al. (2006, 2009):

$$\begin{aligned} &S_L = u_L - M_L, \;\; S_R = u_R + M_R \\ &M_K = \begin{cases} c_K & \text{if } A^\star \leq A_K \\ \sqrt{\dfrac{g(I_1^\star - I_{1,K})A^\star}{A_K(A^\star - A_K)}} & \text{if } A^\star > A_K \end{cases} \end{aligned} \tag{1.13}$$

with $K = L, R$. For the intermediate (starred) state, different estimates are available in the literature. Those based on the two-rarefaction wave approximation and the depth-positivity condition (Toro, 2001; León et al., 2006) are employed in this work. In the case of wet-dry interfaces, wave speeds are estimated exactly as follows:

$$\begin{aligned} &S_L = u_L - c_L, \quad S_R = u_L + \phi_L, \quad \text{if the right side is dry,} \\ &S_L = u_R - \phi_R, \quad S_R = u_R + c_R, \quad \text{if the left side is dry.} \end{aligned} \tag{1.14}$$

The variable ϕ is defined as $\int (c/A) dA$ and derives from the definition of the

Riemann invariants for circular pipes (León et al., 2006).

The treatment of source terms is accomplished according to Sanders and Bradford (2011). The bottom slope source term is treated explicitly and is calculated as:

$$(gAS_0)_i^n = -\frac{1}{\Delta x}\, g \left[I_1\left(h_i + \frac{1}{2}\Delta z_i\right) - I_1\left(h_i - \frac{1}{2}\Delta z_i\right)\right] \tag{1.15}$$

to ensure that the C-property (i.e. the ability of the scheme to preserve a stationary condition in a non-horizontal pipe) is satisfied. On the other hand, the friction slope source term is treated implicitly as follows:

$$(S_f)_i^{n+1} = n_m^2 \, \frac{Q_i^{n+1}|Q_i^n|}{(A_i^n)^2\,(R_h^n)_i^{4/3}} \tag{1.16}$$

in order to prevent unphysical flow inversions induced by flow resistance. Finally, the update expression for the flow rate is:

$$\begin{aligned} Q_i^\star &= Q_i^n - \frac{\Delta t}{\Delta x}(\mathbf{F}_{i+1/2} - \mathbf{F}_{i-1/2}) + \Delta t\ (gAS_0)_i^n \\ Q_i^{n+1} &= Q_i^\star \left[1 + \Delta t \frac{g n_m^2 |Q_i^n|}{A_i^n\,(R_h^n)_i^{4/3}}\right]^{-1}. \end{aligned} \tag{1.17}$$

Being explicit, the numerical scheme is stable provided that the CFL condition is fulfilled, that is:

$$Cr = \frac{\lambda\,\Delta t}{\Delta x} \leq 1 \tag{1.18}$$

where Cr is the Courant number and λ is the maximum wave speed along the pipe. Boundary conditions are implemented on the basis of the ghost cell approach (LeVeque, 2002).

1.4 Two-equation model

1.4.1 Mathematical model

Bourdarias and Gerbi (2007) proposed a conservative formulation of the governing equations for unsteady pressurized flow in a rigid prismatic conduit, which formally appear equivalent to the de Saint-Venant equations for open channel flow. Assuming a compressible flow, the authors introduced a new set of conserved variables: the equivalent wet area $A_{eq} = A_{\max}\,\rho/\rho_0$ and the equivalent discharge $Q_{eq} = Q\,\rho/\rho_0$, where ρ and ρ_0 are the density values at pressure p and at atmospheric pressure p_0, respectively. Pressure and density are linked by the classic Boussinesq pressure law:

$$p = p_0 + a^2\,(\rho - \rho_0). \tag{1.19}$$

The new conserved variables A_{eq} and Q_{eq} obviously reduce to A and Q in the case of incompressible free-surface flow. In this way, Eq. (1.1) defines a two-equation (2E) dual model which combines the de Saint-Venant equations and the compressible water hammer equations, provided that the following statements are introduced for the vector of conserved variables, the flux vector, and the source term:

$$\mathbf{U} = \begin{bmatrix} A_{eq} \\ Q_{eq} \end{bmatrix}, \quad \mathbf{F} = \begin{bmatrix} Q_{eq} \\ \dfrac{Q_{eq}^2}{A_{eq}} + I \end{bmatrix}, \quad \mathbf{S} = \begin{bmatrix} 0 \\ gA_{eq}(S_0 - S_f) \end{bmatrix}. \tag{1.20}$$

The pressure term I depends on the flow regime and is written:

$$I = \begin{cases} g\,I_1(A_{eq}) & \text{if free-surface,} \\ g\,I_1(A_{\max}) + a^2\,(A_{eq} - A_{\max}) & \text{if pressurized.} \end{cases} \tag{1.21}$$

The pressure term is a continuous function of the equivalent area, yet it is characterized by abrupt discontinuity in the derivative at the transition point (for $A_{eq} = A_{\max}$). This feature, along with the strong discontinuity in the wave celerity value, is probably the main reason for the numerical instabilities that arise when pipe filling bore fronts, causing the sudden transition between the two flow regimes, are modelled by shock-capturing schemes (Vasconcelos et al., 2009). It is to be noted that this model is automatically capable of handling sub-atmospheric pressures (León et al., 2010), provided that ventilation conditions are specified. The same formulation of the governing equations was adopted by León et al. (2010, 2013).

1.4.2 Numerical scheme

Equation (1.1), coupled with statements (1.20), is numerically solved by using the same finite volume scheme described in Section 1.3.4, the only exception being few numerical details concerning the flux evaluation. For free-surface flow, the HLL solver is still used, whereas for pressurized flow the approximate solver suggested by León et al. (2008) is employed. In this latter case, the physical flux $\mathbf{F}(\mathbf{U}^\star)$ is computed at the intercells according to Eq. (1.20), and the intermediate state $\mathbf{U}^\star$ is estimated as follows (the subscript eq is dropped for simplicity):

$$\begin{aligned} A^\star &= \left(\frac{A_L + A_R}{2}\right)\left(1 + \frac{u_L - u_R}{c_L + c_R}\right) \\ Q^\star &= Q_L + \left(\frac{u_L + u_R}{2} - \frac{c_L + c_R}{2}\right)(A^\star - A_L). \end{aligned} \tag{1.22}$$

Finally, a special flux treatment is required at free-surface/pressurized flow interfaces, as suggested by Bourdarias and Gerbi (2007). According to this method, the interface is considered as a shock wave, and Rankine-Hugoniot conditions are imposed across the wave, coupled with closure relations, which may represent

characteristic equations, Riemann invariants, or energy balances, depending on the type of interface and wave pattern. The resulting non-linear system must be solved iteratively. For more details, the reader is referred to the original paper.

1.5 Validation

1.5.1 Laboratory test case

The laboratory test case used for the validation and comparison of the two models is described in Aureli et al. (2015). The experiments were carried out in the facility sketched in Fig. 1.3, which was set up at the Hydraulics Laboratory of the University of Parma. It consisted of a 12 m long Plexiglas pipeline with 0.192 m inner diameter. At approximately 7 m from the upstream end, the pipe slope changed abruptly from about 8.4% (downward) to about −27.7% (upward). A sluice gate (orthogonal to the pipe axis) was placed approximately 5 m downstream of the upper end of the device. The gate could be almost instantaneously lifted by means of a simple manhandled pulley system. Aeration was guaranteed at both pipe ends, hence air entrapment does not influence the phenomenon. Pressure and velocity measurements were performed by non-intrusive techniques at the cross-sections indicated in Table 1.2.

The sluice gate retained still water upstream, with a pressure head of 0.225 m at

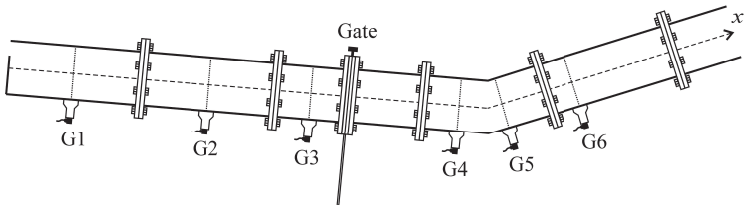

FIGURE 1.3 – Sketch of the laboratory set-up

gauge G1, while the conduit was initially dry downstream. The sudden removal of the gate triggered a rapid transient, whose main stages are qualitatively represented in Fig. 1.4. Immediately after the gate opening, a wetting front propagated in the downstream conduit, while gauges from G1 to G3 (located upstream of the gate) registered a rapid depressurization. At approximately $t = 1\,\mathrm{s}$, the wetting front reached the slope reversal, and free-surface regime occurred everywhere (Fig. 1.4a). At about $t = 2\,\mathrm{s}$, the wetting front reached gauge G6, and, immediately after, the run-up of the wave in the counter-sloped branch induced partial pressurization of the pipe and the formation of a positive transition wave travelling upstream (Fig. 1.4b). Between $t = 3\,\mathrm{s}$ and $t = 8\,\mathrm{s}$ (Fig. 1.4c) the advancing shock wave kept moving and involved all the upstream gauges, while the downstream portion of the pipe was subject to emptying. Then, a damped oscillatory flow developed in the device, with almost persistent pressurization of the three lowest gauges G3, G4, and G5. After $t = 8\,\mathrm{s}$, gauge G6 recorded free-surface water levels only, and after $t = 20\,\mathrm{s}$ the extreme upstream gauge G1 was no longer affected by wetting (Fig. 1.4d).

TABLE 1.2 – Location of the measuring gauges (x is the distance along the pipe axis)

Pressure gauges		Velocity gauges	
Gauge	x (m)	Gauge	x (m)
G1	1.00	V1	0.94
G2	3.00	V2	2.94
G3	4.50	V3	4.44
G4	6.80	V4	6.74
G5	7.32	V5	7.26
G6	8.52	V6	8.46

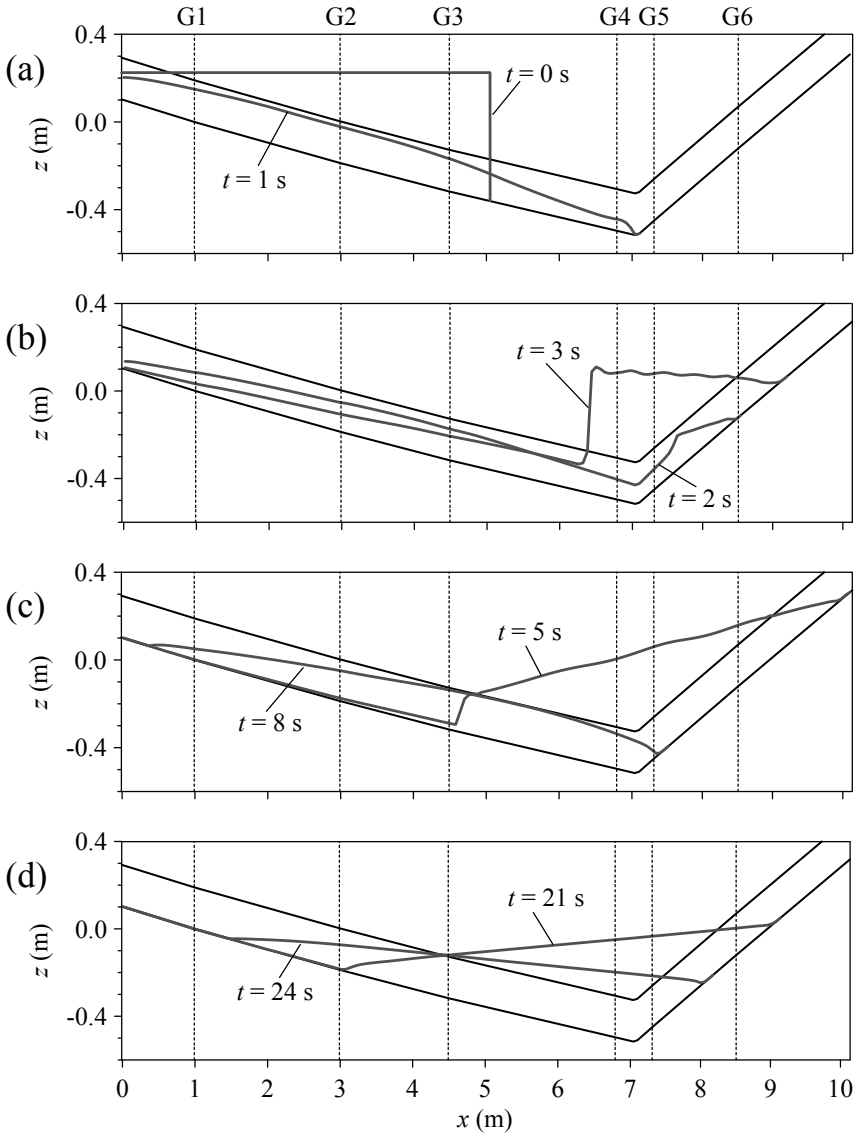

FIGURE 1.4 – Pressure head profiles for the laboratory test case. The variable x is the distance along the pipe. Elevation z is referred to the bottom of section G1

1.5.2 Simulation parameters

The experimental test case described in Section 1.5.1 is simulated by applying the two numerical models described in Sections 1.3 and 1.4. The computational domain is discretized by means of 300 grid cells (with grid spacing $\Delta x = 4$ cm), and the Courant number is set at 0.8. Manning's roughness coefficient is calibrated to correctly reproduce the observed arrival time of the wetting front at the downstream gauge sections, and is set at 0.009 $\mathrm{m}^{-1/3}\mathrm{s}$. In the PS model simulation, a slot width equal to 1% of the pipe diameter (corresponding to about 12 m/s pressure wave celerity) is adopted in order to prevent the numerical oscillations that typically arise at flow regime transitions when much larger wave celerity is assumed. This low value, although not representative of the actual pressure wave speed in the pipe (estimated to be in the order of 200 m/s) guarantees that post-shock oscillations do not sensibly deteriorate the quality of the numerical results. Accordingly, the same value of the pressure wave speed is adopted in the 2E model simulation. Simple reflective boundary conditions (Toro, 2001) are specified at both pipe ends.

1.5.3 Numerical results

Figures 1.5 and 1.6 compare numerical results and experimental measurements for the six pressure gauges G1-G6, while Figs. 1.7 and 1.8 show the same comparison for the six sections V1-V6, equipped with velocity gauges. It is noteworthy that the two models, despite the different approach used for coupling free-surface and pressurized flow regimes, give almost identical results. In general, both numerical methods reproduce the experimental data satisfactorily, in spite of the non-physical value assigned to the pressure wave speed. This fact was also observed by other authors on the basis of the numerical simulations of different experimental tests (e.g. Capart et al., 1997; Trajkovic et al., 1999; Ferreri et al.,

2010). The main consequence of the assumption of a reduced value for the pressure wave speed is recognizable at gauges G1 and G2 (Figs. 1.5a and 1.5b). The depressurization wave originated by the gate opening has been experimentally observed to arrive almost instantaneously at the upstream sections; conversely, the numerical results show a delay in the arrival time, and the initial state is maintained for about 0.2 s at the upstream limb of the reservoir (see the insert in Fig. 1.5a). However, the subsequent development of the phenomenon is excellently reproduced by both numerical models at gauges G1 and G2, where, except for the very first stages, the flow remains in free-surface regime. The temporal sequence of wetting and drying is also well caught. At section G3 (Fig. 1.5c), the closest to the gate, the numerical results do not exactly match the experimental measurements between $t = 0$ s and $t = 5$ s, and show a noticeable underestimation of the pressure head. Actually, as already highlighted in the literature (e.g. Ozmen-Cagatay and Kocaman, 2010; Shigematsu et al., 2004), 1D depth-integrated numerical models fail to correctly describe dam-break phenomena near the gate site immediately after the gate opening, due to their inability to handle strong curvatures with non-zero vertical velocity components. The correct prediction of this and other three-dimensional (3D) effects would require a detailed 3D simulation of the phenomenon.

At gauges G4 and G5 (Figs. 1.6a and 1.6b), sudden flow regime transitions can be observed at $t = 3$ s, when a pipe filling bore travelling upstream reaches these sections. The timing of the pressurization wave is correctly estimated by both numerical models, but small post-shock oscillations can be observed on the pressurized side of the interface (see, for example, the pressure head longitudinal profile at $t = 2.8$ s shown in Fig. 1.9). The pressure time series recorded at all the measuring sections exhibit a long-time damping oscillatory behaviour. During the long-time oscillations, sections G1, G2, and G6 remain in free-surface flow regime, G4 and G5 in pressurized flow regime, while G3 shows multiple smooth

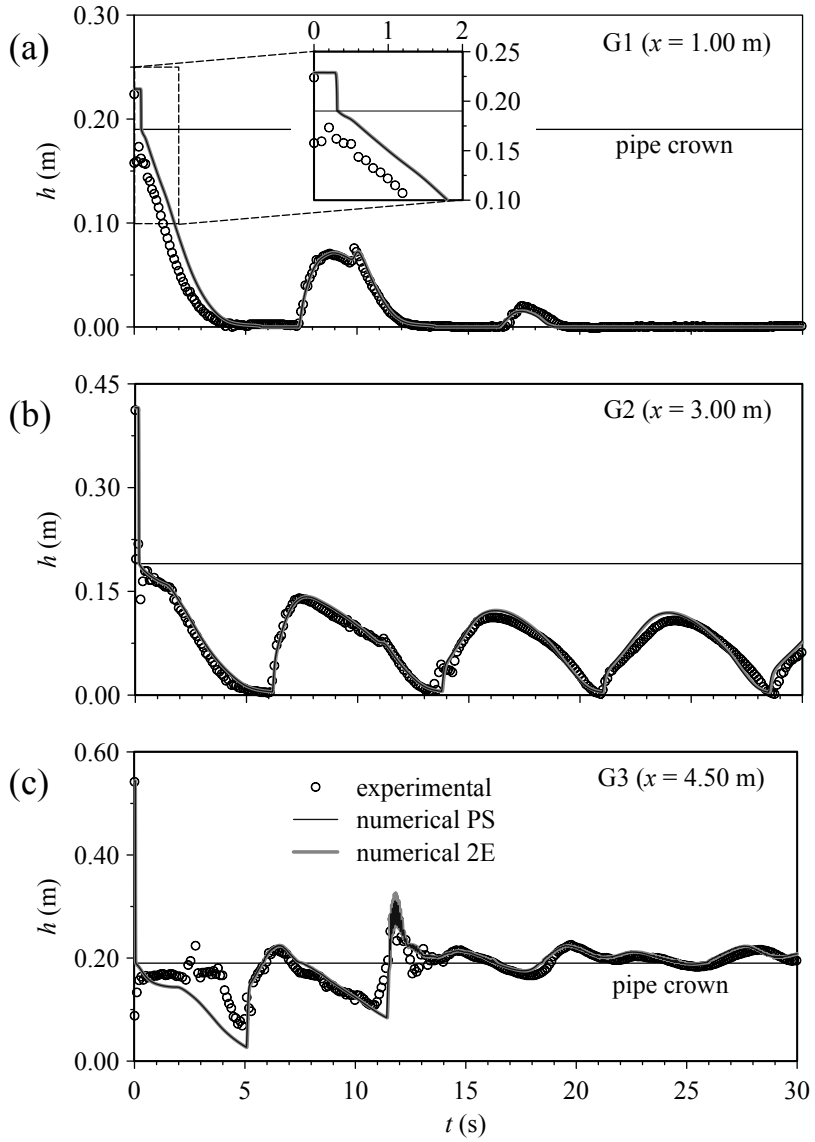

FIGURE 1.5 – Comparison between experimental and numerical pressure head time series at the measuring sections labelled G1, G2, and G3

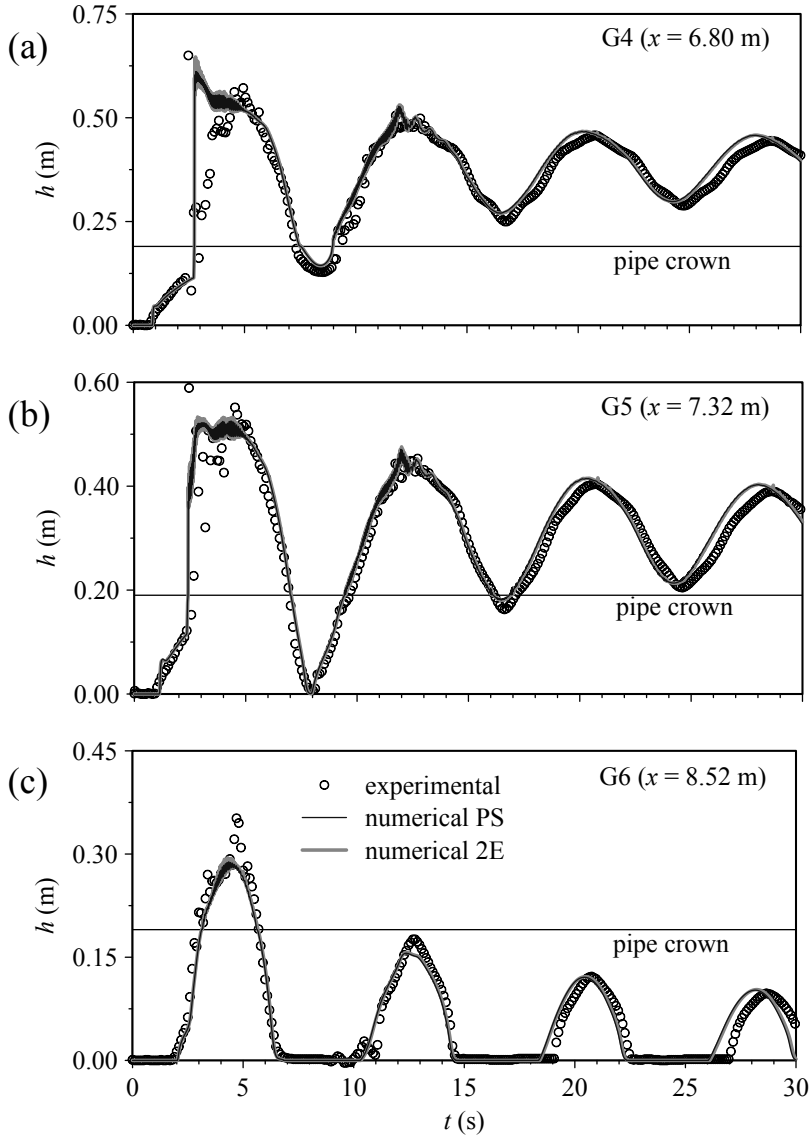

FIGURE 1.6 – Comparison between experimental and numerical pressure head time series at the measuring sections labelled G4, G5, and G6

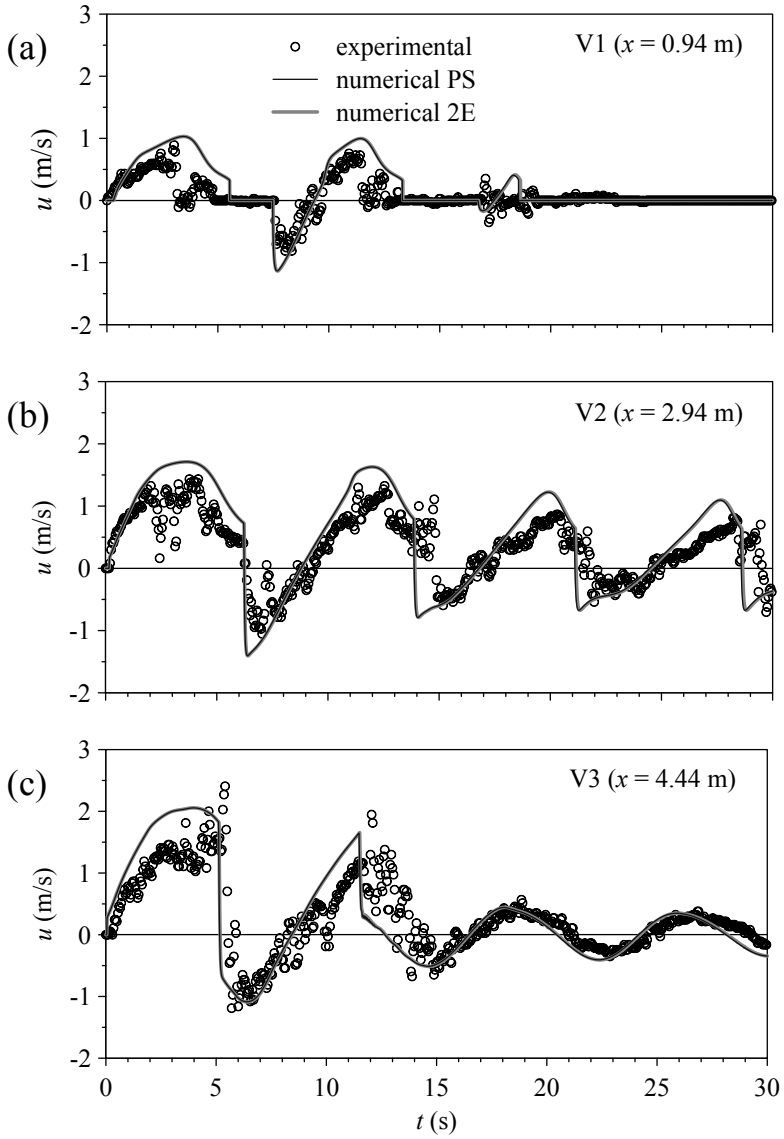

FIGURE 1.7 – Comparison between experimental and numerical velocity time series at the measuring sections labelled V1, V2, and V3

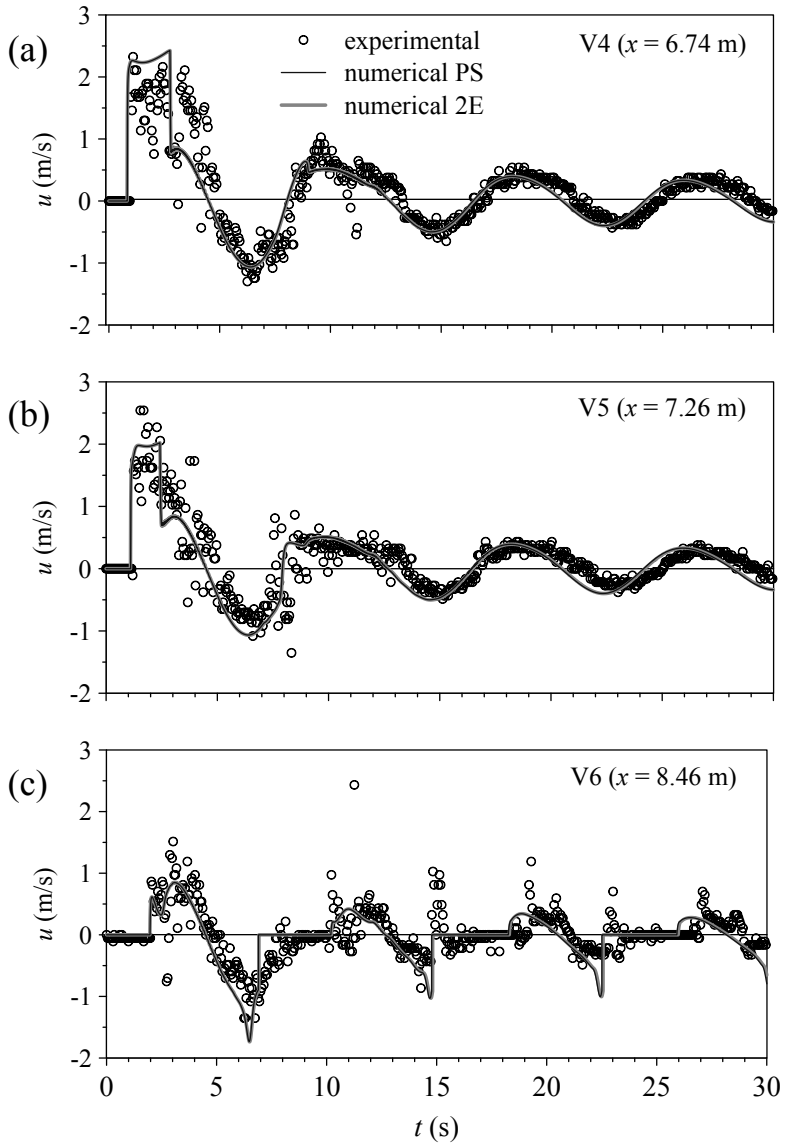

FIGURE 1.8 – Comparison between experimental and numerical velocity time series at the measuring sections labelled V4, V5, and V6

transitions, which are accurately captured by both numerical models. In the last phase of the oscillatory phenomenon, gauge G1 remains dry, whereas, at the other gauges, pressure head peaks are slightly overestimated and anticipated. This effect becomes more and more noticeable as time increases. This circumstance is probably referable partly to a slight underestimation of the long-time frictional effects due to the adoption of a steady friction model, and partly to the numerical diffusivity introduced by the first-order scheme.

As for velocity measurements, it must be noticed that the experimental data are characterized by scattering over the entire time interval under consideration (Figs. 1.7 and 1.8). Nevertheless, Figs. 1.7 and 1.8 show that the numerical models are able to satisfactorily reproduce the experimental data from a qualitative point of view, even if peak values are not always well captured.

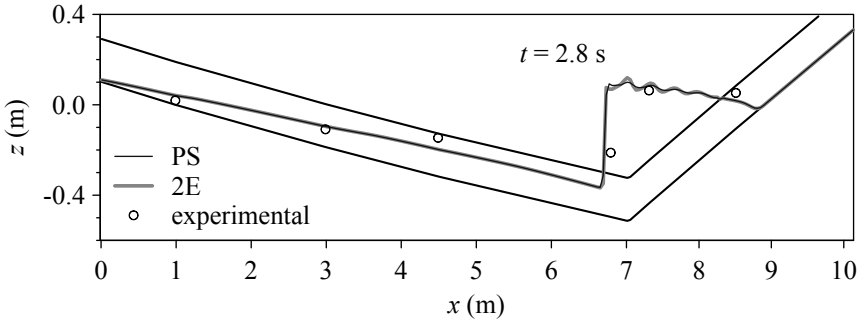

FIGURE 1.9 – Post-shock oscillations affecting the pressure head profile at $t = 2.8$ s

1.5.4 Sensitivity analysis on Manning's coefficient

Small changes in Manning's coefficient do not appear to be effective in improving the agreement of the numerical results with the experimental data in the last stage of the phenomenon. In fact Fig. 1.10, which shows the sensitivity of the PS model results to Manning's coefficient, confirms that, if n_m ranges from

$0.007\,\mathrm{m}^{-1/3}\mathrm{s}$ to $0.011\,\mathrm{m}^{-1/3}\mathrm{s}$ (a plausible range for Plexiglas), the long-time anticipation and overestimation of pressure head peaks are still observed (see Fig. 1.10b concerning gauge G5 for $t > 15\,\mathrm{s}$): as the roughness coefficient decreases, the temporal shift diminishes slightly, but, at the same time, the overestimation of the pressure head peak seems to increase. The same trend for the pressure head peak value can be observed at the initial stages of the pressurization process (Fig. 1.10b at $t = 3\,\mathrm{s}$) as roughness changes. Furthermore, the value of Manning's coefficient considerably affects the prediction of the long-time oscillatory process. As an example, Fig. 1.10a shows the results concerning gauge G1, which is characterized by repeated wetting and drying. It can be observed that the selected roughness coefficient ($0.009\,\mathrm{m}^{-1/3}\mathrm{s}$) allows the best reproduction of the experimental data, while the lowest value leads to an erroneous prediction of wetting at $t = 25\,\mathrm{s}$.

1.5.5 Convergence analysis

A convergence analysis on the grid size is performed on the basis of the proposed test case. Simulations are repeated with grid sizes $\Delta x = 0.08$, 0.04, 0.02, and 0.01 m, and the discrepancy from the reference solution obtained from a simulation performed using a very fine mesh with size $\Delta x = 0.005\,\mathrm{m}$ is estimated for the pressure head profile at $t = 2.8\,\mathrm{s}$ (Fig. 1.9). With this aim, the error based on the L_1-norm (LeVeque, 2002) is used:

$$E_{L_1} = \Delta x \sum_{i=1}^{N} |h_i - h_{i,ref}| \tag{1.23}$$

where N is the total number of cells along the profile.

Figure 1.11 summarizes the results. The error decreases with grid refinement approximately linearly with Δx, and this confirms that the numerical scheme is first-order accurate, as theoretically expected. The grid spacing $\Delta x = 0.04\,\mathrm{m}$ is

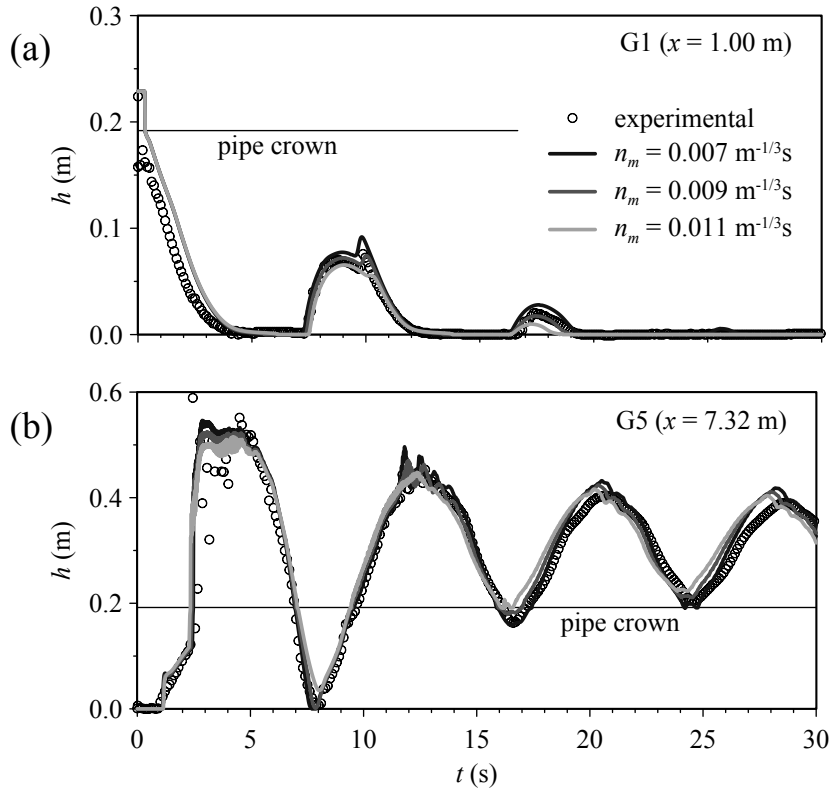

FIGURE 1.10 – Sensitivity analysis on Manning's roughness coefficient

chosen for all simulations as a satisfactory compromise between accuracy and computational efficiency. In fact, the use of this grid size already provides an overall good reproduction of the pipe geometry and gives sufficiently accurate results compared with the experimental ones, especially in the spatial description of shock waves and in the prediction of wetting and drying processes.

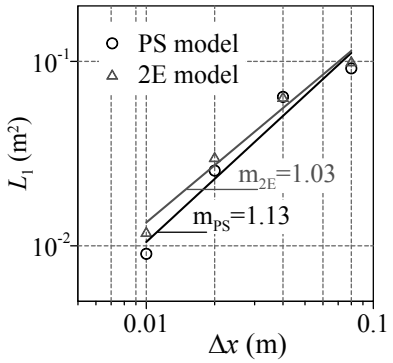

FIGURE 1.11 – Convergence analysis: L_1-error for the pressure head profile at $t = 2.8$ s as a function of grid size

1.5.6 Sensitivity analysis on slot width and pressure wave celerity

The sensitivity of the numerical results to pressure wave celerity (for the 2E model) and to slot width (for the PS model) is also analyzed. In the PS model, slot widths equal to 1%, 0.06%, 0.015%, and 0.0037% of the pipe diameter are investigated; correspondingly, pressure wave speed values equal to 12, 50, 100, and 200 m/s are assumed in 2E modelling.

Figure 1.12 shows some significant numerical results of the sensitivity analysis. It must be noticed that the almost instantaneous depressurization that occurs at upstream gauge G1 is better reproduced with high pressure wave celerity values (Fig. 1.12a). In general, however, the use of high celerity values does not lead to significant improvements in the numerical results compared with the ones obtained with smaller unphysical values. As an example, pressure head time series at gauge G5 are reported in Fig. 1.12b. The 2E model, even if affected by spurious oscillations originating at flow regime transitions, yields satisfactory results for all the pressure wave celerity values considered. Conversely, the PS model solution appears corrupted for the highest celerity values (Fig. 1.12c).

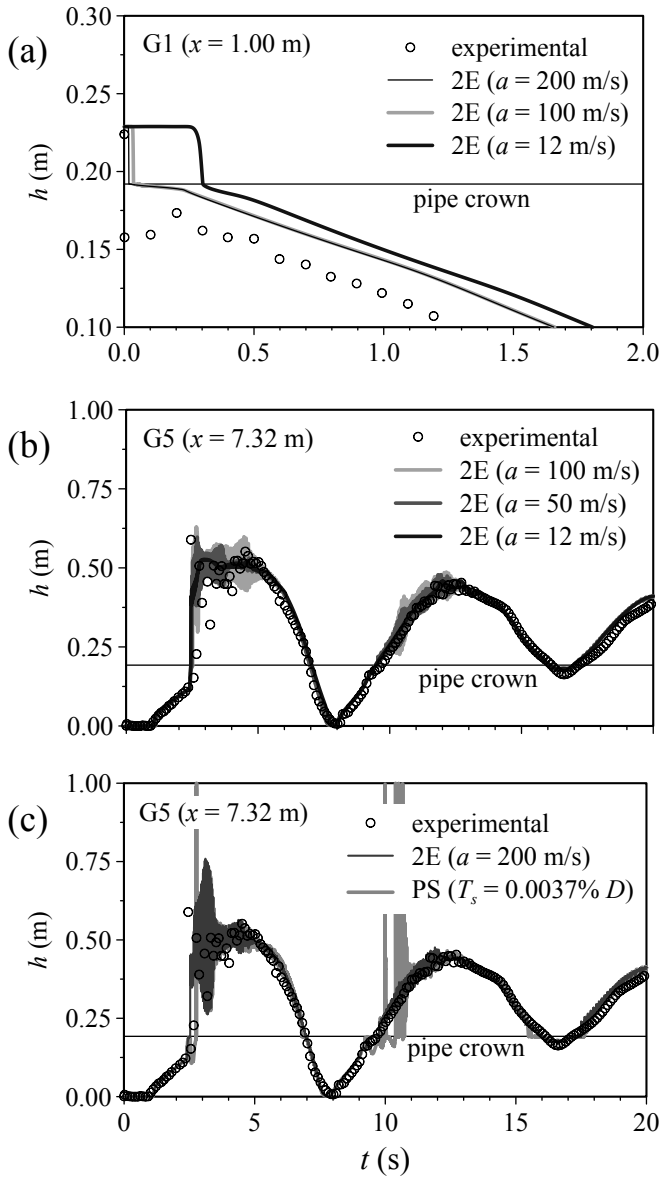

FIGURE 1.12 – Sensitivity analysis on the pressure wave celerity

1.6 Concluding remarks

This chapter compares the effectiveness of the PS model and of the 2E model on the basis of the simulation of a laboratory test case. The two 1D numerical methods appear to be equivalent in predicting the evolution of the phenomenon investigated when low values of the pressure wave speed are assumed. The 2E model, at the cost of greater complexity, seems more robust in handling the severe conditions of transient mixed flows when realistic pressure wave speeds are assumed. However, numerical instabilities and spurious oscillations always arise at the transition bores, due to the abrupt change in wave celerity.

For the test case considered here, the propagation of disturbances in the pressurized zone is quasi-instantaneous compared with the global evolution of the phenomenon. This fact confirms that realistic values of pressure wave speed are not strictly necessary to correctly predict the propagation of the transition waves. Therefore, the slot width for the PS model and the pressure wave celerity for the 2E model should be calibrated as model parameters rather than set on the basis of physical considerations.

Given the substantial similarity of results between the two models when low values of pressure wave celerity are chosen, the PS model is preferred in the following developments of this work due to its greater simplicity.

Manning's coefficient must be carefully calibrated in order to accurately predict the advancing of the wetting front observed during the first stages of the transient. The sensitivity analysis, performed on the basis of roughness values typically assumed for Plexiglas, shows that this parameter has a weak influence on the pressure head peak at flow regime transitions and on the propagation speed of the bore, but more noticeably affects the long-time oscillatory process.

Chapter 2

Local time stepping

2.1 Introduction

Free-surface flow and pressurized flow are characterized by celerity values which lie within a range of up to two orders of magnitude. In the case of mixed flows, one of the main consequences of the coexistence of wave celerity values varying considerably in the flow field is the fact that, if an explicit scheme is adopted, the pressurized cells (characterized by higher values of wave celerity) will determine the computational time step to be used to update the solution in the whole domain, according to the CFL stability condition. This restriction has two main negative effects: first, the computational effort increases greatly compared to free-surface flow simulations; second, the numerical solution in the free-surface portion of the domain is updated with a much smaller time step than its maximum allowable, resulting in an expected reduction of solution accuracy (Zhang et al., 1994). The problem is similar to the one encountered in free-surface flow applications when the mesh is locally refined, in which case the smallest grid cell will dictate the size of the time step, thereby drastically reducing model

efficiency, especially if the mesh refinement is restricted to only a small portion of the entire computational domain.

The local time stepping (LTS) strategy (or temporal adaptivity) has been proposed in the literature since the 1980s (Osher and Sanders, 1983) to increase computational efficiency when a non-uniform spatial discretization is used. It is based on the idea of updating each computational cell with a local time step as close as possible to its maximum allowable to satisfy the stability criterion, in contrast with the global time stepping (GTS) strategy, which advances the solution by using the minimum permissible time step in the whole domain. Most of the available LTS schemes are based on local time steps defined as integer multiples of a common reference time step (e.g. Kleb et al., 1992). However, some authors presented LTS algorithms where each cell can be advanced at its own time step without introducing any defined time step ratio (e.g. Dumbser, 2014). LTS methods have been satisfactorily applied to Euler and Navier-Stokes equations (e.g. Pervaiz and Baron, 1988; Kleb et al., 1992; Coquel et al., 2010), but also to other hyperbolic systems (e.g. Dumbser et al., 2007; Grote and Mitkova, 2010). Moreover, LTS schemes have also been adopted in combination with adaptive mesh refinement (AMR) techniques (e.g. Berger and LeVeque, 1998; Dumbser et al., 2013).

Applications of the LTS strategy to 1D and 2D shallow water equations can also be found in the literature (e.g. Crossley et al., 2003; Sanders, 2008; Trahan and Dawson, 2012; Kesserwani and Liang, 2015; Maleki and Khan, 2016). The results reported in these works show that considerable saving in computational time can be achieved without impairing model accuracy when a non-uniform mesh in used. However, despite the fact that LTS methods can be expected to be profitable not only when a local mesh refinement is employed, but also in applications involving significantly variable wave celerity, to the best of the author's knowledge the applicability of the LTS methodology to unsteady mixed

flows has not yet been thoroughly assessed. This strategy can be very useful and effective in practical applications, especially in those cases where only a small region of the domain is pressurized in an otherwise fully free-surface flow field. This occurs, for example, when a single branch of a pipe network is surcharged, or when a culvert, a bridge or an inverted siphon inserted in an open channel system are partially or totally surcharged. Actually, in the context of pipe network modelling, Sanders and Bradford (2011) adopted a TPA model in which the computational cells within each pipe were updated by using the minimum time step permissible in that pipe, while a larger global time step was used for the synchronization of all pipes and junctions.

This chapter presents the application of a LTS method modified from previous works (Kleb et al., 1992; Crossley and Wright, 2005) to the numerical modelling of 1D unsteady mixed flows. The LTS scheme is implemented in the PS model presented in Section 1.3. Several simulations of idealized numerical tests, of an experimental test, and of a simplified field-scale test are performed to assess the effectiveness and robustness of the LTS method in mixed flow applications and to evaluate the achievable improvement in model efficiency and solution accuracy in comparison with the conventional GTS scheme.

This chapter is derived in part from Dazzi et al. (2016).

2.2 Local time stepping numerical scheme

The LTS technique proposed by Kleb et al. (1992), and then successfully applied to shallow water equations by different authors (e.g. Crossley et al., 2003; Krámer and Józsa, 2007; Sanders, 2008), is adopted here with modifications. According to this method, the local time step Δt_i in each cell is set as a power of

two multiple of the minimum time step Δt throughout the computational domain:

$$\Delta t_i = 2^{m_i} \Delta t \tag{2.1}$$

where m_i is an integer parameter computed for each cell as:

$$m_i = \text{int} \left[\frac{\log\left(\dfrac{\Delta t_{i,CFL}}{\Delta t} \right)}{\log(2)} \right] \tag{2.2}$$

in which $\Delta t_{i,CFL}$ denotes the maximum allowable time step in cell i to satisfy the CFL condition.

Following Sanders (2008), the cell edges are also marked with a specific parameter m_f which is defined as $m_{f,i+1/2} = \min(m_i, m_{i+1})$, and a new integer parameter $m^\star$ is associated to each cell based on the following criterion: $m_i^\star = \min(m_{f,i-1/2}, m_{f,i+1/2})$; the local time step is then redefined according to Eq. (2.1) on the basis of the parameter $m_i^\star$. Finally, the value $m_{\max} = \max_i(m_i^\star)$ is computed, and the maximum time step is defined as $\Delta t_{\max} = 2^{m_{\max}} \Delta t$.

The time advancing of the computational cells during each update from the common time level t^n to the new common time level $t^{n+1} = t^n + \Delta t_{\max}$, is asynchronous: actually, the updating cycle from t^n to t^{n+1} is divided into a sequence of $2^{m_{\max}}$ intermediate steps (identified with the step number $p = 0, 1, \ldots, 2^{m_{\max}} - 1$); during each of these steps, only the cells for which $(p+1)$ is a multiple of $2^{m^\star}$ are advanced via Eq. (1.9) on the basis of their local time step Δt_i. Consequently, in the overall updating cycle, each computational cell is advanced by $2^{m_{\max} - m^\star}$ steps. In particular, cells marked with $m^\star = m_{\max}$ are advanced by a single time step of size $\Delta t_{\max}$, while those labelled with $m^\star = 0$ are updated by $2^{m_{\max}}$ unit steps of size Δt. The update algorithm is sketched in Fig. 2.1 for $m_{\max} = 2$, corresponding to a sequence of four intermediate steps.

Black dots indicate the known states at the beginning of each intermediate step, while white and black arrows represent cell updates and intercell flux evaluations performed during the current step, respectively.

The LTS algorithm for the flux evaluation at the cell boundaries follows the procedure proposed by Sanders (2008). Accordingly, at each intermediate step, numerical fluxes are evaluated only at those intercells labelled with a m_f value for which p is an integer multiple of 2^{m_f}. In particular, at the first intermediate step ($p = 0$) fluxes are computed at all cell boundaries and stored in a dedicated array; fluxes at intercells marked with $m_f = 0$ are re-evaluated at all intermediate steps (see Fig. 2.1).

Special attention must be devoted to the case of neighbouring cells characterized by different local time steps as, for example, cells $i-1$ and i in Fig. 2.1. Although the permissible time step of the cell i is $2\Delta t$, the update procedure based on the parameter $m^\star$ dictates that this cell is advanced by two distinct intermediate steps of size Δt. Only the flux at intercell $i - 1/2$ is re-computed during the second step ($p = 1$), while the flux at $i + 1/2$ is kept unchanged during the two steps $p = 0$ and $p = 1$. The added intermediate state is represented with dashed lines in Fig. 2.1. The use of $m^\star$ instead of m to identify which cells must be advanced during each intermediate step ensures that flux evaluation is carried out correctly at edges between adjacent cells characterized by different values of the parameter m. It can be noticed that the original method (Kleb et al., 1992; Crossley and Wright, 2005) employed a different strategy based on an interpolation procedure at interfaces, and a correction was necessary to ensure conservation properties (Tan et al., 2004; Krámer and Józsa, 2007). The update procedure adopted here instead is intrinsically conservative (Sanders, 2008).

Some authors suggest that, in order to increase the robustness and accuracy of the method, the jump in the m value between neighbouring cells should not exceed one (e.g. Krámer and Józsa, 2007). Moreover, the correct propagation

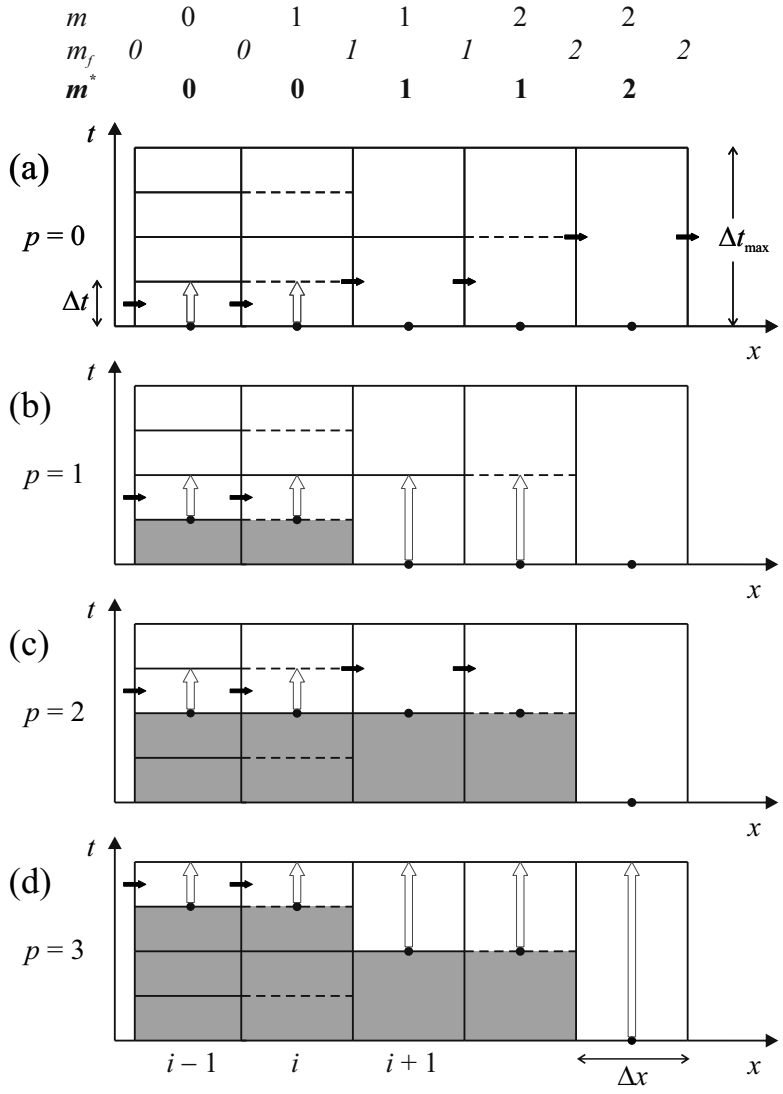

FIGURE 2.1 – Sketch of the LTS update procedure for $m_{\max} = 2$ (corresponding to a sequence of four intermediate steps)

of information at interfaces between cells updated with different time steps requires that a suitable interface region, where m varies gradually, separates areas characterized by highly different values of m (Crossley and Wright, 2005). In applications with non-uniform grids, this requirement is often satisfied thanks to an appropriate mesh design, which should guarantee smooth transitions from small to large cells. In the context of mixed flows, instead, transitions from free-surface to pressurized flow induce abrupt changes in the permissible time step size; thus values of m must be artificially re-assigned in a few cells near the flow regime transition prior to updating, in order to ensure the correct propagation of travelling waves. The procedure outlined in Crossley and Wright (2005) to define this interface region is adopted in this work. In short, if neighbouring regions are characterized by two different values m_1 and m_2 (with $\Delta m = m_2 - m_1 > 0$), the interface is composed of $2^{\Delta m} + 3$ cells. In particular, value m_1 is assigned to the first four cells originally belonging to the m_2 region; then, a gradual transition is created by assigning the value $m_1 + l$ to 2^l cells, with l being an integer counter ranging from 0 to $\Delta m - 1$. For example, at the interface between $m_1 = 0$ and $m_2 = 3$ (which could reasonably be the case of a flow regime transition), the original m vector $[\ldots, 0, 0, 0, \mathbf{3, 3, 3, 3, 3, 3, 3, 3, 3, 3}, 3, 3, \ldots]$ becomes $[\ldots, 0, 0, 0, \mathbf{0, 0, 0, 0, 0, 1, 1, 2, 2, 2, 2}, 3, 3, \ldots]$, where numbers in bold type refer to cells belonging to the interface zone.

A possible source of numerical instability is due to the fact that, throughout a global update from t^n to t^{n+1}, the local time step in each cell is kept constant, while, after a partial update, wave speed may increase in some cells, with consequent reduction of the permissible time step, and the CFL condition might then be no longer fulfilled in these cells. Possible strategies to face this problem include the use of a slightly reduced value of the Courant number (e.g. $Cr = 0.8$ in Sanders, 2008) and the artificial limitation of the maximum value of m (e.g. $m_{\max} = 3$ in Crossley and Wright, 2005; Krámer and Józsa, 2007). A different strategy is

implemented in this work. After each intermediate update from t^k to t^{k+1}, the local values assumed by the Courant number in the next intermediate time step are calculated as:

$$Cr_i^{k+1} = \Delta t_i \frac{|u_i^{k+1}| + c_i^{k+1}}{\Delta x_i}. \tag{2.3}$$

If the Courant number exceeds unity somewhere, the usual update procedure is interrupted, and all cells are advanced to the current intermediate time level t^{k+1} (see Fig. 2.2). After this synchronization, local time steps are re-evaluated in all cells and a new updating cycle can start. During the simulation of the laboratory test presented in Section 2.3.4 and used for validation, the robustness of the model appeared to be improved by stopping the update procedure and re-evaluating the local time steps, unlike what happened when limiting the maximum time step. This strategy actually proves to be effective when some cells become pressurized, starting from a free-surface condition; in this case celerity values increase suddenly, and instabilities possibly arise (and are further compounded by the well-known spurious oscillations near sudden flow regime transitions) if local time steps are not re-evaluated correctly.

2.3 Numerical tests

This section shows the results of some numerical simulations concerning different test cases and compares the LTS and GTS schemes in terms of accuracy and CPU time. First, the simple case of water at rest in a pipe is simulated; then, idealized test cases with analytical solution and a simple test case of gradual pipe filling are considered in order to assess the effectiveness and efficiency of the two time stepping techniques; finally, a laboratory test and a real-field test are analyzed as applications of practical significance. All simulations are performed on a workstation with a 2.67 GHz Intel Core i7 processor and 8 GB RAM.

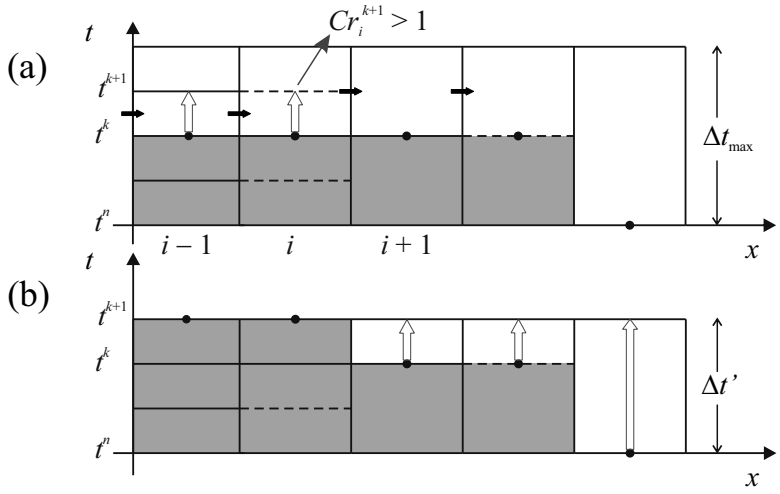

FIGURE 2.2 – Sketch of the synchronization procedure introduced to avoid instabilities: (a) if $Cr_i^{k+1} > 1$, the update procedure is interrupted, and (b) all cells are synchronized at t^{k+1}

2.3.1 Test cases with water at rest

The first test case concerns a 100 m long sloped pipe with diameter $D = 1$ m. Both pipe ends are closed, and the pipe is partially filled with still water up to a certain level. Different pipe slopes ranging from +0.5% to +5% (positive downwards) are considered. The water depth at the upstream end ($x = 0$ m) is assumed equal to 0.5 m for all slopes. Consequently, the upstream region of the pipe is in free-surface conditions, while the downstream part is pressurized; the length of this latter region increases with pipe slope, and the pressure head at the downstream end of the pipe ranges between 1 m and 5.5 m.

The computational domain is discretized with $N = 200$ cells of uniform size $\Delta x = 0.5$ m, and the Courant number is set at 0.9. Dimensionless slot widths T_s/D equal to 0.01 and 0.001 are assumed, corresponding to 27 m/s and 87 m/s pressure wave celerity values, and to ratios of maximum to minimum local time

step equal to 8 (i.e. $m_{\max} = 3$) and 32 (i.e. $m_{\max} = 5$), respectively. In both cases the solution is advanced for 3000 time steps in the GTS simulation and for the corresponding duration in the LTS simulation (approximately 50 s for $T_s/D = 0.01$, and 16 s for $T_s/D = 0.001$).

Both LTS and GTS schemes are able to preserve the static condition, except for round-off and truncation errors. As an example, at the end of the simulation with the pipe slope equal to +1%, the maximum discharge is in the order of 10^{-14} m^3/s in both cases.

Table 2.1 reports the speed-up factors calculated for simulations carried out with different pipe slopes and with both values of the slot width. The speed-up factor is the ratio of the execution time of the GTS simulation to that of the LTS simulation, thus representing an estimate of the performance improvement in terms of computational effort that the LTS scheme can achieve compared to the GTS scheme. The speed-up factor decreases with the increase in the percentage of pressurized cells and, theoretically, tends to unity when the whole computational domain is pressurized. Moreover, the narrower the slot is, the greater the value of the speed-up factor is.

TABLE 2.1 – Sensitivity of the speed-up factor to the percentage of pressurized cells and to the slot width for the test case of water at rest in a sloped circular pipe

Slope	α	$T_s/D = 0.01$		$T_s/D = 0.001$	
		Speed-up (actual)	Speed-up [Eq. (2.4b)]	Speed-up (actual)	Speed-up [Eq. (2.4b)]
+0.5%	1%	4.2	7.5	6.4	24.4
+0.553%	10%	3.2	4.7	4.3	7.8
+0.66%	25%	2.7	2.9	3.7	3.7
+1.0%	50%	1.9	1.8	2.4	1.9
+2.0%	75%	1.5	1.3	1.7	1.3
+5.0%	90%	1.3	1.1	1.5	1.1

These trends can be explained by estimating the achievable speed-up, as suggested by Kleb et al. (1992). If α ($0 < \alpha \leq 1$) is the percentage of pressurized cells (which is known *a priori* and does not change in time in this simple application), then a dimensionless quantification of the computational loads (W) associated with the GTS and LTS schemes (assumed proportional to the total number of updates carried out until the computational time t) and the achievable speed-up are roughly given by:

$$W_{GTS} \propto \sum_{i=1}^{N} \frac{t}{\Delta t} = N \frac{t}{\Delta t}, \quad W_{LTS} \propto \sum_{i=1}^{N} \frac{t}{\Delta t_i} = \alpha N \frac{t}{\Delta t} + (1-\alpha) N \frac{t}{2^{m_{\max}} \Delta t} \tag{2.4a}$$

$$\text{speed-up} = \frac{W_{GTS}}{W_{LTS}} \propto \left[\alpha + \frac{(1-\alpha)}{2^{m_{\max}}} \right]^{-1}. \tag{2.4b}$$

It follows that the LTS procedure basically reduces the number of update operations in the free-surface portion of the domain with a factor $2^{m_{\max}}$. Thus, other conditions being equal, the more cells belong to the free-surface region, the more update operations are skipped, and the faster the LTS simulation run time is, compared to the GTS simulation. Furthermore, narrower slots, corresponding to higher pressure wave celerity values, lead to higher values of the parameter $m_{\max}$, further increasing the achievable speed-up. The speed-up factors expected according to Eq. (2.4b) are also reported in Table 2.1 for comparison. The theoretical and actual values do not coincide, since the estimate of Eq. (2.4b) does not take into account the presence of an interface region with gradually varying values of m and other implementation details. Moreover, geometrical relations in free-surface conditions may require iterations or interpolations even for common cross-section shapes (e.g. circular), while in pressurized conditions explicit calculations can be done, and the CPU time necessary to perform such operations may differ for the two regimes. In any case, Eq. (2.4b) can be used as a rule of thumb to predict whether the use of the LTS strategy can be beneficial for a certain application,

even if in general the percentage of pressurized cells changes in time and may be difficult to estimate *a priori*.

Equation (2.4b) also suggests that the achievable speed-up should not depend on the total number of cells. This was verified by simulating the test case characterized by $T_s/D = 0.01$ and a pipe slope equal to +1% (which led to the pressurization of exactly half of the domain) with different grid sizes ($N = 200, 400,$ and 800 cells). The speed-up factor is almost constant, ranging between 1.9 and 2.1.

2.3.2 Test cases with analytical solution

Idealized test cases with analytical solution are presented in this subsection. The exact Riemann solver proposed by Kerger et al. (2011b) is used here to calculate reference solutions for initial value problems with piecewise constant initial states $\mathbf{U}_L$ (on the left-hand side) and $\mathbf{U}_R$ (on the right-hand side). All tests are performed in a frictionless 500 m long horizontal conduit with rectangular cross-section characterized by width $B = 1$ m and height $H = 1$ m. The slot width T_s is set at $0.01B$, which corresponds to pressure wave celerity approximately equal to 31 m/s. The computational domain is defined by the interval $[0, 500]$ m and the initial discontinuity is located at $x = 250$ m. Test conditions are summarized in Table 2.2. The solution of both Tests T1 and T2 is characterized by a rarefaction wave propagating to the left with transition between pressurized and free-surface conditions; the wave on the right instead is a free-surface shock in Test T1 and a free-surface rarefaction in Test T2. For the numerical simulations of both tests, the computational domain is discretized by means of $N = 500$ cells and the Courant number is set at 0.9.

Figures 2.3 and 2.4 compare the GTS and LTS numerical pressure head and velocity profiles with the analytical solution at $t = 6$ s. Both schemes correctly

TABLE 2.2 – Test conditions for three discontinuous initial-value problems with exact solution

Test	h_L(m)	u_L(m/s)	h_R(m)	u_R(m/s)	Description
T1	3.0	0.0	0.5	0.0	Left transition rarefaction and right shock
T2	1.8	−0.9	0.8	1.0	Left transition rarefaction and right rarefaction
T3	0.8	2.0	0.8	−2.0	Two transition shocks

predict the speed of both left and right waves and the intermediate state. However, the LTS scheme provides slightly less diffusive results in the free-surface portion of the solution (see the inserts in Figs. 2.3 and 2.4 at $x \simeq 270$ m).

The error based on the L_2-norm (LeVeque, 2002) is used to quantify the accuracy of the numerical solution. Accordingly, the error at a fixed time can be assessed in term of conserved variables as:

$$E_{L_2}(A) = \left[\frac{1}{N}\sum_{i=1}^{N}\left(A_i - A_{i,ref}\right)^2\right]^{0.5}, \quad E_{L_2}(Q) = \left[\frac{1}{N}\sum_{i=1}^{N}\left(Q_i - Q_{i,ref}\right)^2\right]^{0.5} \tag{2.5}$$

where the subscript "ref" refers to the analytical solution. Table 2.3 reports the L_2-norms calculated for flow area and discharge profiles at $t = 6$ s with progressively halved mesh size ($N = 500, 1000$, and 2000 cells). The LTS scheme gives lower error norms than the GTS scheme for all mesh sizes and for both test cases. The improvement in accuracy mainly concerns the free-surface region of the flow field, where error norms decrease by about $20 - 30\%$ switching from GTS to LTS scheme, since in this region the Courant number is locally closer to unity. On the other hand, in the pressurized region of the flow field, error norms increase slightly (only by a few percent) for the LTS numerical solution. This is probably due to the fact that the LTS technique adopted here employs the same time step over a certain number of intermediate updates, potentially making the scheme

slightly more diffusive, especially where celerity decreases, as near the transition from pressurized to free-surface flow; conversely, the time step is recomputed after each time advancement in the GTS scheme.

Table 2.3 also reports the speed-up factor for test cases T1 and T2. In general, the speed-up factor is not expected to change considerably with the total number of cells, and this is confirmed by the fact that it varies from 1.6 to 1.9 (corresponding to CPU time reduction between 37% and 47%) if N increases from 500 to 2000. In this case, the percentage of pressurized cells is time-dependent; considering an average value in the time interval between $t = 0\,\mathrm{s}$ and $t = 6\,\mathrm{s}$, the speed-up estimated according to Eq. (2.4b) is approximately equal to 1.9 for both tests.

Finally, the numerical scheme does not deteriorate mass conservation; in fact, for Test T1, which involves no inflows or outflows in the time interval considered, the relative mass conservation error is in the order of 10^{-15} (with reference to the mass initially present in the conduit) for both LTS and GTS schemes at the end of the simulation (after approximately 10^3 updates in the GTS simulation with $N = 2000$ cells).

Test T3 is characterized by an initial condition representing two approaching free-surface uniform flows; the impact produces two pipe filling bores propagating

TABLE 2.3 – Comparison between GTS and LTS accuracy and efficiency at $t = 6\,\mathrm{s}$ for different mesh sizes for test cases T1 and T2

Test	N	$E_{L_2}(A)(\times 10^{-3}\,\mathrm{m}^2)$		$E_{L_2}(Q)(\times 10^{-2}\,\mathrm{m}^3/\mathrm{s})$		Speed-up
		GTS	LTS	GTS	LTS	
T1	500	12.0	10.5	4.0	3.6	1.6
	1000	8.5	6.4	3.0	2.5	1.6
	2000	6.1	4.4	2.2	1.8	1.9
T2	500	9.9	7.4	3.2	2.4	1.7
	1000	7.2	4.8	2.3	1.7	1.6
	2000	5.0	3.1	1.7	1.1	1.9

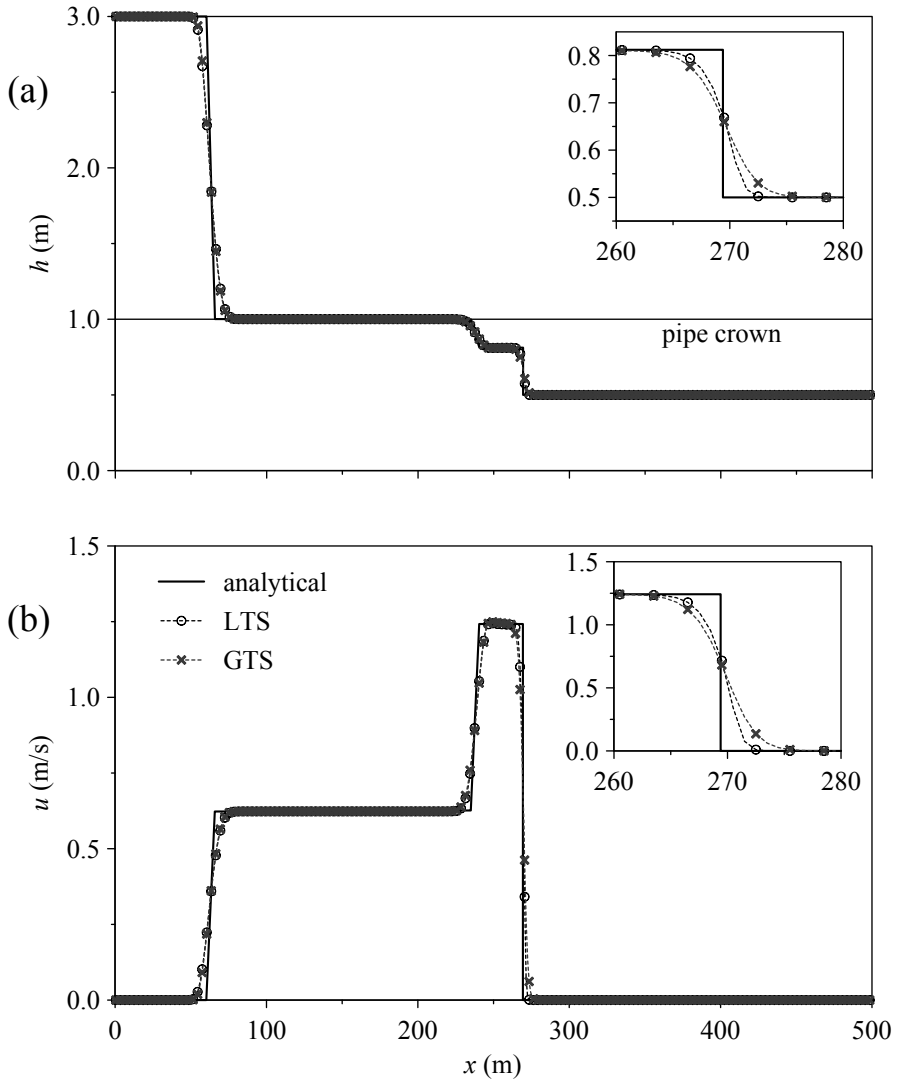

FIGURE 2.3 – GTS and LTS numerical profiles of pressure head (a) and velocity (b) at $t = 6$ s for tests T1, compared with analytical solutions. In numerical profiles, one symbol out of three is represented for clarity

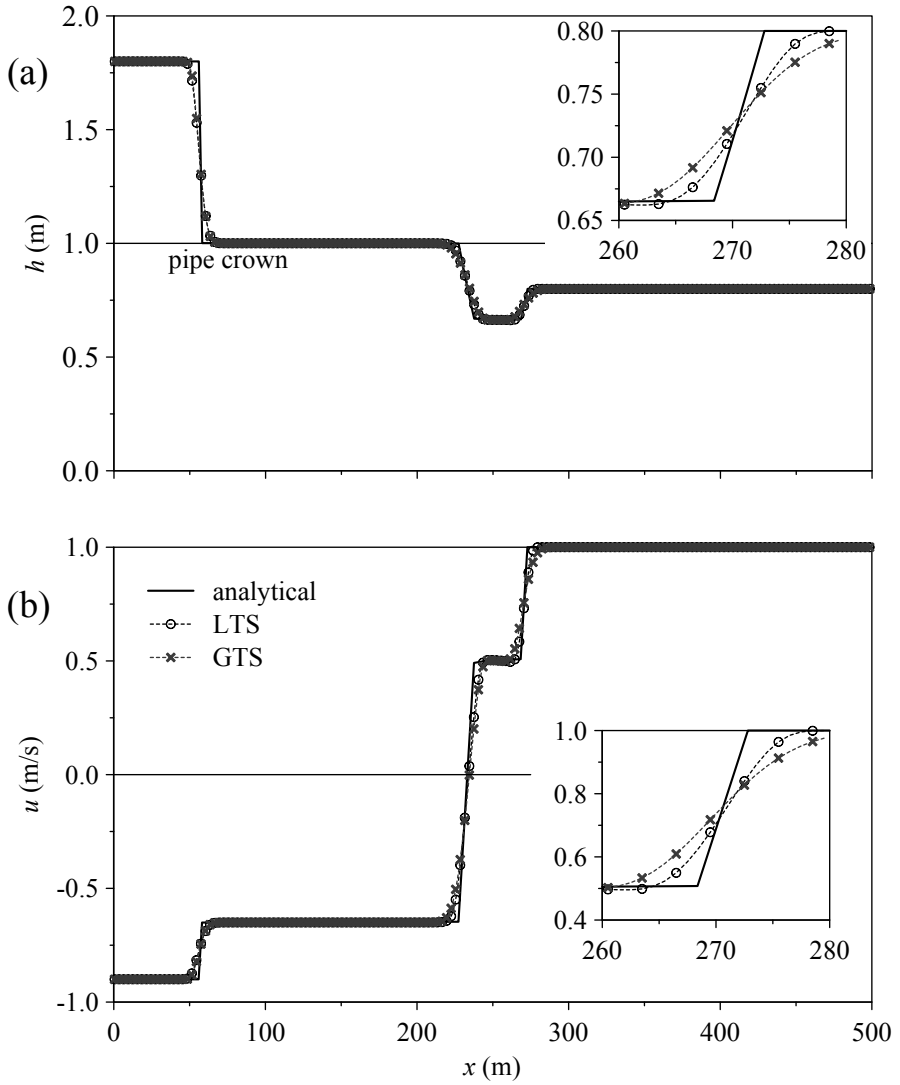

FIGURE 2.4 – GTS and LTS numerical profiles of pressure head (a) and velocity (b) at $t = 6$ s for tests T2, compared with analytical solutions. In numerical profiles, one symbol out of three is represented for clarity

in opposite directions. The computational domain is discretized by means of $N = 1000$ cells and simulations are repeated for three different values of the slot width ($T_s/B = 0.04, 0.01$, and 0.001), corresponding to pressure wave celerity values approximately equal to 15, 31, and 100 m/s. The Courant number is set at 0.7. Figure 2.5 shows the pressure head and velocity profiles at $t = 20$ s; only LTS results are reported, since the LTS and GTS profiles practically overlap. The speed-up factor increases with the reduction of the slot width, and ranges from 1.4 to 1.9 to 2.4.

2.3.3 Gradual pipe filling

Pipe pressurization can be induced not only by a transition bore (as in Test T3), but also by gradual rising of the water level (e.g. Capart et al., 1997; Ferreri et al., 2014b). The numerical simulation of gradual pressurization is presented in this subsection in order to further verify the effectiveness of the LTS scheme.

The test is performed in a 100 m long circular pipe with 1 m diameter and 0.4% slope. Manning's roughness coefficient is set at $0.015\,\mathrm{m}^{-1/3}\mathrm{s}$. A subcritical uniform free-surface flow with $0.7\,\mathrm{m}^3/\mathrm{s}$ discharge and approximately 0.52 m normal depth is assumed as initial condition. The sudden closure (at $t = 0$) of a gate located at the downstream end of the pipe causes an abrupt increase in the water depth which propagates upstream as a free-surface shock wave. Due to pipe slope, after a few seconds the downstream portion of the pipe becomes pressurized and a smooth flow regime transition travelling upward arises.

The pipe is discretized by $N = 100$ computational cells ($\Delta x = 1$ m), and the slot width is set at $0.01D$. The Courant number is assumed equal to 0.9, and the solution is advanced for 60 s. A constant discharge is specified at the upstream boundary, while the reflective boundary condition is imposed downstream.

Figure 2.6 shows the pressure head profiles at $t = 5$, 20, and 40 s for the

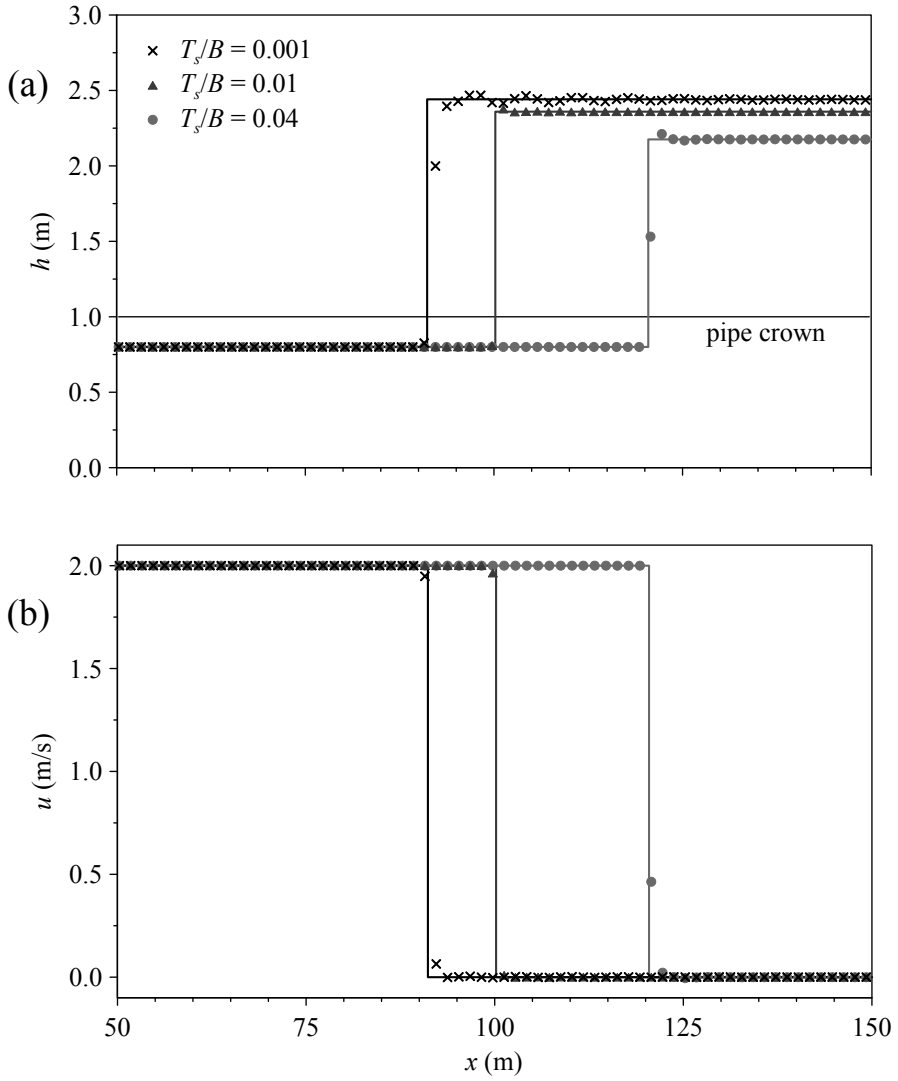

FIGURE 2.5 – Numerical (LTS) and analytical (solid lines) pressure head (a) and velocity (b) profiles at $t = 20\,\mathrm{s}$ for Test T3. The x-axis is restricted to $[50, 150]\,\mathrm{m}$ for clarity. In numerical profiles, one symbol out of three is represented

GTS and LTS schemes, along with a reference solution obtained with a very fine mesh ($N = 2000$ cells, $\Delta x = 0.05$ m). Moreover, Table 2.4 reports the L_2-error norms of flow area and discharge profiles calculated via Eq. (2.5) at selected times (the same shown in Fig. 2.6) with reference to the fine mesh predictions. The results confirm that the overall numerical scheme is able to describe smooth free-surface/pressurized interfaces and that the LTS scheme reproduces the moving free-surface discontinuities in a slightly more accurate way than the GTS model. The speed-up factor is approximately 1.6 in this test.

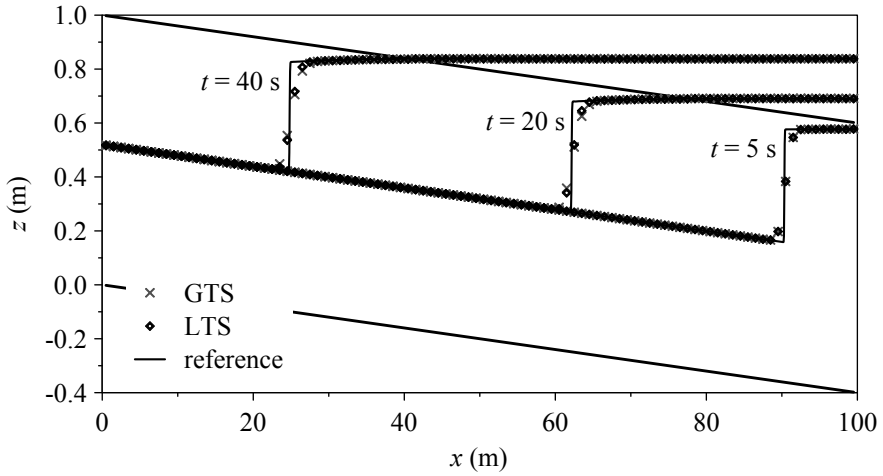

FIGURE 2.6 – Numerical (LTS and GTS, $N = 100$ cells) and reference ($N = 2000$ cells) pressure head profiles at $t = 5$, 20, and 40 s for the gradual flow transition

TABLE 2.4 – Gradual pipe filling: LTS and GTS L_2-error norms of flow area and discharge profiles at selected times

time (s)	$E_{L_2}(A)(\times 10^{-2}\ \mathrm{m}^2)$		$E_{L_2}(Q)(\times 10^{-2}\ \mathrm{m}^3/\mathrm{s})$	
	GTS	LTS	GTS	LTS
5	1.4	1.4	3.8	3.8
20	1.5	1.3	3.7	3.4
40	1.6	1.4	2.9	2.6

2.3.4 Laboratory test case

The robustness and effectiveness of the LTS scheme are assessed in this subsection on the basis of the laboratory test proposed by Aureli et al. (2015) and described in Section 1.5.1.

The computational domain is discretized by means of 300 grid cells ($\Delta x = 0.04$ m) and Manning's coefficient is set at 0.009 $\mathrm{m}^{-1/3}$s. The slot width is assumed to be equal to $0.01D$ and the Courant number is set at 0.9. A reflective boundary condition is imposed at the upstream end, whereas the downstream end is never reached by the flow.

Figures 2.7 and 2.8 show GTS and LTS numerical pressure head profiles at selected times, along with the local experimental measurements available. Moreover, Fig. 2.9 compares the numerical and experimental pressure head time series at Sections G1 ($x = 1.0$ m) and G5 ($x = 7.32$ m), as well as velocity time series at Section V5 ($x = 7.28$ m). The LTS scheme yields almost identical numerical results to the ones provided by the GTS scheme. Table 2.5 reports GTS and LTS L_2-errors of flow area and discharge profiles calculated via Eq. (2.5) at selected times (the same shown in Figs. 2.7 and 2.8) with reference to the GTS results obtained with a very fine mesh ($\Delta x = 0.005$ m). The results confirm that the accuracy of the two schemes is comparable. Moreover, for both schemes, the dimensionless mass conservation error remains in the order of 10^{-15} at the end of the simulation (corresponding to almost 10^4 updates in the GTS simulation). Thus, LTS does not deteriorate mass conservation, even in the presence of wetting and drying. Finally, the speed-up factor varies approximately from 2.0 to 2.1 (corresponding to about 50% CPU time reduction) as the mesh is refined from $\Delta x = 0.04$ m to $\Delta x = 0.005$ m.

The sensitivity of numerical results to the slot width is also analyzed. The simulation of this test case is repeated with dimensionless slot widths decreasing

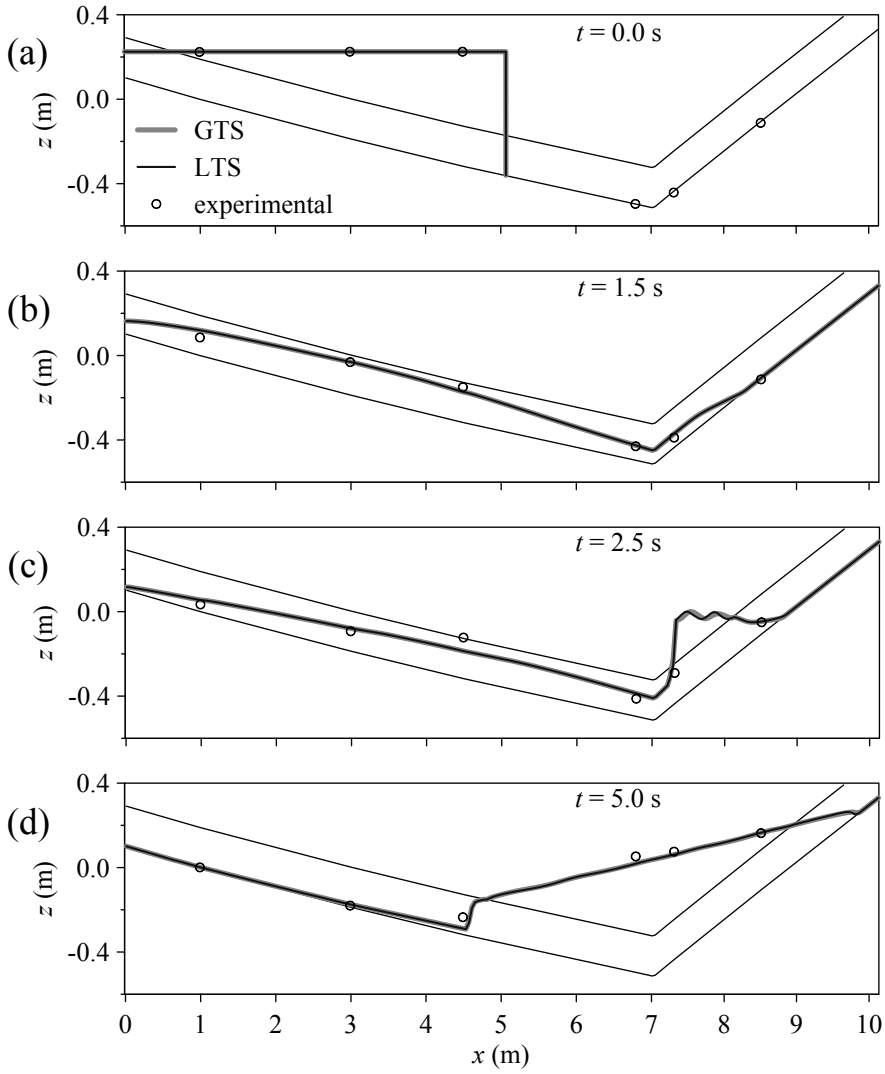

FIGURE 2.7 – Numerical (GTS and LTS) pressure head profiles at selected stages for the experimental test case. Experimental data are also reported. The spatial variable x represents the distance along the pipe. Elevation z is referred to the bottom of section G1

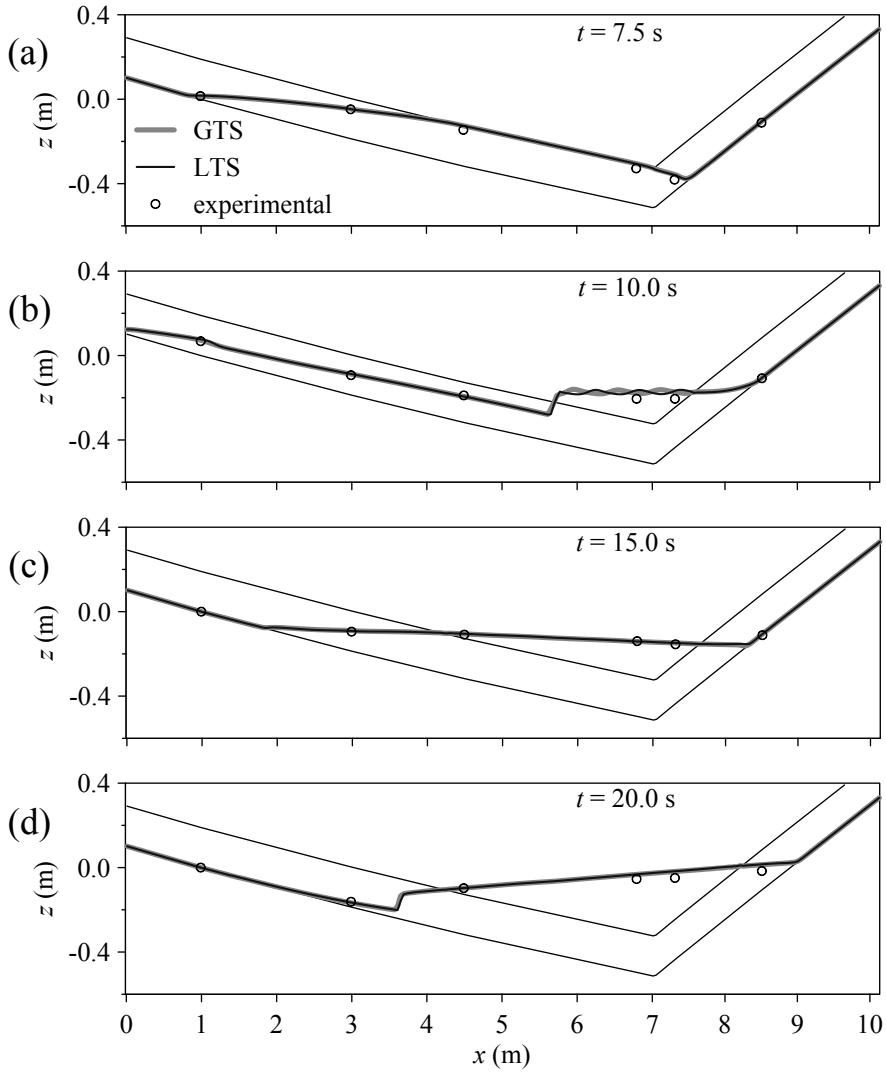

FIGURE 2.8 – Numerical (GTS and LTS) pressure head profiles at selected stages for the experimental test case. Experimental data are also reported. The spatial variable x represents the distance along the pipe. Elevation z is referred to the bottom of section G1

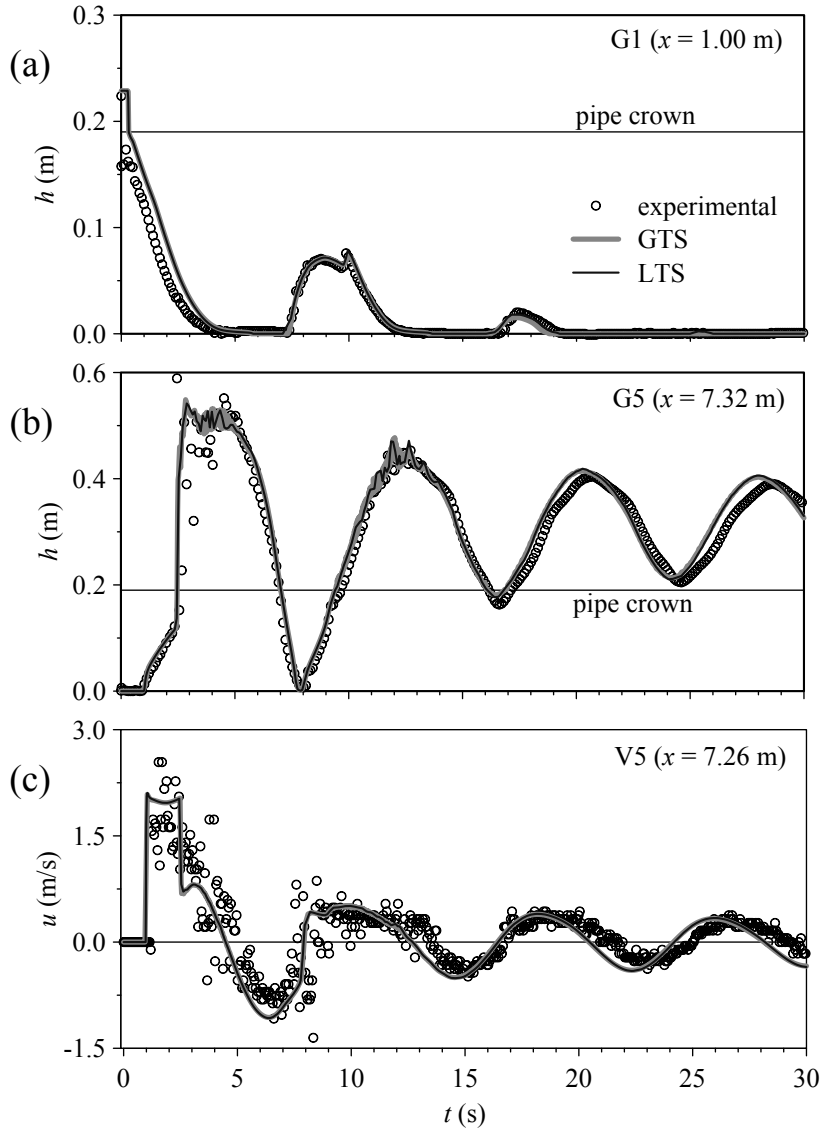

FIGURE 2.9 – Numerical (GTS and LTS) and experimental pressure head and velocity time series at selected cross-sections

TABLE 2.5 – Experimental test case: LTS and GTS L_2-error norms of flow area and discharge at selected times with reference to a simulation performed with a very fine mesh ($\Delta x = 0.005$ m)

time (s)	$E_{L_2}(A)(\times 10^{-4}\ \mathrm{m}^2)$		$E_{L_2}(Q)(\times 10^{-4}\ \mathrm{m}^3/\mathrm{s})$	
	GTS	LTS	GTS	LTS
1.5	2.8	2.8	2.5	2.6
2.5	5.7	5.3	7.2	7.3
5.0	4.9	4.3	3.3	2.8
7.5	3.8	4.6	3.0	2.8
10.0	3.7	2.8	3.4	4.3
15.0	4.1	3.0	2.1	1.0
20.0	3.1	4.0	2.5	2.4

from 0.01 to 0.0005 (correspondingly, the pressure wave celerity increases from 12 m/s to 54 m/s), maintaining $\Delta x = 0.04$ m and assuming $Cr = 0.5$. The speed-up factor is observed to increase from 2.2 to 2.5. As an example, numerical and experimental pressure head time series at cross-section G4 ($x = 6.8$ m) are reported in Fig. 2.10 for the simulation performed with $T_s/D = 0.0005$. It must be considered that GTS and LTS time series are characterized by different temporal resolutions, since output results are available only at synchronization times for the LTS simulation, whereas GTS results can be obtained after each update. In this simulation, m_{max} is expected to be equal to 6, hence in Fig. 2.10 only one value out of 2^6 is represented in the GTS time series, in order to compare the numerical results consistently.

2.3.5 A field-scale application

The simulation of an idealized field-scale test is finally presented. A 2000 m long sewer pipe, characterized by a circular cross-section ($D = 1.2$ m) and by 0.1% slope, intersects a subway structure at $x = 1000$ m, and an inverted siphon is used to bypass the obstacle from below. This element is simply schematized

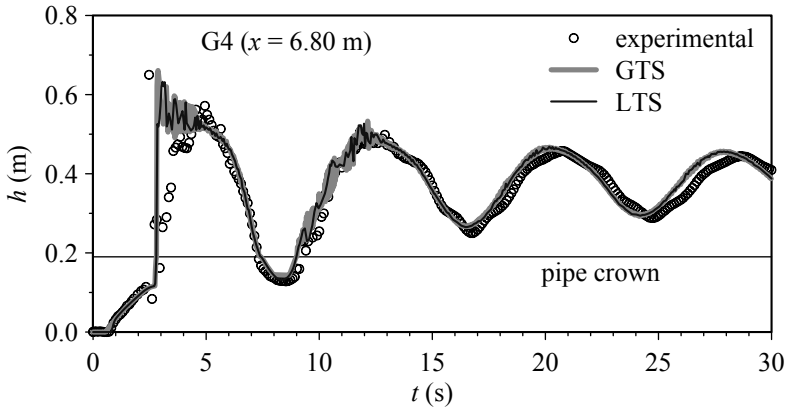

FIGURE 2.10 – Numerical (GTS and LTS) and experimental pressure head time series at cross-section G4 ($T_s/D = 0.0005$). Only one value out of 64 is considered in the GTS time series

as a vertical deviation in the pipe axis, which is 50% sloped (downward) for 8 m, horizontal for 5 m, and −50% sloped (upward) for 7 m. This geometry is certainly a simplification, since these structures often consist of multiple pipes, inlet and outlet chambers, and control devices. However, the main purpose of this test case is to demonstrate the efficiency of the LTS scheme in practical applications where only a small region of the flow field is surcharged.

The pipe is initially dry, the only exception being the siphon, filled with static water, as if it was left from a previous rainfall event. At $t = 0$ min, a triangular inflow hydrograph, with 30 min duration and 1.2 m^3/s peak discharge at $t = 9$ min, is imposed at the upstream section. A free outfall is assumed downstream. The domain is discretized by means of $N = 2000$ cells of length $\Delta x = 1$ m; moreover, the Courant number is assumed equal to 0.9, Manning's coefficient is set at 0.014 $m^{-1/3}s$, and the dimensionless slot width is set at 0.01 (corresponding to a 30 m/s pressure wave celerity value). The flood propagation in the sewer is simulated for 60 min.

As an example of model results, Fig. 2.11 shows pressure head profiles at

selected times (Fig. 2.11a), and hydrographs of discharge (Fig. 2.11b) and pressure head (Fig. 2.11c) at three cross-sections. Only LTS results are represented, since GTS results are almost identical. The maximum water depth predicted is 0.84 m, thus the flow in the pipe always remains in free-surface conditions, except for the few cells (less than 1% of the total) representing the siphon. Hence, this case is suitable to be simulated with the LTS scheme, since the few pressurized cells would dictate the time step for the whole domain if the GTS scheme was used. The achieved speed-up is in fact equal to 5.7, corresponding to 82% CPU time reduction. If the simulation is repeated with "wet" initial conditions (for example, 0.05 m in the whole pipe), the speed-up grows to 6.5 (−85% CPU time). This is due to the fact that, for both schemes, flux evaluation in dry cells is computationally inexpensive compared to the case of wet cells, thus making the improved performance of the LTS scheme more evident.

2.4 Concluding remarks

In this chapter the local time stepping strategy is applied for the first time to the numerical modelling of unsteady mixed flows. The LTS method adopted, coupled with a Godunov-type finite volume solver based on the Preissmann slot approach, is found to be effective in simulating these phenomena as regards both computational efficiency and solution accuracy. In particular, the results of the numerical simulations show the following:

- The LTS reduces run time and improves model efficiency in comparison with the conventional GTS, without impairing overall solution accuracy and without deteriorating mass conservation. In the transient test cases presented in this work, speed-up factors between 1.4 and 6.5 were achieved (corresponding to a reduction in CPU time between 29% and 85%). Moreover, the LTS strategy ensures improved accuracy in the free-surface region of

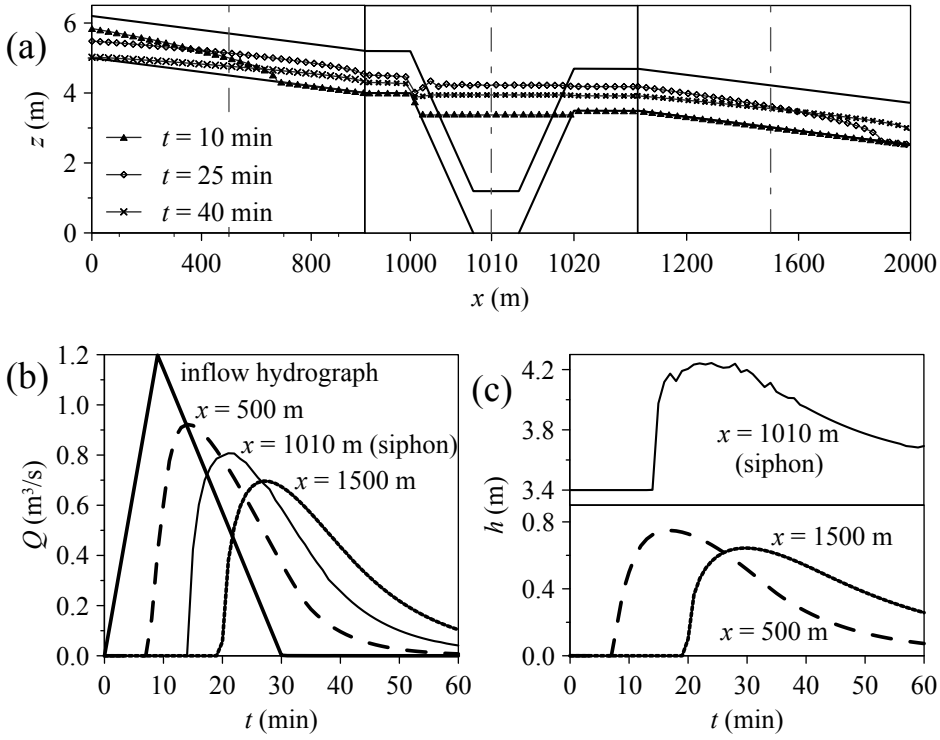

FIGURE 2.11 – LTS numerical results for the inverted siphon simulation: (a) pressure head profiles at selected times (elevation z is referred to the siphon invert; the representation is distorted near the siphon to improve readability); (b) discharge hydrograph at inflow and at three selected sections; (c) pressure head time series at three sections

the flow field.

- The speed-up factor increases with the percentage of free-surface cells in the domain (which is time-dependent in unsteady applications); this suggests that LTS is particularly suitable for applications where flow pressurization is expected to involve only a small region of the flow field.
- The run time improvement achievable by the LTS scheme (compared to the GTS scheme) is slightly enhanced when narrow slot widths, corresponding to more realistic values of pressure wave celerity, are employed.
- The novel procedure based on the check of the local Courant number, which interrupts the series of intermediate updates and imposes synchronization to a suitable limited computational time, is useful to prevent numerical instabilities.

The application of the LTS method presented in this paper can easily be extended to finite volume mixed flow models based on different approaches, such as the TPA model or the dual model, and to numerical schemes of higher order of accuracy.

Chapter 3

2D modelling of mixed flows

3.1 Introduction

Researchers have mainly focused their attention on the implementation and validation of 1D numerical models, because the 1D approximation is suitable for most applications (e.g. Politano et al., 2007; Sanders and Bradford, 2011; Trindade and Vasconcelos, 2013; Cataño-Lopera et al., 2014). However, some practical situations involving mixed flows require a 2D approximation, at least. This is the case of hydraulic structures, such as bridges and culverts, which may become partially or totally pressurized. In the numerical simulation of flood events in a wide area, the presence of bridges, culverts, or similar structures is often either neglected (when these elements do not sensibly affect the flow field) or treated in a simplified way: as an example, Ratia et al. (2014) account for the head loss induced by a bridge as an additional source term in a 2D finite volume numerical scheme. For these hydraulic singularities, which are inevitably poorly described in large 2D areas (unless a very high spatial resolution is adopted), 2D/1D dynamically linked modelling has been proposed for an adequate prediction

of the near-field effects (e.g. Syme et al., 2004). However, a near-field simulation of the flooding process may require a more accurate description of the flow field around and under bridges or culverts, coupled with a detailed representation of the topography.

Moreover, the 1D approximation appears to be unsuitable for circular or vaulted conduits (such as derivation or by-pass tunnels) in the presence of a curved pipe alignment, when the superelevation in water surface causes a partial wetting of the conduit ceiling.

Therefore, 2D numerical modelling of transient mixed flow appears to deserve attention, but to date, to the best of the author's knowledge, only the study by Van Nam et al. (2012) has attempted to examine this topic, providing original experimental data concerning a steady flow induced in a narrow rectangular culvert placed asymmetrically inside a laboratory flume with rectangular cross-section. Another recent work by Bashiri Atrabi et al. (2015) focused on the 2D extension of an interface-tracking model to simulate the propagation of air cavities into ducts. However, only the transition from pressurized to free-surface flow (and not viceversa) could be modelled.

This chapter presents a novel 2D model for simulating transient mixed flows which extends the validity of the 2D shallow water equations to the case of pressurized flows using the Preissmann slot approach. With this aim, each computational cell is expanded over its top by ideally adding two perpendicular narrow slots. The model is validated by comparison with exact solutions of 1D discontinuous initial value problems and radial solutions of idealized test cases with cylindrical symmetry. Moreover, the simulation of a simple laboratory test case concerning a partially pressurized arch bridge in steady state conditions is performed. Finally, the suitability of the model to deal with field-scale problems is assessed on the basis of the simulation of the transit of a dam-break bore under an arch bridge. This chapter is derived in part from Maranzoni et al. (2015).

3.2 Mathematical model

The extension of the Preissmann slot concept to 2D modelling is based on the idea of introducing two hypothetical narrow vertical slots on the top of each Cartesian element in which the 2D computational domain is assumed to be discretized. The two slots are aligned along the Cartesian plane directions x and y and extend indefinitely upward (see Fig. 3.1). In Fig. 3.1, H denotes the elevation of the ceiling above the bottom; $\Delta x = x_2 - x_1$ and $\Delta y = y_2 - y_1$ indicate the plane dimensions of a generic fixed control element with a rectangular base; T_x and T_y are the widths of the slots along the y- and x-axis directions, respectively. As long as the water surface is below the ceiling, free surface flow occurs and h represents the local water depth; conversely, when the water surface reaches the top of the cell, the free-surface is inside the slot and water depth h provides an estimate of the pressure head of an equivalent pressurized flow. Again in Fig. 3.1, A_x and A_y are the flow areas of the x- and y-normal faces respectively, shaped as rectangular sections with a vertical slot added on the ceiling.

3.2.1 Governing equations

The mass conservation principle, expressed in the Eulerian form and applied to the case of incompressible flow, states that the rate of change of the total amount of fluid volume V in a control volume equals the net volume rate of flow entering through its boundaries. For the fixed control volume shown in Fig. 3.1 with planar basis $[x_1, x_2] \times [y_1, y_2]$, this leads to the following basic integral form of the continuity relation:

$$\frac{\partial V}{\partial t} = [\mathsf{f}(x_1, t) - \mathsf{f}(x_2, t)] + [\mathsf{g}(y_1, t) - \mathsf{g}(y_2, t)] \tag{3.1}$$

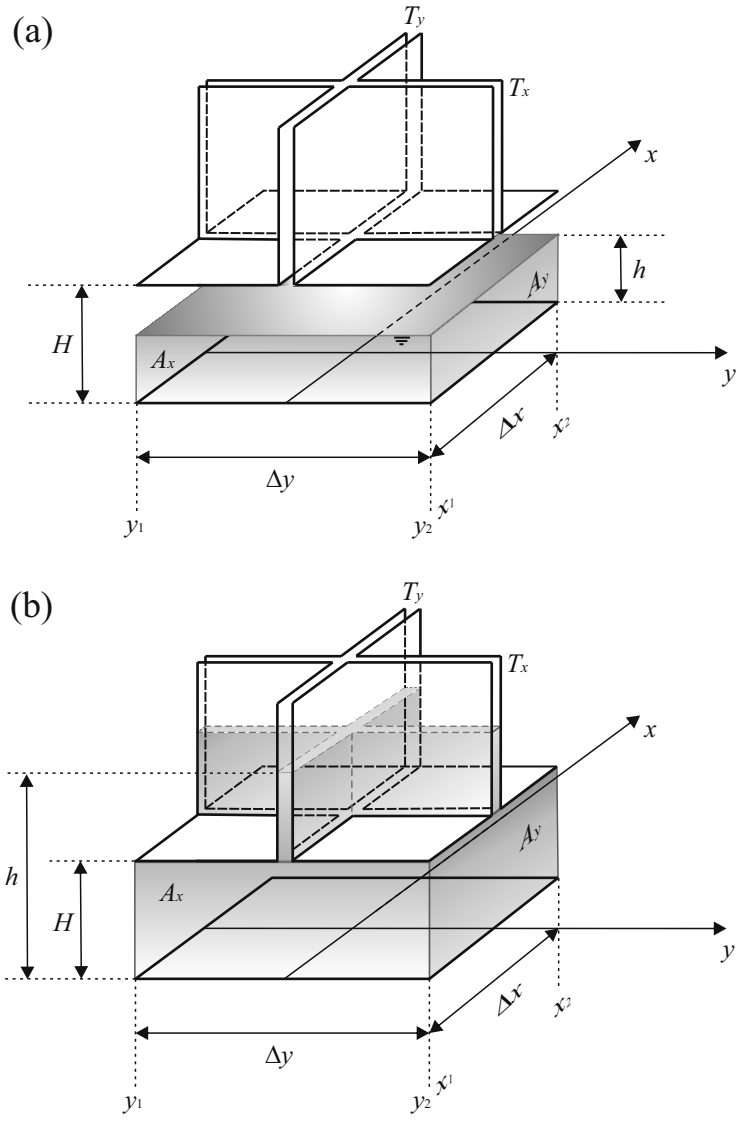

FIGURE 3.1 – Definition sketch of the 2D elemental Cartesian control volume with the addition of two narrow vertical slots on the top: flow not involving (a) or involving (b) the slots

where $\mathsf{f} = \int_{A_x} u \, \mathrm{d}A_x$ and $\mathsf{g} = \int_{A_y} v \, \mathrm{d}A_y$ represent the intercell volume fluxes in the x- and y-directions across the lateral faces A_x and A_y respectively, u and v are the x- and y-components of velocity. Introducing the surface-averaged values $\bar{u}$ and $\bar{v}$ of velocity components over the areas A_x and A_y, the flux functions f and g can be represented as follows:

$$\mathsf{f} = \bar{u} A_x, \quad \mathsf{g} = \bar{v} A_y. \tag{3.2}$$

Division of Eq. (3.1) by the plane area $\Omega = \Delta x \times \Delta y$ leads to:

$$\frac{\partial \bar{h}}{\partial t} = \frac{1}{\Delta x} \left[\bar{q}_x(x_1, t) - \bar{q}_x(x_2, t) \right] + \frac{1}{\Delta y} \left[\bar{q}_y(y_1, t) - \bar{q}_y(y_2, t) \right] \tag{3.3}$$

in which $\bar{h} = \frac{V}{\Omega}$ is the average value of the areal density of water volume over the control element, i.e. a kind of "average water depth" over the planar area Ω, while $\bar{q}_x = \frac{A_x \bar{u}}{\Delta y}$ and $\bar{q}_y = \frac{A_y \bar{v}}{\Delta x}$ are equivalent flow discharges per unit width along the x- and y-axis directions, respectively. If the control volume becomes infinitesimal, for smooth solutions Eq. (3.3) reduces to the differential form:

$$\frac{\partial \bar{h}}{\partial t} + \frac{\partial \bar{q}_x}{\partial x} + \frac{\partial \bar{q}_y}{\partial y} = 0. \tag{3.4}$$

In addition to mass, momentum is also a "conserved" quantity for the fixed control volume of Fig. 3.1, and the linear momentum equation can be derived from Newton's second law. In the following, only the x-component of the equation will be derived. First, the rate of change of the x-momentum within the control volume (CV) can be written as:

$$\frac{\partial}{\partial t} \int_{CV} \rho u \, \mathrm{d}V \simeq \frac{\partial}{\partial t} (\rho \bar{u} A_x \Delta x) \tag{3.5}$$

assuming that the water mass contained in the slot extending along the y-direction

does not carry x-momentum. Recalling the definition of the equivalent unit discharge $\bar{q}_x$ introduced above, the time derivative in Eq. (3.5) becomes

$$\frac{\partial}{\partial t}(\rho \bar{q}_x \Omega). \tag{3.6}$$

Then, the x-component of the convective part of the momentum flux through the faces normal to x-axis is:

$$m_c(x_1, t) - m_c(x_2, t) \tag{3.7}$$

with $m_c = \int_{A_x} \rho u^2 \mathrm{d}A_x \simeq \rho \bar{u}^2 A_x$, while the x-momentum carried past the faces normal to y-axis becomes:

$$n_c(y_1, t) - n_c(y_2, t) \tag{3.8}$$

where $n_c = \int_{A_y} \rho uv \mathrm{d}A_y \simeq \rho \bar{u}\bar{v} A_y$. Consequently, the total advective contribution to the momentum flux is:

$$-\rho \Delta y \left(\frac{\bar{q}_x^2}{\bar{h}_x} \right) \Bigg|_{x_1}^{x_2} - \rho \Delta x \left(\frac{\bar{q}_x \bar{q}_y}{\bar{h}_x} \right) \Bigg|_{y_1}^{y_2} \tag{3.9}$$

where $\bar{h}_x = \frac{A_x}{\Delta y}$ represents the surface-averaged water depths over A_x (similarly $\bar{h}_y = \frac{A_y}{\Delta x}$). By assuming a hydrostatic distribution, the pressure term in the x-momentum flux reads:

$$m_p(x_1, t) - m_p(x_2, t) = -(\rho g \zeta_x A_x) \Big|_{x_1}^{x_2} \tag{3.10}$$

where ζ_x denotes the vertical distance of the centroid of the areas A_x from the water surface.

Finally, the source term includes a component due to gravity:

$$\int_{CV} \rho g S_{0x} \mathrm{d}V \simeq \rho g A_x S_{0x} \Delta x \tag{3.11}$$

S_{0x} being the bottom slope in the x-axis direction, and a component due to friction:

$$-\rho g A_x S_{fx} \Delta x \tag{3.12}$$

in which S_{fx} is the friction slope in the x-direction. If only bed friction effects are considered, the friction slope can be assessed with the usual Manning formula:

$$S_{fx} = \frac{n_m^2 \bar{u}|\bar{u}|}{\bar{h}_x^{4/3}} \,. \tag{3.13}$$

The mass stored in the y-directed slot is assumed not to contribute to the flowing in the x-direction, thus is again neglected in the assessment of contributions (3.11) and (3.12). By joining all the previous terms and dividing by $\rho\Omega$, the following linear momentum equation can be obtained for the control volume of Fig. 3.1:

$$\frac{\partial \bar{q}_x}{\partial t} = -\frac{1}{\Delta x}\left(\frac{\bar{q}_x^2}{\bar{h}_x}\right)\Bigg|_{x_1}^{x_2} - \frac{1}{\Delta x}(g\zeta_x \bar{h}_x)\Big|_{x_1}^{x_2} - \frac{1}{\Delta y}\left(\frac{\bar{q}_x \bar{q}_y}{\bar{h}_x}\right)\Bigg|_{y_1}^{y_2} + g\bar{h}_x(S_{0x} - S_{fx}). \tag{3.14}$$

Ultimately, the application to an infinitesimal control volume gives the x-momentum equation written in differential conservation law form:

$$\frac{\partial \bar{q}_x}{\partial t} + \frac{\partial}{\partial x}\left(\frac{\bar{q}_x^2}{\bar{h}_x} + g\zeta_x \bar{h}_x\right) + \frac{\partial}{\partial y}\left(\frac{\bar{q}_x \bar{q}_y}{\bar{h}_x}\right) = g\bar{h}_x(S_{0x} - S_{fx}). \tag{3.15}$$

Similarly, the y-momentum equation can be derived:

$$\frac{\partial \bar{q}_y}{\partial t} + \frac{\partial}{\partial x}\left(\frac{\bar{q}_x \bar{q}_y}{\bar{h}_y}\right) + \frac{\partial}{\partial y}\left(\frac{\bar{q}_y^2}{\bar{h}_y} + g\zeta_y \bar{h}_y\right) = g\bar{h}_y(S_{0y} - S_{fy}). \tag{3.16}$$

Equations (3.4), (3.15) and (3.16) can be combined into a system of equations that can be written using the compact vector notation:

$$\frac{\partial \mathbf{U}}{\partial t} + \frac{\partial \mathbf{F}}{\partial x} + \frac{\partial \mathbf{G}}{\partial y} = \mathbf{S} \tag{3.17}$$

in which the vector $\mathbf{U}$ of the conserved variables, the flux vectors $\mathbf{F}$ and $\mathbf{G}$, and the source term $\mathbf{S}$ read:

$$\mathbf{U} = \begin{bmatrix} \bar{h} \\ \bar{q}_x \\ \bar{q}_y \end{bmatrix}, \quad \mathbf{F} = \begin{bmatrix} \bar{q}_x \\ \dfrac{\bar{q}_x^2}{\bar{h}_x} + g\zeta_x \bar{h}_x \\ \dfrac{\bar{q}_x \bar{q}_y}{\bar{h}_y} \end{bmatrix}, \quad \mathbf{G} = \begin{bmatrix} \bar{q}_y \\ \dfrac{\bar{q}_x \bar{q}_y}{\bar{h}_x} \\ \dfrac{\bar{q}_y^2}{\bar{h}_y} + g\zeta_y \bar{h}_y \end{bmatrix},$$

$$\mathbf{S} = \begin{bmatrix} 0 \\ g\bar{h}_x(S_{0x} - S_{fx}) \\ g\bar{h}_y(S_{0y} - S_{fy}) \end{bmatrix}. \tag{3.18}$$

Equation (3.17), coupled with the previous statements, actually represents a system of modified 2D shallow water equations with a peculiar definition of the set of unknown variables. In particular, the assumption that the water mass flowing in a slot has only one component of velocity (in the slot direction) ensures that Eq. (3.17) shows the classic structure of the 2D shallow water equations with the first terms of the $\mathbf{F}$ and $\mathbf{G}$ flux vectors coinciding with the second and third component of the vector $\mathbf{U}$ of the conserved variables, respectively. If $h < H$, then the water surface is below the ceiling, $\bar{h}$ reduces to h (the same holds for $\bar{h}_x$ and $\bar{h}_y$), and Eq. (3.17) returns to the usual system of the 2D shallow water equations (e.g. Toro, 2001). The geometrical properties of the control volume can easily be extended for $h \geq H$ considering the addition of two crossing vertical slots on the

top with dimensionless widths $k_x = T_x/\Delta x$ and $k_y = T_y/\Delta y$, respectively:

$$V = \begin{cases} \Omega h & \text{if } 0 \le h \le H \\ \Omega H \left[1 + (k_x + k_y - k_x k_y)\left(\dfrac{h}{H} - 1\right)\right] & \text{if } h \ge H \end{cases}$$
$$\bar{h} = \begin{cases} h & \text{if } 0 \le h \le H \\ H \left[1 + (k_x + k_y - k_x k_y)\left(\dfrac{h}{H} - 1\right)\right] & \text{if } h \ge H \end{cases} \tag{3.19}$$

$$A_x = \begin{cases} \Delta y\, h & \text{if } 0 \le h \le H \\ \Delta y\, H \left[1 + k_y\left(\dfrac{h}{H} - 1\right)\right] & \text{if } h \ge H \end{cases}$$
$$\bar{h}_x = \begin{cases} h & \text{if } 0 \le h \le H \\ H \left[1 + k_y\left(\dfrac{h}{H} - 1\right)\right] & \text{if } h \ge H \end{cases} \tag{3.20}$$

$$\zeta_x \bar{h}_x = \begin{cases} \dfrac{h^2}{2} & \text{if } 0 \le h \le H \\ H\left(h - \dfrac{H}{2}\right) + \dfrac{(h-H)^2}{2} k_y & \text{if } h \ge H \end{cases} \tag{3.21}$$

Similar expressions can be derived for A_y, $\bar{h}_y$, and $\zeta_y \bar{h}_y$. It can be noticed that these geometrical quantities are continuous functions of h, with a discontinuity in the derivative at $h = H$. This sudden change in the gradient is more severe for narrower slots.

Therefore, by the simple generalization of the classic Preissmann slot model described above, a 2D mixed flow can easily be modeled as an equivalent 2D free-surface flow occurring in a fixed integration element with peculiar composite shape, without the need of any special treatment for handling transitions between free-surface and pressurized conditions. In this way, the capability of dealing with the surcharging of the system can be extended to the 2D modelling, without modifying the governing equations. The high celerity values typical of the pressure

waves can be reproduced through a suitable setting of the slot widths. Finally, Eq. (3.17) easily reduces to the x- (or y-) split 2D shallow water equations when the velocity component in the y- (or x-) direction vanishes; in this case, the classic 1D geometrical schematization of the Preissmann slot model can be obtained if the width of the transverse slot is set to zero.

3.2.2 Properties of the equations

In this subsection, the eigenstructure of the governing equations is analyzed with regard to the conserved variables (Toro, 2001). For $h \geq H$, the Jacobian matrix $\mathbf{J_F}$ corresponding to the flux vector $\mathbf{F}$ defined in Eq. (3.18) is given by:

$$\mathbf{J_F} = \begin{bmatrix} 0 & 1 & 0 \\ \left\{ -\left(\frac{\bar{q}_x}{\bar{h}_x}\right)^2 + gH\left[\frac{1}{k_y} + \left(\frac{h}{H} - 1\right)\right]\right\} \frac{k_y}{k_x + k_y - k_x k_y} & 2\frac{\bar{q}_x}{\bar{h}_x} & 0 \\ -\frac{\bar{q}_x \bar{q}_y}{\bar{h}_y^2} \frac{k_y}{k_x + k_y - k_x k_y} & \frac{\bar{q}_y}{\bar{h}_y} & \frac{\bar{q}_x}{\bar{h}_y} \end{bmatrix} \tag{3.22}$$

while, for $h < H$, it reduces to the familiar form typical of the 2D shallow water equations:

$$\mathbf{J_F} = \begin{bmatrix} 0 & 1 & 0 \\ -\bar{u}^2 + gh & 2\bar{u} & 0 \\ -\bar{u}\bar{v} & \bar{v} & \bar{u} \end{bmatrix}. \tag{3.23}$$

The eigenvalues of $\mathbf{J_F}$ in Eq. (3.22) can be obtained after some algebra:

$$\lambda_1 = \bar{u} - c_x, \quad \lambda_2 = \frac{\bar{q}_x}{\bar{h}_y}, \quad \lambda_3 = \bar{u} + c_x \tag{3.24}$$

where the celerity c_x is a function of both h and $\bar{u}$ (for $h \geq H$):

$$c_x = \sqrt{\bar{u}^2 - \left\{\bar{u}^2 - gH\left[\frac{1}{k_y} + \left(\frac{h}{H} - 1\right)\right]\right\} \frac{k_y}{k_x + k_y - k_x k_y}}\,. \tag{3.25}$$

For the special case of $k_x = k_y = k$, the celerity is

$$c_x = \sqrt{\bar{u}^2 \frac{1-k}{2-k} + gH \frac{1}{2-k} \left[\frac{1}{k} + \left(\frac{h}{H} - 1 \right) \right]} \tag{3.26}$$

with k and H acting as geometric parameters. Moreover, in the particular case of a 1D flow along the x-direction, assuming k_x equal to zero in Eq. (3.25), c_x becomes a function of h only:

$$c_x = \sqrt{gH \left[\frac{1}{k_y} + \left(\frac{h}{H} - 1 \right) \right]}. \tag{3.27}$$

It can easily be verified that Eq. (3.27) is equivalent to the usual celerity formula $c = \sqrt{gA/b}$ applied to a composite rectangular section with the addition of a vertical slot above the crown. For $h = H$, Eq. (3.27) shows a discontinuity in the celerity value that can be very strong for low values of k.

A similar analysis can be performed for the Jacobian matrix $\mathbf{J_G}$ corresponding to the flux vector $\mathbf{G}$. The classic 2D shallow water equations are known to be strictly hyperbolic for a wet bed. The strict hyperbolicity of Eq. (3.17) is confirmed even for $h \geq H$, since the Jacobian matrices $\mathbf{J_F}$ and $\mathbf{J_G}$ admit three real eigenvalues which, in addition, are all distinct.

3.3 Numerical scheme

Equation (3.17) is discretized over a uniform Cartesian grid with dimensions $\Delta x \times \Delta y$ using the following explicit finite volume scheme, based on the Strang splitting of the source term (Toro, 1999):

$$\begin{aligned}
\mathbf{U}^{\star}_{i,j} &= \mathbf{U}^{n}_{i,j} + \frac{\Delta t}{2}\mathbf{S}^{n}_{i,j} \\
\mathbf{U}^{\star\star}_{i,j} &= \mathbf{U}^{\star}_{i,j} - \frac{\Delta t}{\Delta x}\left[\mathbf{F}_{i+\frac{1}{2},j} - \mathbf{F}_{i-\frac{1}{2},j}\right] - \frac{\Delta t}{\Delta y}\left[\mathbf{G}_{i,j+\frac{1}{2}} - \mathbf{G}_{i,j-\frac{1}{2}}\right] \\
\mathbf{U}^{n+1}_{i,j} &= \mathbf{U}^{\star\star}_{i,j} + \frac{\Delta t}{2}\mathbf{S}^{\star\star}_{i,j}\,.
\end{aligned} \tag{3.28}$$

According to this succession of updates, the cell-average $\mathbf{U}_{i,j}$ in the i,j-cell evolves from the time level n to the time level $n+1$ (being $\Delta t = t^{n+1} - t^{n}$ the computational time interval). In a single step, both x and y fluxes are taken into account through the intercell numerical fluxes $\mathbf{F}_{i\pm1/2,j}$ and $\mathbf{G}_{i,j\pm1/2}$ (in the x- and y-directions, respectively) calculated at the intermediate state $\mathbf{U}^{\star}$. Forcing effects are involved by the cell-averaged source term vector $\mathbf{S}_{i,j}$ which is evaluated at the states $\mathbf{U}^{n}$ and $\mathbf{U}^{\star\star}$ in Eq. (3.28).

The Slope Limiter Centred (SLIC) scheme proposed by Toro (1999) is here adopted in order to estimate the numerical fluxes. This scheme is characterized by three steps.

1. According to the MUSCL-Hancock approach, boundary extrapolated values are computed at the interfaces of each cell. For the x-axis direction, it reads:

$$\begin{aligned}
\mathbf{U}^{L}_{i+\frac{1}{2},j} &= \mathbf{U}^{n}_{i,j} + \frac{1}{2}\mathbf{\Phi}^{+}_{i-\frac{1}{2},j}\left(\mathbf{U}^{n}_{i,j} - \mathbf{U}^{n}_{i-1,j}\right) \\
\mathbf{U}^{R}_{i+\frac{1}{2},j} &= \mathbf{U}^{n}_{i+1,j} - \frac{1}{2}\mathbf{\Phi}^{-}_{i+\frac{3}{2},j}\left(\mathbf{U}^{n}_{i+2,j} - \mathbf{U}^{n}_{i+1,j}\right)
\end{aligned} \tag{3.29}$$

   in which the superscripts L and R indicate the left- and right-hand extrapolated states at each cell interface respectively, and $\mathbf{\Phi}$ represents a suitable

slope limiter function which enforces the Total Variation Diminishing (TVD) property, with the aim of minimizing spurious oscillations in proximity of strong gradients of the variables (Hirsch, 1990). In Eq. (3.29), the limiters $\boldsymbol{\Phi}^{\pm}$ depend on the corresponding ratios $\boldsymbol{r}^{\pm}$, which are defined as:

$$\boldsymbol{r}^{+}_{i-\frac{1}{2},j} = \frac{\mathbf{U}^{n}_{i+1,j} - \mathbf{U}^{n}_{i,j}}{\mathbf{U}^{n}_{i,j} - \mathbf{U}^{n}_{i-1,j}}, \qquad \boldsymbol{r}^{-}_{i+\frac{3}{2},j} = \frac{\mathbf{U}^{n}_{i+1,j} - \mathbf{U}^{n}_{i,j}}{\mathbf{U}^{n}_{i+2,j} - \mathbf{U}^{n}_{i+1,j}}. \tag{3.30}$$

In this work, the classic slope limiter function of Van Leer (1974) is adopted:

$$\phi\left(r\right) = \begin{cases} \dfrac{r + |r|}{1 + r} & \text{if } r > 0 \\ 0 & \text{if } r \leq 0 \end{cases} \tag{3.31}$$

Extrapolations along the y-direction can be performed in a similar way. Moreover, intercell boundary values of the variables A_x, $\bar{h}_x$, and $\zeta_x \bar{h}_x$ (similarly for A_y, $\bar{h}_y$, and $\zeta_y \bar{h}_y$) are also reconstructed on the basis of the geometrical relations (3.20) and (3.21).

2. The boundary extrapolated variables are evolved by an half time step $\Delta t/2$ according to the following relations:

$$\begin{aligned} \overline{\mathbf{U}}^{L}_{i+\frac{1}{2},j} = \mathbf{U}^{L}_{i+\frac{1}{2},j} &- \frac{\Delta t}{2\Delta x}\left[\mathbf{F}\left(\mathbf{U}^{L}_{i+\frac{1}{2},j}\right) - \mathbf{F}\left(\mathbf{U}^{R}_{i-\frac{1}{2},j}\right)\right] \\ &- \frac{\Delta t}{2\Delta y}\left[\mathbf{G}\left(\mathbf{U}^{L}_{i,j+\frac{1}{2}}\right) - \mathbf{G}\left(\mathbf{U}^{R}_{i,j-\frac{1}{2}}\right)\right], \end{aligned} \tag{3.32a}$$

$$\begin{aligned} \overline{\mathbf{U}}^{R}_{i+\frac{1}{2},j} = \mathbf{U}^{R}_{i+\frac{1}{2},j} &- \frac{\Delta t}{2\Delta x}\left[\mathbf{F}\left(\mathbf{U}^{L}_{i+\frac{3}{2},j}\right) - \mathbf{F}\left(\mathbf{U}^{R}_{i+\frac{1}{2},j}\right)\right] \\ &- \frac{\Delta t}{2\Delta y}\left[\mathbf{G}\left(\mathbf{U}^{L}_{i+1,j+\frac{1}{2}}\right) - \mathbf{G}\left(\mathbf{U}^{R}_{i+1,j-\frac{1}{2}}\right)\right]. \end{aligned} \tag{3.32b}$$

Evolutions along the y-direction can be performed in a similar way. Again,

evolved values of A_x, $\bar{h}_x$, and $\zeta_x \bar{h}_x$ (similarly for A_y, $\bar{h}_y$, and $\zeta_y \bar{h}_y$) are estimated through Eqs. (3.20) and (3.21).

3. Godunov fluxes at the intercell boundaries are evaluated by the First-Order Centred (FORCE) flux (Toro, 1999), which is the arithmetic mean of the Lax-Friedrichs (LF) and Richtmyer (RI) fluxes:

$$\mathbf{F}^{\mathrm{FORCE}}_{i+\frac{1}{2},j} = \frac{1}{2}\left(\mathbf{F}^{\mathrm{LF}}_{i+\frac{1}{2},j} + \mathbf{F}^{\mathrm{RI}}_{i+\frac{1}{2},j}\right). \tag{3.33}$$

The LF flux is computed as:

$$\mathbf{F}^{\mathrm{LF}}_{i+\frac{1}{2},j} = \frac{1}{2}\left[\mathbf{F}\left(\overline{\mathbf{U}}^{L}_{i+\frac{1}{2},j}\right) + \mathbf{F}\left(\overline{\mathbf{U}}^{R}_{i+\frac{1}{2},j}\right)\right] + \frac{1}{2}\frac{\Delta x}{\Delta t}\left(\overline{\mathbf{U}}^{L}_{i+\frac{1}{2},j} - \overline{\mathbf{U}}^{R}_{i+\frac{1}{2},j}\right) \tag{3.34}$$

while the RI flux is evaluated as:

$$\mathbf{F}^{\mathrm{RI}}_{i+\frac{1}{2},j} = \mathbf{F}\left(\mathbf{U}^{\mathrm{RI}}_{i+\frac{1}{2},j}\right) \tag{3.35}$$

with:

$$\mathbf{U}^{\mathrm{RI}}_{i+\frac{1}{2},j} = \frac{1}{2}\left(\overline{\mathbf{U}}^{L}_{i+\frac{1}{2},j} + \overline{\mathbf{U}}^{R}_{i+\frac{1}{2},j}\right) + \frac{1}{2}\frac{\Delta t}{\Delta x}\left[\mathbf{F}\left(\overline{\mathbf{U}}^{L}_{i+\frac{1}{2},j}\right) - \mathbf{F}\left(\overline{\mathbf{U}}^{R}_{i+\frac{1}{2},j}\right)\right]. \tag{3.36}$$

Similar relations can be written for the vector $\mathbf{G}$ of fluxes in the y-direction.

This numerical procedure for solving the homogeneous problem is second-order accurate in space and time. With regard to stability, the explicit unsplit MUSCL-Hancock scheme applied to the 2D linear advection equations with constant velocity components $a_x > 0$ and $a_y > 0$ (in the x and y directions, respectively) has the stability range (Toro, 1999):

$$a_x \frac{\Delta t}{\Delta x} + a_y \frac{\Delta t}{\Delta y} \leq 1. \tag{3.37}$$

The extension of this condition to the non-linear problem (3.17) and (3.18) leads to the stability restriction:

$$\max_{i,j}\left[\left(\left|\frac{\bar{q}_x}{\bar{h}_x}\right|+c_x\right)\frac{\Delta t}{\Delta x}+\left(\left|\frac{\bar{q}_y}{\bar{h}_y}\right|+c_y\right)\frac{\Delta t}{\Delta y}\right]\leq 1 \tag{3.38}$$

involving the wave speeds c_x and c_y of the hyperbolic system. The condition expressed by Eq. (3.38) is certainly satisfied if the computational time step Δt is calculated as follows:

$$\Delta t=\frac{1}{2}\,Cr\min_{i,j}\left(\frac{\Delta x}{\left|\frac{\bar{q}_x}{\bar{h}_x}\right|+c_x},\frac{\Delta y}{\left|\frac{\bar{q}_y}{\bar{h}_y}\right|+c_y}\right) \tag{3.39}$$

where Cr denotes the Courant number (≤ 1).

The effectiveness and robustness of this numerical method for solving shallow water equations in dam-break modelling had been extensively tested on the basis of both analytical and real field test cases (see, for example, Aureli et al., 2008).

3.4 Numerical tests

In this section the model previously described is validated by comparing numerical results with both exact solutions of 1D discontinuous initial value problems and reference radial solutions of idealized test cases with cylindrical symmetry. All validation tests concern frictionless problems with horizontal bathymetry. Finally, applications to the experimental case of a steady flow through an arch bridge and to a field-scale dam-break case are presented.

3.4.1 1D test cases with exact solution

The ability of the numerical model to simulate highly transient mixed flows is first assessed on the basis of 1D test problems with exact solution, which can be obtained from the exact Riemann solver proposed by Kerger et al. (2011b).

All tests consider a 20 m long frictionless horizontal duct characterized by a rectangular cross-section with height H and width B both equal to 1 m. The computational domain $[-10, 10]\,\mathrm{m} \times [0, 1]\,\mathrm{m}$ is discretized by means of $N_x = 2000 \times N_y = 10$ rectangular cells with size $\Delta x = 0.01\,\mathrm{m} \times \Delta y = 0.1\,\mathrm{m}$. Since each computational cell is provided with two fictitious vertical slots aligned along the two plane directions x and y, the closed conduit presents N_y longitudinal slots instead of the classic single slot that is ideally introduced above the pipe crown when the slot concept is applied to the 1D equations. The width T_y of the slots in the longitudinal direction is assumed to be equal to a small fraction of the cross-sectional grid size Δy ($k_y = T_y/\Delta y$). Therefore, an array of longitudinal slots with fixed dimensionless width k_y conceptually replaces a single slot with the same value of the ratio of slot width to conduit width. Moreover, in the simulation of 1D problems, the dimensionless width of the transverse slots ($k_x = T_x/\Delta x$) should be assumed sufficiently small in order to limit the artificial increase in the pipe volume.

Table 3.1 summarizes the test conditions and gives the initial left and right values for the three test cases considered (in the following, the overbar above the velocity components is omitted for simplicity). The discontinuity in the initial states is located at the origin of the x-axis. Some of these tests have already been employed in Chapter 2. In all the simulations, the stability condition stated by Eq. (3.39) is adopted with the Courant number Cr equal to 0.9.

TABLE 3.1 – Test conditions for three 1D discontinuous initial-value problems with analytical solution

Test	h_L(m)	u_L(m/s)	h_R(m)	u_R(m/s)	Description
A1	0.8	2.0	0.8	−2.0	Two transition shocks
A2	3.0	0.0	0.5	0.0	Left transition wave and right shock
A3	1.5	1.0	1.5	−1.0	Two waterhammer waves

Test A1

Test A1 is characterized by an initial condition representing two colliding uniform free-surface flows with the same water depth but opposite velocities. This test coincides with T3 in Section 2.3.2. The impingement of the two incoming flows produces a pressurized intermediate state which expands thanks to two transition shock waves traveling in opposite directions. If only one half of the domain is considered, this situation is equivalent to the propagation of a pipe-filling surge originated by the sudden closure of the downstream end of a conduit.

Figure 3.2 compares the numerical results of two simulations carried out by setting k_y at 0.01 and 0.1 ($k_x = 0.001$ for both simulations) with the corresponding 1D solutions obtained from the exact Riemann solver by considering a single longitudinal slot with the same dimensionless width. The numerical model seems to correctly resolve the abrupt transition between free-surface and surcharged regimes. However, spurious oscillations appear behind the shock wave, as expected. Figure 3.2 shows that the strength of the numerical oscillations at flow transitions slightly depends on the slot width.

A sensitivity analysis is carried out on the basis of the same test conditions in order to highlight the effect of the longitudinal mesh size Δx on the numerical results. Figure 3.3 compares pressure head and velocity profiles at $t = 0.5\,\mathrm{s}$ extracted from three different simulations performed with $\Delta x = 0.01, 0.05$ and

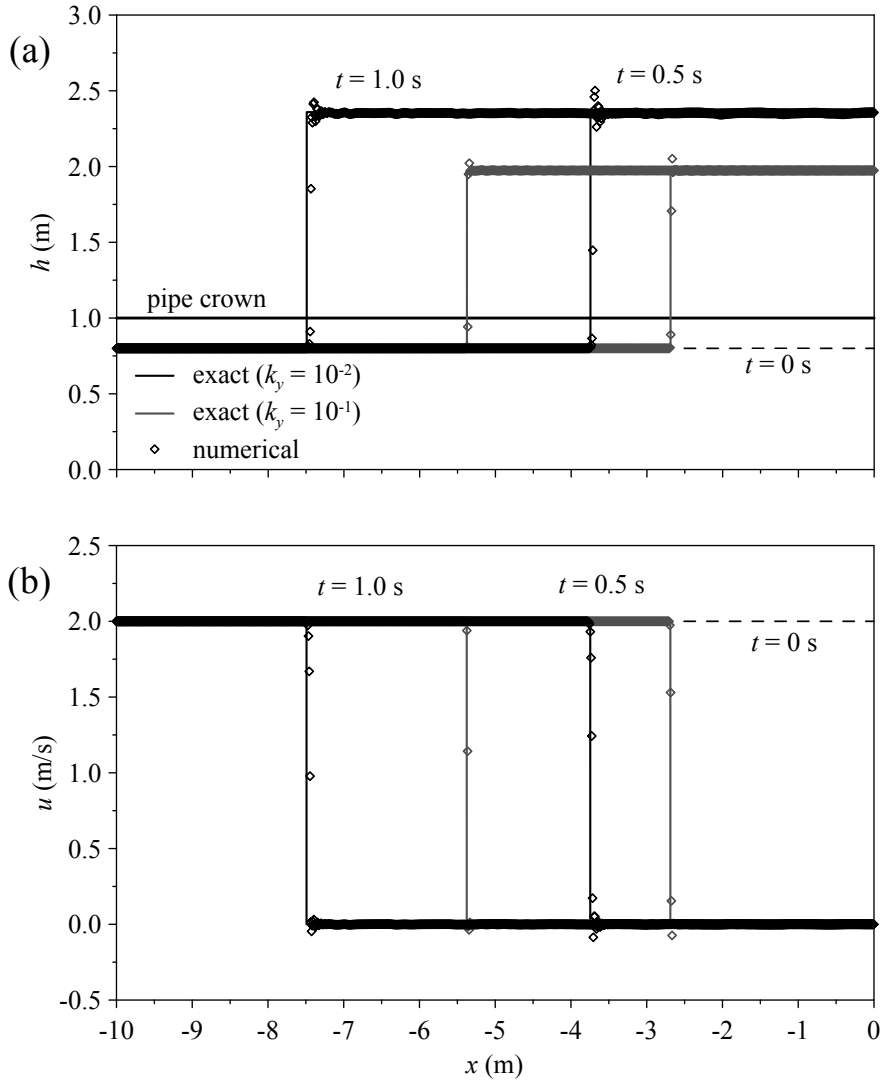

FIGURE 3.2 – Test A1: comparison between exact solution and numerical results at $t = 0.5\,\mathrm{s}$ and $t = 1\,\mathrm{s}$; (a) pressure head, (b) velocity. Two data series are reported, corresponding to $k_y = 0.01$ and $k_y = 0.1$ respectively. Only the sub-domain $[-10, 0]\,\mathrm{m}$ is represented for clarity

0.1 m. All the other model parameters remain unchanged. The numerical model shows a slight shift in the location of the discontinuity. Furthermore, it spreads the discontinuity over a small number of grid cells, which does not seem to be influenced by Δx. For this reason, the coarser the mesh, the more diffusive the numerical profiles appear. Similarly, the finer the mesh, the shorter the space interval along which spurious oscillations at the transition front vanish. Moreover, oscillation amplitude seems insensitive to grid size.

The deviation of the numerical pressure head and velocity profiles from the reference solution provided by the exact Riemann solver can be quantified by the L_1-error, commonly used for conservation laws (LeVeque, 2002):

$$E_{L_1}(h) = \Delta x \sum_{i=1}^{N} |h_{num} - h_{exact}|,\ E_{L_1}(u) = \Delta x \sum_{i=1}^{N} |u_{num} - u_{exact}|. \qquad (3.40)$$

Table 3.2 reports the results obtained for $t = 0.5$ s considering half of the computational domain, i.e. $[-10, 0]$ m. It can be noticed that grid refinement induces a reduction in the pressure head error. On the contrary, the overall error in the velocity profile is slightly affected by the grid spacing in the Δx-range considered. Anyway, these errors are mainly attributable to the numerical approximation in the reconstruction of the transition bore.

The sensitivity of the numerical results to the width of the transverse slot

TABLE 3.2 – Test A1: sensitivity analysis on longitudinal grid size based on the pressure head and velocity profiles at $t = 0.5$ s. The L_1-norms are calculated with reference to the exact solution over the sub-domain $[-10, 0]$ m

Δx	$E_{L_1}(h)(\mathrm{m}^2)$	$E_{L_1}(u)(\mathrm{m}^2/\mathrm{s})$
0.01	0.840	0.557
0.05	0.903	0.559
0.10	0.980	0.559

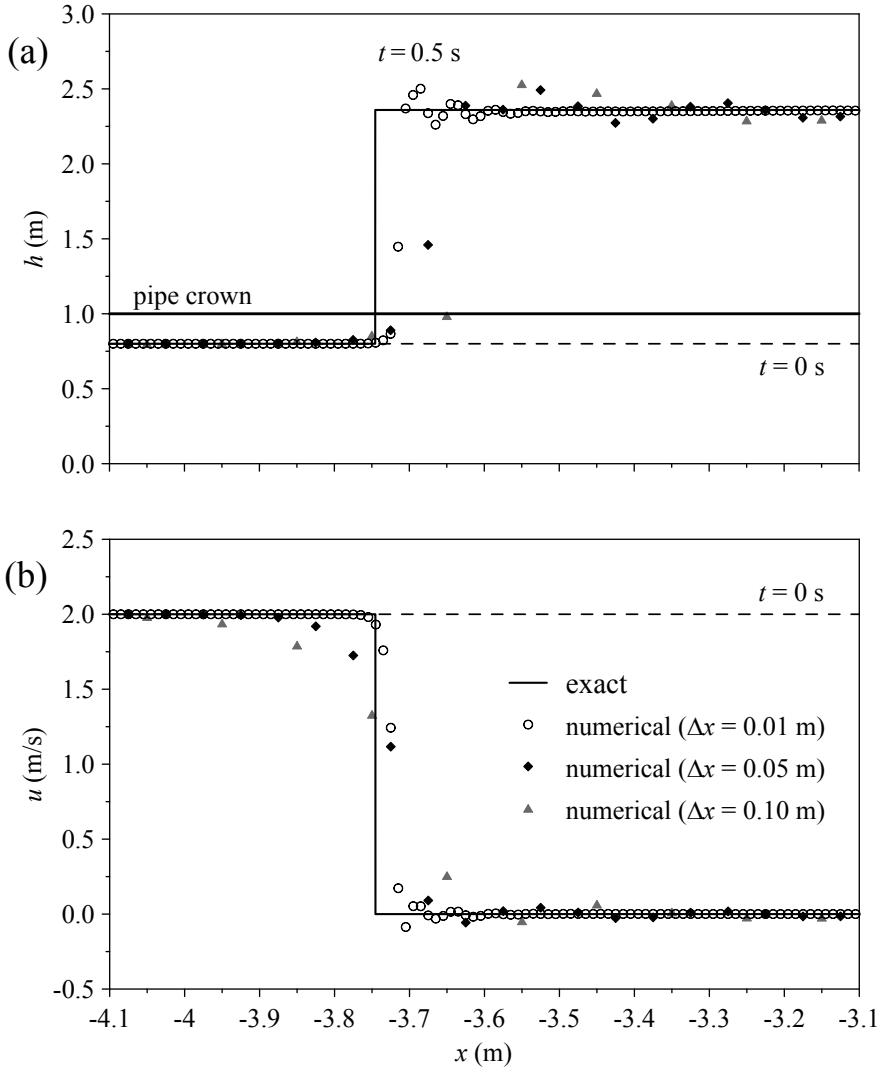

FIGURE 3.3 – Test A1: convergence analysis based on three different longitudinal grid sizes ($\Delta x = 0.01$, 0.05, and 0.10 m). Pressure head (a) and velocity (b) profiles at $t = 0.5$ s are shown. The x-axis is limited to the interval $[-4.1, -3.1]$ m for clarity

can be assessed by looking at Fig. 3.4, in which three pressure head and velocity profiles at $t = 0.5\,\mathrm{s}$, computed using three different values of the dimensionless slot width k_x ($10^{-2}, 10^{-3}$ and 10^{-4}), are compared with the exact solution ($k_y = 0.01$). Since the reference 1D solution does not take into account the fictitious increment of the conduit volume induced by the system of transverse slots, it can be expected that the agreement between reference and numerical solutions improves with k_x decreasing. This trend is evident in Table 3.3, which shows the deviation between predicted and reference pressure head and velocity profiles at $t = 0.5\,\mathrm{s}$, estimated through the L_1-norm defined in Eq. (3.40) for the sub-domain $[-10, 0]\,\mathrm{m}$. The pipe filling bore is actually well reproduced provided that k_x is set at least one/two orders of magnitude lower than k_y. If the width of the transverse slot is assumed of the same order of magnitude as the longitudinal one, the celerity of the sharp transition wave is underestimated, as well as the height of the jump in pressure head caused by the wave transit.

TABLE 3.3 – Test A1: sensitivity analysis on the parameter k_x based on the pressure head and velocity profiles at $t = 0.5\,\mathrm{s}$. The L_1-norms are calculated with reference to the exact solution over the sub-domain $[-10, 0]\,\mathrm{m}$

k_x	$E_{L_1}(h)(\mathrm{m}^2)$	$E_{L_1}(u)(\mathrm{m}^2/\mathrm{s})$
10^{-4}	0.788	0.518
10^{-3}	0.841	0.557
10^{-2}	1.324	0.916

Test A2

Test A2 represents a sort of "dam-break" problem in which a wall (located at $x = 0\,\mathrm{m}$) initially separates a pressurized left state from a free-surface right state (see Table 3.1). This test coincides with T1 in Section 2.3.2. The solution consists of a free-surface shock wave propagating downstream and a left rarefaction

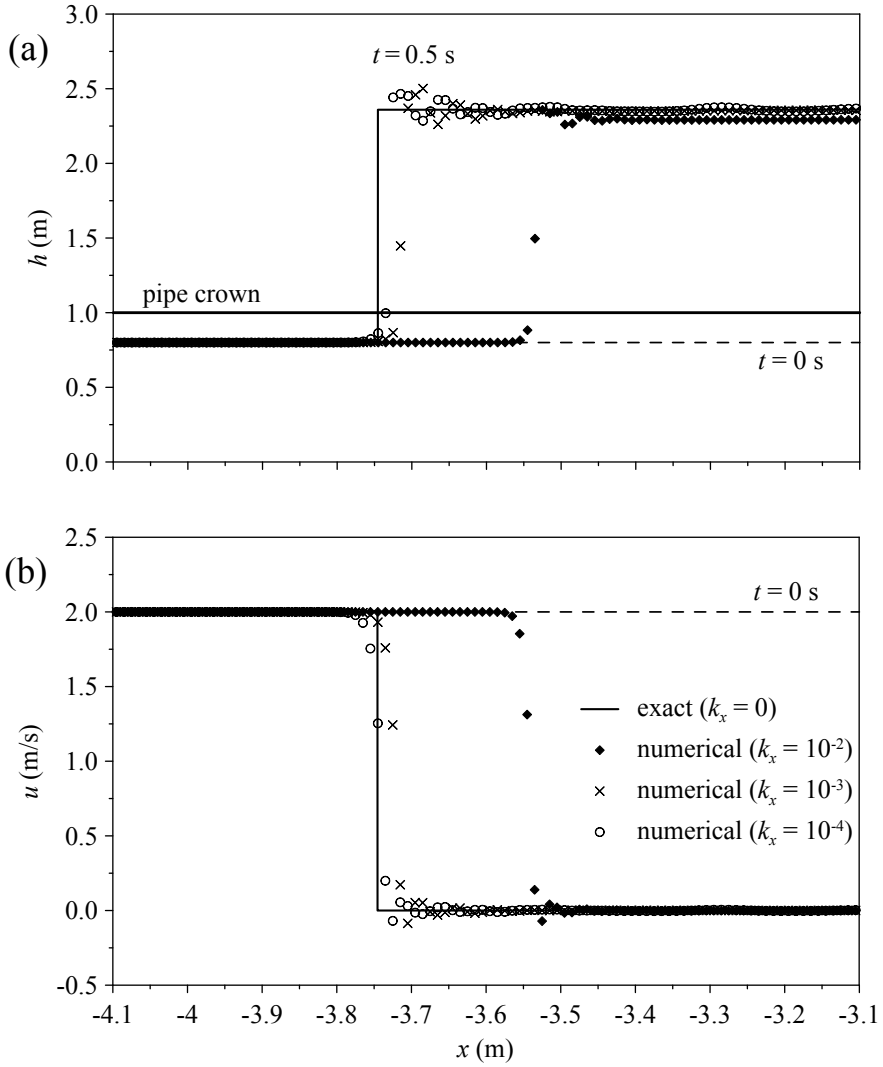

FIGURE 3.4 – Test A1: sensitivity analysis on the width of the transverse slot ($k_x = 10^{-2}, 10^{-3}$ and 10^{-4}). Pressure head (a) and velocity (b) profiles at $t = 0.5$ s are shown. The x-axis is limited to the interval $[-4.1, -3.1]$ m for clarity

wave along which a smooth transition between free-surface and pressurized flow occurs (Fig. 3.5). This transition rarefaction wave appears to be very steep in the pressurized portion and shows a considerable spread in correspondence with the flow transition. This behavior is due to the fact that the left eigenvalue is practically constant where the flow is pressurized and changes considerably across the crown of the closed conduit.

Figure 3.5 shows pressure head and velocity profiles at $t = 0.3\,\mathrm{s}$ computed on the basis of two different values of the model parameter k_x ($k_x = 10^{-3}$ and 10^{-4}). The numerical profiles (especially in the portion corresponding to the rarefaction wave) are rather sensitive to the dimensionless slot width k_x, and a good agreement with the solution of the exact Riemann solver is achieved with $k_x = 10^{-4}$. The free-surface intermediate state located between the two waves (star region) is well reproduced by the numerical model. With reference to these simulations (not involving inflow or outflow contributions), at $t = 0.3\,\mathrm{s}$, after approximately 2000 computational time steps, the relative volume conservation error (with reference to the initial water volume) is in the order of 10^{-13}, independently of the value of k_x.

Table 3.4 provides quantitative information on the overall accuracy of the numerical reconstruction of pressure head and velocity profiles at $t = 0.3\,\mathrm{s}$ for different longitudinal grid sizes. The L_1-error norms, calculated by applying Eq. (3.40) over the total domain $[-10, 10]\,\mathrm{m}$, show a trend towards pointwise convergence of the numerical profiles to the reference solution as the grid is refined. In particular, if too coarse a mesh is adopted, excessive numerical spreading of the rarefaction and shock waves occurs, with significant inaccuracy in the prediction of the intermediate state in the star region.

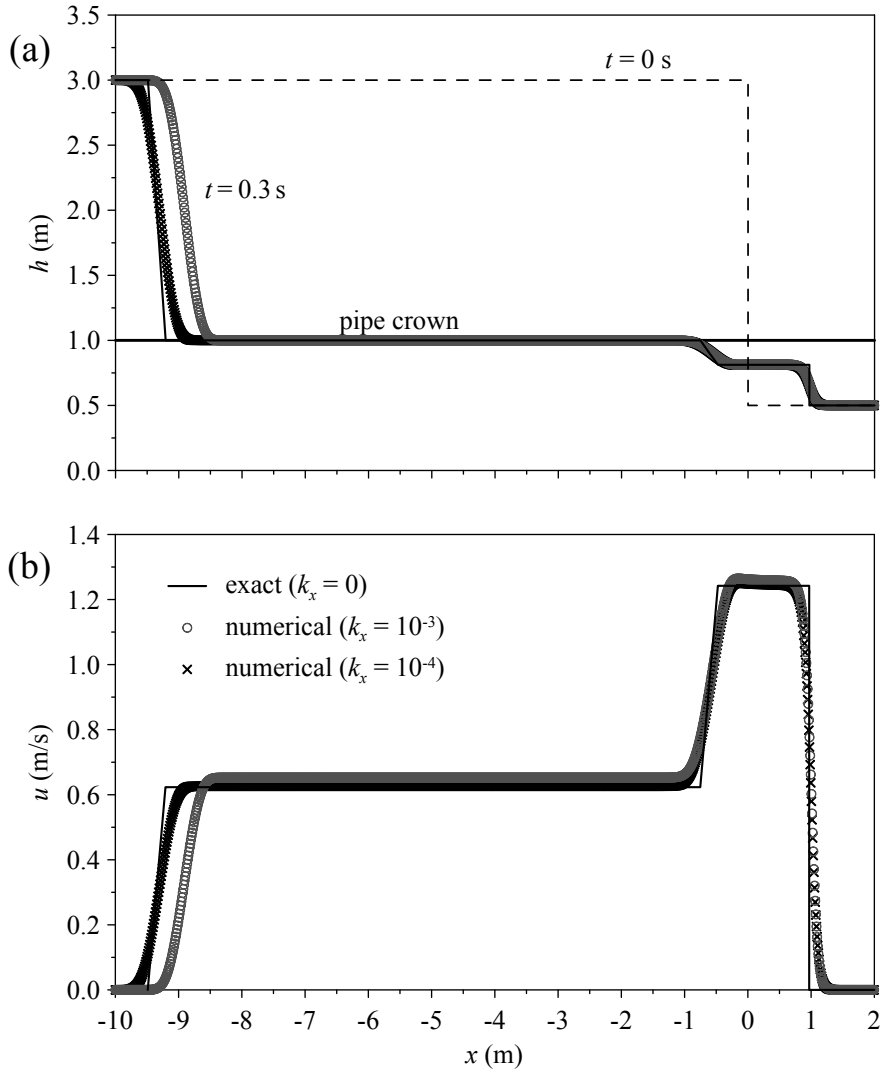

FIGURE 3.5 – Test A2: comparison between exact solution and numerical results at $t = 0.3$ s; (a) pressure head, (b) velocity. Profiles obtained by setting two different widths for the transverse slot ($k_x = 10^{-3}$ and 10^{-4}) are shown. Only the sub-domain $[-10, 2]$ m is represented for clarity

TABLE 3.4 – Test A2: sensitivity analysis on longitudinal grid size based on the pressure head and velocity profiles at $t = 0.3\,\mathrm{s}$ ($k_y = 10^{-2}$, $k_x = 10^{-4}$). The L_1-norms are calculated with reference to the exact solution over the total computational domain $[-10, 10]\,\mathrm{m}$

Δx	$E_{L_1}(h)(\mathrm{m}^2)$	$E_{L_1}(u)(\mathrm{m}^2/\mathrm{s})$
0.01	0.223	0.232
0.05	0.551	0.602
0.10	0.807	0.845

Test A3

Finally, Test A3 involves a fully pressurized flow and aims at assessing the model's capability of simulating water hammer transients. The initial data refer to two colliding pressurized flows moving with opposite velocities in a rectangular duct. The same test can simulate the stopping of a pressurized uniform flow caused by the instantaneous closure of a downstream valve. A Preissmann slot with a size of 0.001% of the conduit width is adopted, thus the propagating pressure wave is modeled by means of a gravity wave traveling with a celerity of approximately 990 m/s. This value is realistic in water hammer phenomena. Figure 3.6 shows numerical pressure head and velocity profiles at $t = 0.003\,\mathrm{s}$ and $t = 0.008\,\mathrm{s}$, and the reference solution derived from the exact Riemann solver. The reference solution is accurately reproduced by the numerical model and, in particular, the water hammer wave is well resolved without spurious oscillations.

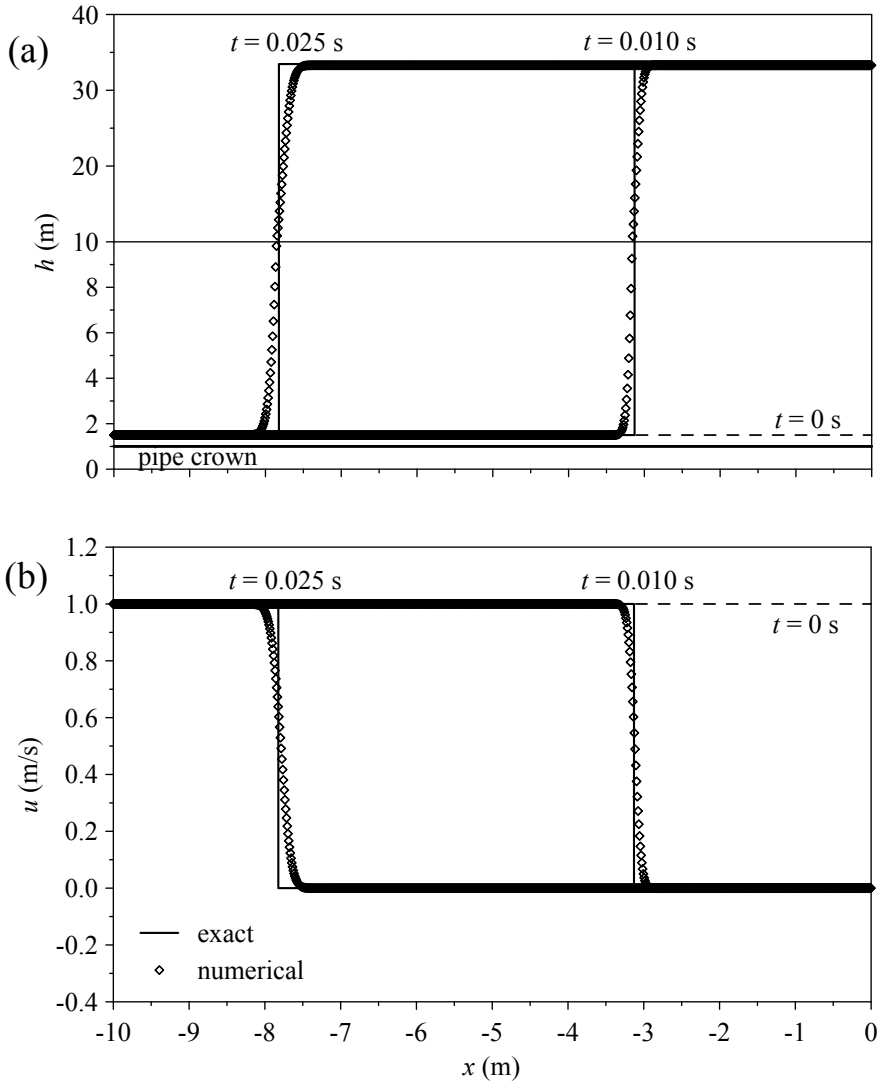

FIGURE 3.6 – Test A3: comparison between exact solution (pressure wave speed of approximately 990 m/s) and numerical results at $t = 0.003$ s and $t = 0.008$ s; (a) pressure head, (b) velocity. Only the sub-domain $[-10, 0]$ m is represented for clarity

3.4.2 2D test cases with reference solution

The capability of the proposed model of predicting 2D transient mixed flows is assessed in this subsection. In the literature, numerical schemes based on the 2D shallow water equations are often validated by comparison with dam-break test cases with cylindrical symmetry, namely the circular dam-break and the shock-focusing problems (e.g. Alcrudo and García-Navarro, 1993; Liska and Wendroff, 1999; Toro, 2001). In this work, these well-known test cases are modified in order to set up 2D discontinuous initial-value problems capable of inducing propagation phenomena involving transitions between free-surface and pressurized flow. Table 3.5 summarizes the test conditions for the two cases considered here.

Given the cylindrical symmetry of the problem, a 1D radial solution can be obtained by solving the following 1D system:

$$\frac{\partial \mathbf{U}}{\partial t} + \frac{\partial \mathbf{F}}{\partial r} = \mathbf{S}_r \tag{3.41}$$

where

$$\mathbf{U} = \begin{bmatrix} \tilde{h} \\ u_r \tilde{h} \end{bmatrix}, \ \mathbf{F} = \begin{bmatrix} u_r \tilde{h} \\ u_r^2 \tilde{h} + \dfrac{g}{2k_r}\left[\tilde{h}^2 + H^2\left(k_r - 1\right)\right] \end{bmatrix}, \ \mathbf{S}_r = -\frac{1}{r}\begin{bmatrix} u_r \tilde{h} \\ u_r^2 \tilde{h} \end{bmatrix} \tag{3.42}$$

$\mathbf{S}_r$ being the source term induced by the metrics. In Eq. (3.42), r is the radial

TABLE 3.5 – Test conditions for two 2D discontinuous initial-value problems with reference solution. For both tests $u_L = u_R = 0$

Test description	Domain (m)	h_L (m)	h_R (m)	R (m)	H (m)
Mixed circular dam-break	$[25, 50] \times [25, 50]$	10.0	1.0	11.0	5.0
Mixed shock-focusing	$[0, 1.5] \times [0, 1.5]$	0.2	1.0	0.35	1.03

coordinate, u_r is the radial velocity, and $\tilde{h}$ is an average depth defined as $H + k_r(h - H)$, being k_r the ratio between the length of the free-surface arch and the circumferential length at a fixed radial distance. Accordingly, k_r is a geometrical parameter denoting the dimensionless slot width if $\tilde{h} > H$; it reduces to unity if $\tilde{h} \leq H$.

Actually, a 1D radial solution obtained from a very fine mesh can be considered a good approximation of the exact solution. All reference solutions described in the following are obtained from numerical simulations performed with a 1D Preissmann slot model (described in Section 1.3), properly modified in order to take into account the additional radial source term.

Mixed circular dam-break problem

In the original circular dam-break test case (see Liska and Wendroff, 1999), a 10 m high water column with radius equal to 11 m is placed in the middle of a 50 m $\times$ 50 m square horizontal frictionless domain. Around, quiescent water has an initial depth equal to 1 m. In this work, a 5 m high ceiling is introduced over the whole domain, in such a way that the central part of the domain is initially pressurized (see Fig. 3.7). The sudden release of the water column generates a wave system characterized by a flow regime transition.

Figure 3.8 shows the comparison between 1D radial solution and diagonal ($y = x$) pressure head and velocity profiles computed by the full 2D model at selected times ($t = 0.1, 0.3$, and 0.7 s). The reference radial solution is obtained by numerically solving Eq. (3.41) over the domain $[25, 50]$ m discretized through a very fine uniform mesh consisting of 4000 cells. Due to geometrical symmetry, the 2D simulation is restricted to the sub-domain $[25, 50]$ m $\times$ $[25, 50]$ m, which is divided into 501 $\times$ 501 uniform computational cells. The Courant number is set equal to 0.9. From the cylindrical symmetry of the problem, it ensues that no preferential streamwise direction is recognizable *a priori* in the 2D simulation.

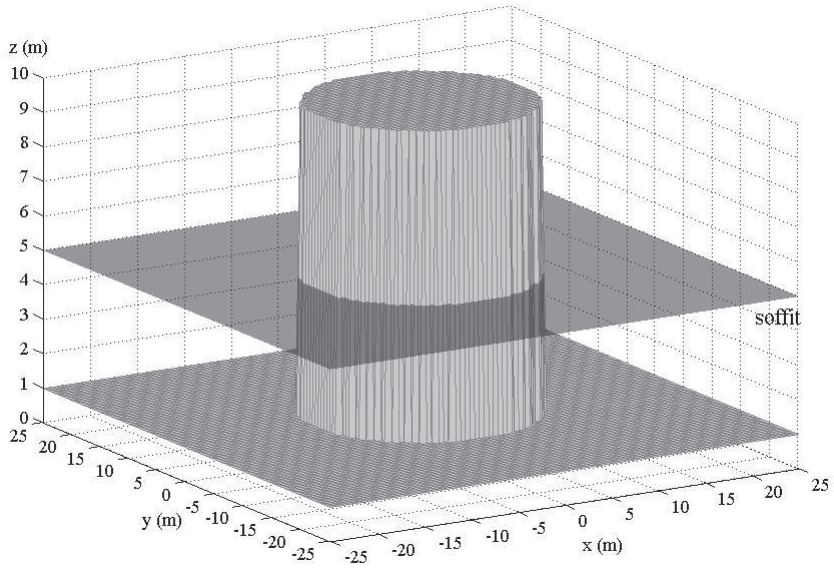

FIGURE 3.7 – Mixed circular dam-break test: sketch of the initial conditions

Therefore, it is reasonable to adopt the same slot size for both systems of parallel slots aligned along the Cartesian axes ($k_x = k_y = 0.01$). Moreover, in order to make the 1D radial solution (obtained by adding a single longitudinal slot) comparable with the full 2D solution (computed in the presence of a lattice of orthogonal slots), the width of the single 1D slot is assumed to be double the size of each group of parallel slots in the full 2D modelling, i.e. $k_r = 0.02$. In this way, the two models ideally contain the same supplementary volume above the conduit crown.

Figure 3.8 highlights the fact that the 2D numerical results fit the reference solution reasonably well and that the 2D model is capable of satisfactorily reproducing both the depressurization of the water column generated by the inward-propagating rarefaction wave and the evolution of the following fully free-surface flow with a circular shock wave expanding outwards. Since axial and

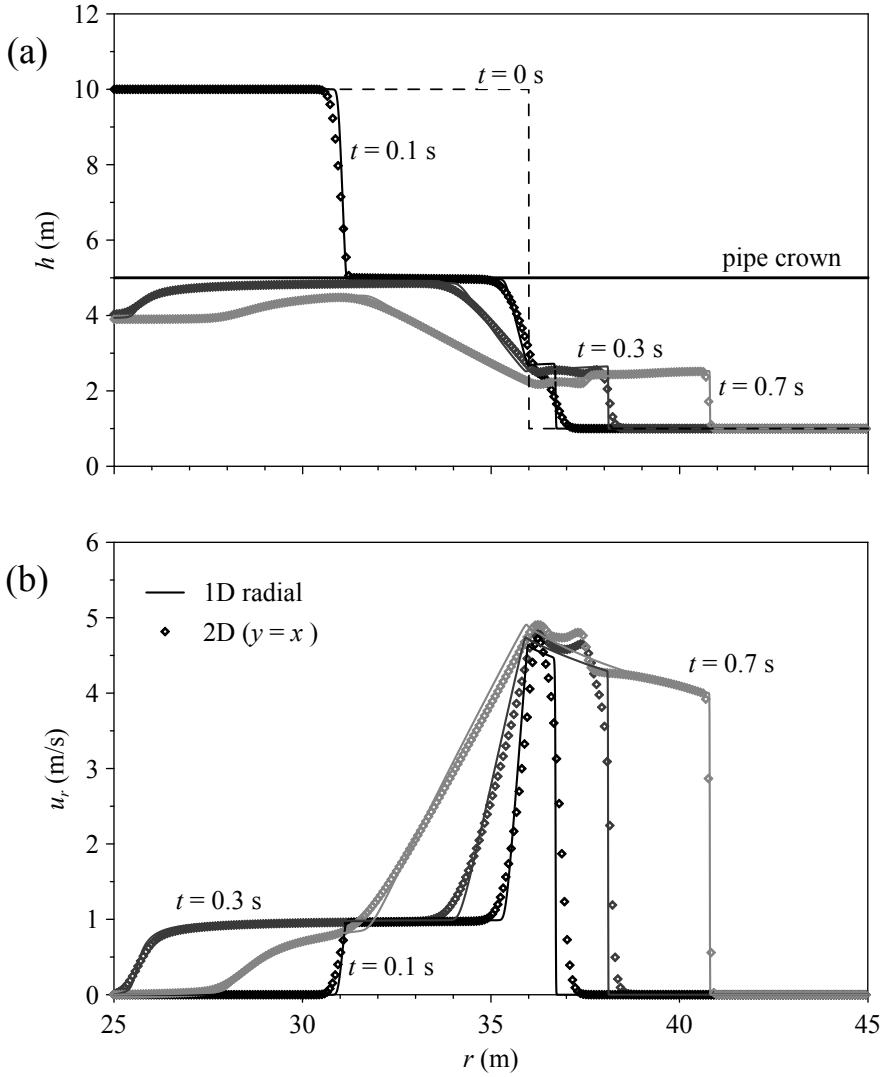

FIGURE 3.8 – Mixed circular dam-break test: comparison between reference 1D radial solution and 2D numerical profiles along $y = x$ at $t = 0.1, 0.3$, and 0.7 s; (a) pressure head, (b) velocity. Only the radial sub-domain $[25, 45]$ m is represented for clarity

diagonal profiles are almost undistinguishable, only diagonal profiles are shown in Fig. 3.8 for the sake of clarity. Hence, the 2D numerical solution excellently preserves the circular symmetry despite the Cartesian mesh.

Mixed shock-focusing problem

The classic shock-focusing test case is commonly defined in a dimensionless context (see, for example, Liska and Wendroff, 1999). In this work, an analogous test is carried out on a dimensional square domain $[-1.5, 1.5]\,\mathrm{m} \times [-1.5, 1.5]\,\mathrm{m}$, again horizontal and frictionless. An idealized circular dam of 0.35 m radius is placed in the center of the domain, and a static condition is initially assumed with water depth equal to 0.2 m inside the dam and 1 m outside. The sudden removal of the idealized dam induces a circular shock wave moving towards the center and an outward-propagating rarefaction wave. The shock progressively concentrates and "implodes" at the focusing point $(0, 0)$. It is proved in the literature that this collision process causes considerable numerical difficulties to 2D models, especially if a Cartesian mesh is adopted (e.g. Morel et al., 1996). In the revised version of the shock-focusing test case considered here, the implosion at the focusing point is exploited to generate a 2D transient mixed flow. With this aim, a 1.03 m high ceiling is introduced throughout the domain (see Fig. 3.9). Accordingly, the shock collision produces strong pressurization near the focusing point and gives origin to a circular filling bore which expands outwards.

The 2D simulation is restricted to the $[0, 1.5]\,\mathrm{m} \times [0, 1.5]\,\mathrm{m}$ sub-domain and is performed by setting the model parameters as follows: $\Delta x = \Delta y = 0.003\,\mathrm{m}, k_x = k_y = 0.01, Cr = 0.9$. Again, thanks to the cylindrical symmetry of the problem, a reference solution is obtained by solving Eq. (3.41) on the sub-domain $[0, 1.5]\,\mathrm{m}$ with a fine mesh of 3000 cells; the dimensionless slot width is assumed equal to 0.02 for the reason explained above. Figure 3.10 shows the comparison between 1D radial solution and diagonal ($y = x$) pressure head and velocity profiles at

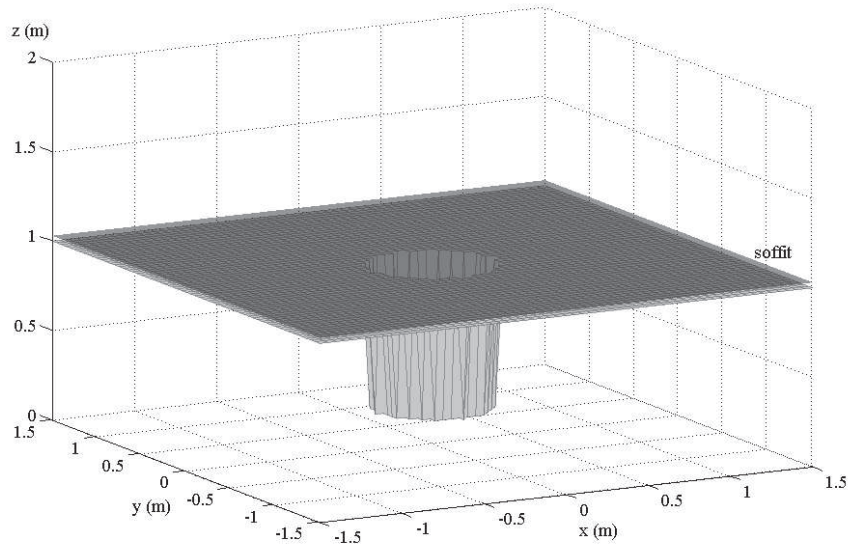

FIGURE 3.9 – Mixed shock-focusing test: sketch of the initial conditions

selected times ($t = 0.05, 0.10$, and $0.15\,\mathrm{s}$). The good agreement between reference 1D and 2D results confirms the effectiveness and robustness of the full 2D model, even for this extremely severe test case. In particular, the 2D model provides a fairly good description of the propagating phenomenon immediately after the collision, even though some discrepancies arise in the peak values (see the profiles at $t = 0.10\,\mathrm{s}$). Axial profiles are omitted in Fig. 3.10 because circular symmetry is very well preserved in this case too.

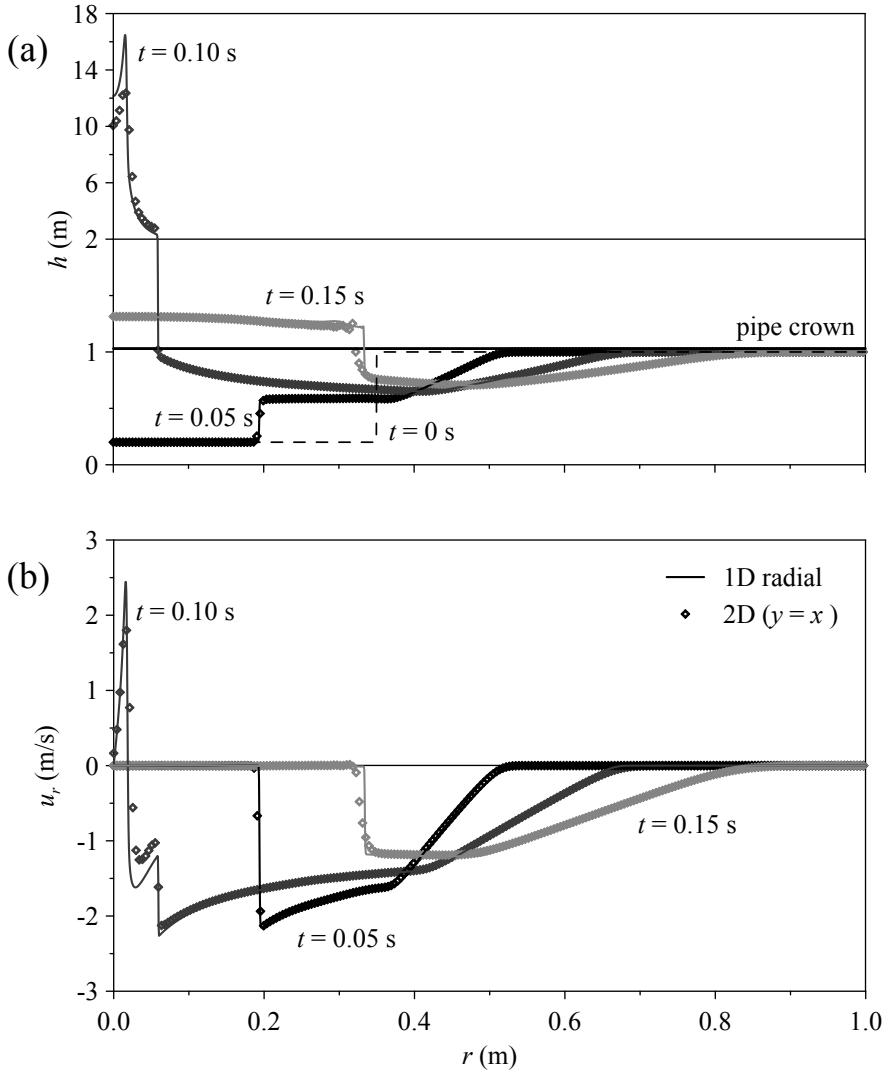

FIGURE 3.10 – Mixed shock-focusing test: comparison between reference 1D radial solution and 2D numerical profiles along $y = x$ at $t = 0.05, 0.10$, and $0.15\,\mathrm{s}$; (a) pressure head, (b) velocity. Only the radial sub-domain $[0, 1]\,\mathrm{m}$ is represented for clarity

3.4.3 Application to the case of flow under arch bridges

Steady-state conditions

A simple experimental test case is considered first. Experiments were performed in a 10 m long, 0.3 m wide horizontal laboratory flume. An arch bridge made of Plexiglas was positioned at $x = 4.23$ m from the upstream end. The bridge geometry is detailed in Fig. 3.11. A constant discharge equal to 0.015 m^3/s was allowed to flow in the flume until steady state conditions were achieved, while the free outfall occurred at the downstream end of the flume. This flow condition guaranteed that the bridge was subject to partial pressurization, i.e. only the lateral regions were surcharged, while the midstream region remained in free-surface conditions. Two ultrasonic transducers, positioned along the centerline of the flume at $x = 3.75$ m and $x = 6.55$ m, measured the water depths upstream and downstream of the bridge.

The computational domain is restricted to the region $[0, 6.55] \times [0, 0.3]$ m, and is discretized by means of a Cartesian mesh with cell size $\Delta x = 0.01$ m $\times \Delta y = 0.01$ m. The Courant number is set at 0.9, and the dimensionless widths k_x and k_y are set

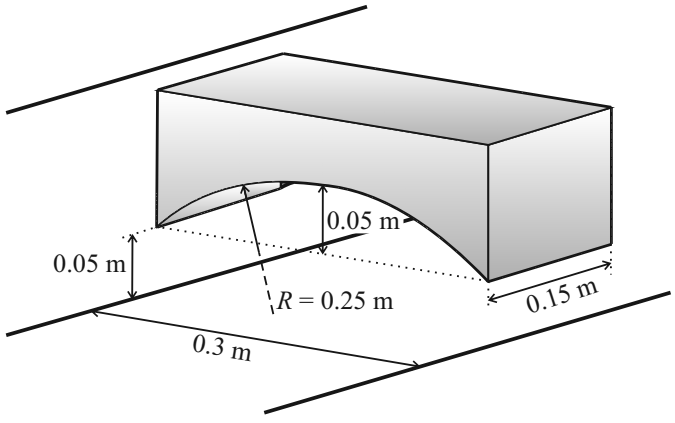

FIGURE 3.11 – Sketch of the experimental set-up

equal to 0.01 and 0.1, respectively. A constant discharge is imposed as upstream boundary condition, while the downstream boundary condition is a constant level equal to 0.085 m, as measured by the ultrasonic transducer at $x = 6.55$ m. Preliminary experiments indicated that Manning's roughness coefficient for the flume bottom could be reasonably assumed to be 0.01 $\mathrm{m}^{-1/3}\mathrm{s}$; on the other hand, the roughness coefficient assigned to the bridge low chord is artificially increased to take into account the local head losses induced by flow contraction and expansion when the bridge is pressurized. In this case, an "equivalent" roughness coefficient is computed over the wetted perimeter (e.g. Chow, 1959).

Figure 3.12 reports the longitudinal profile obtained from the simulations performed with the assumption of different values of Manning's coefficient for the soffit. It is to be noted that the backwater effect calculated with $n_{soffit} = 0.01\,\mathrm{m}^{-1/3}\mathrm{s}$ is not reproduced correctly, while increasing roughness up to four or five times guarantees a better agreement in this particular case.

Figure 3.13 shows the cross-sectional pressure head profiles at $x = 4.3$ m (middle of the bridge), which are not much influenced by the roughness coefficient value selected for the soffit. These profiles show a peculiar "U" shape, also associated with highly different values between the center line and the sides of the channel.

A field-scale test case

The transit of a dam-break bore under an arch bridge is modeled here, in order to assess the model's suitability for case studies with realistic size and for unsteady simulations.

This idealized test case concerns a straight horizontal channel of length 500 m with a 20 m wide rectangular cross-section (Fig. 3.14). An ideal thin vertical wall (simulating a retaining structure) identifies an upstream channel reach with length equal to 200 m. A 20 m wide arch bridge, located 50 m downstream of the

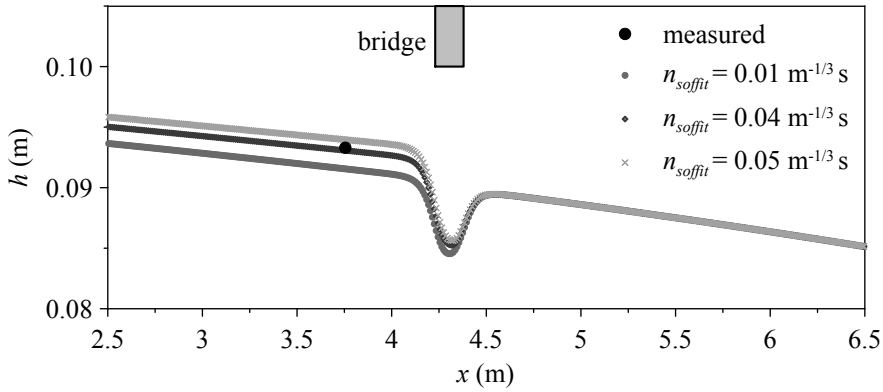

FIGURE 3.12 – Longitudinal profiles of water depth along the midstream line computed with three different values of the roughness coefficient for the soffit

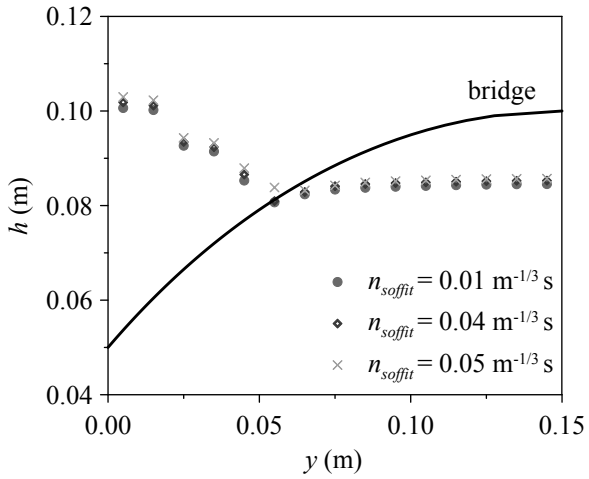

FIGURE 3.13 – Cross-sectional profiles of water depth in the middle section of the bridge, computed with three different values of the roughness coefficient for the soffit

wall, crosses over the canal perpendicularly to its center line. It is characterized by a parabolic lower profile described by the equation: $H = -0.04y^2 + 0.8y + 4$, where H indicates the elevation of the ceiling and y the transverse coordinate. The upstream channel reach initially acts as a reservoir containing still water with 15 m depth. Downstream, the bed is initially wet with a 1.5 m deep layer of still water. The sudden collapse of the wall induces the formation of a bore moving downstream towards the bridge. This test case represents a schematization of a real situation; nevertheless, despite the schematic geometry, it is useful to verify the model's reliability in this kind of engineering applications.

The computational domain is discretized by means of a Cartesian mesh with cell size $\Delta x = 1\,\text{m} \times \Delta y = 0.5\,\text{m}$. An orthogonal lattice of slots with dimensionless widths k_x and k_y both equal to 0.01 is ideally introduced on the lower surface of the bridge. Bed resistance is included by setting Manning's roughness coefficient at $0.03\,\text{m}^{-1/3}\text{s}$, whereas the local head losses are included by setting the soffit roughness coefficient at the augmented value $0.1\,\text{m}^{-1/3}\text{s}$. Finally, the Courant number is assumed equal to 0.9.

As an example of model results, Figs. 3.15 and 3.16 show computed cross-sectional (Fig. 3.15) and longitudinal (Figs. 3.16a and 3.16b) profiles for pressure head at $t = 10\,\text{s}$. At this time, the bore has already passed beyond the bridge

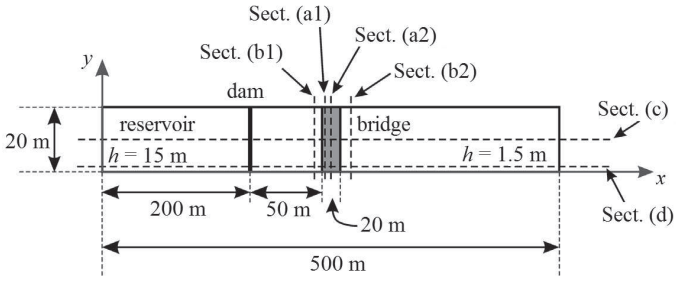

Sect.	Equation
(a1)	$x = 251.5$ m
(a2)	$x = 259.5$ m
(b1)	$x = 245.5$ m
(b2)	$x = 279.5$ m
(c)	$y = 9.75$ m
(d)	$y = 1.75$ m

FIGURE 3.14 – Plan view sketch of the idealized field-scale test case. Cross-sections are selected along computational cell centers

and keeps propagating downward. The opening under the bridge is partially pressurized (Fig. 3.16c). Predicted transverse pressure head profiles along the bridge show the peculiar "U" shape already observed in the steady state simulation. Moreover, the presence of the arch structure gives origin to 2D near-field effects: a wake and a backwater effect develop behind and in front of the bridge, respectively. This justifies the adoption of a 2D mixed flow model to describe the flow field near the bridge.

Although a reference solution is not available for comparison, the numerical results confirm the applicability of the 2D Preissmann slot model to field-scale problems characterized by the presence of topographic singularities (such as culverts or bridges) that could locally induce the pressurization of the flow.

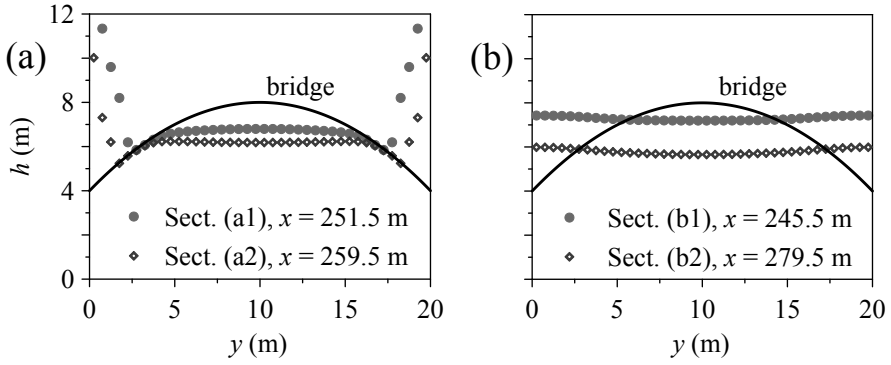

FIGURE 3.15 – Transit of a dam-break bore under an arch bridge: numerical results at $t = 10$ s. (a) Pressure head cross-sectional profiles (at $x = 251.5$ m and $x = 259.5$ m). (b) Water depth cross-sectional profiles just upstream ($x = 245.5$ m) and downstream ($x = 279.5$ m) of the bridge

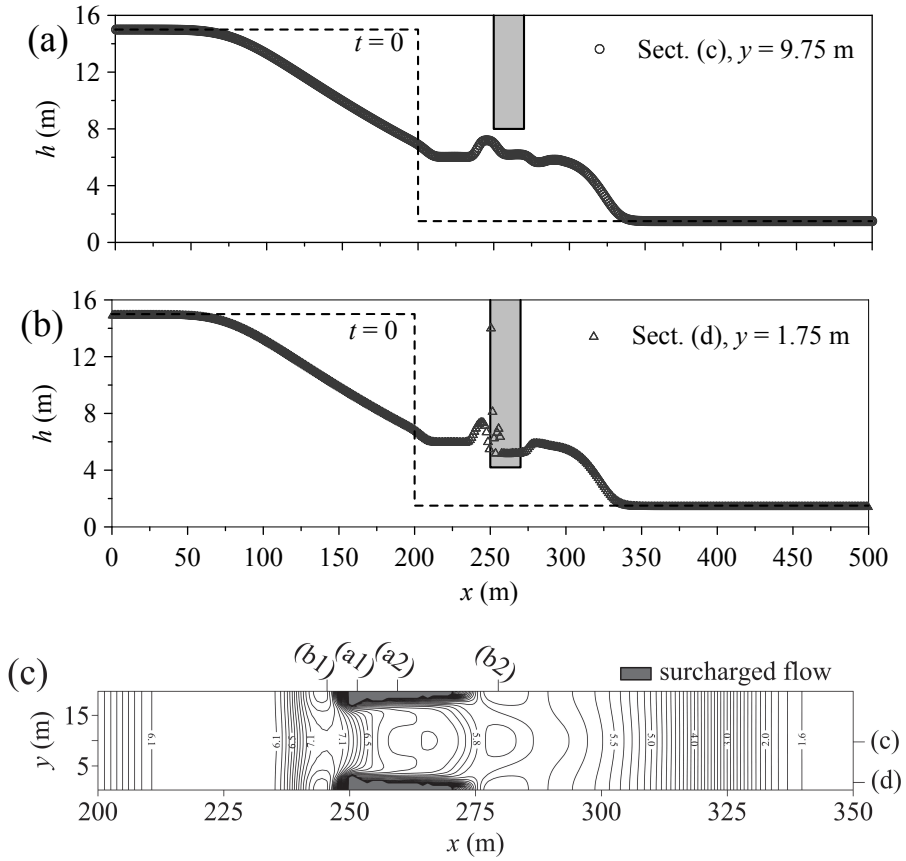

FIGURE 3.16 – Transit of a dam-break bore under an arch bridge: numerical results at $t = 10$ s. (a) Pressure head longitudinal profile at the channel center line ($y = 9.75$ m). (b) Pressure head longitudinal profile at the channel side ($y = 0.25$ m). (c) Water depth contour map around the bridge (contour levels in m) and prediction of surcharged and free-surface areas in the culverted reach

3.5 Concluding remarks

In this chapter the Preissmann slot concept has been extended and applied to 2D highly transient mixed flows. The resulting shallow water model, coupled with a Godunov-type finite volume numerical scheme, is capable of correctly reproducing both exact solutions of 1D discontinuous initial value problems and reference radial solutions of idealized cylindrically symmetric test cases, characterized by either abrupt or mild transitions between free surface and surcharged flows.

In the numerical simulation of 2D problems, since a preferential direction for the flow cannot be identified *a priori*, it seems reasonable to adopt the same value of the slot width to grid size ratio for both systems of orthogonal slots. In this work, a dimensionless ratio in the order of 1% guaranteed a good compromise between accuracy and computational stability, especially when strong pressurization waves occurred.

The simulation of the partial pressurization of an arch bridge, both at the laboratory scale and at field-scale, confirms the reliability and robustness of the model in practical applications involving topographical singularities, such as bridges or culverts, that could be partially or totally filled during flood events. The model, however, cannot be employed to simulate flooding events which give origin to bridge or culvert overtopping, due to the fact that, for example, the flow over a long culvert may even be totally separate from the culvert flow itself.

The value of Manning's coefficient can be artifically increased for the bridge low chord, so that the local head losses due to contraction and expansion when the bridge is pressurized can be taken into account in a simplified way.

Finally, the peculiar "U" shape that is observed in the numerical results when the arch bridge is pressurized should be further investigated experimentally, in order to verify its physical relevance.

Chapter 4

1D modelling of mixed flows through bridges and culverts with overtopping

4.1 Introduction

The presence of bridges, culverts, and similar hydraulic crossing structures in open channels may significantly affect the flood propagation, since these structures typically induce an obstruction to the flow. The lateral and vertical constrictions at bridge sites cause a backwater effect upstream (e.g. DEFRA, 2004), thus augmenting the flood hazard in the surrounding areas. Other notable problems related to the presence of bridges include scour and erosion around piers and abutments (e.g. FHWA, 2012), and hydrodynamic loading on its deck and piers (e.g. Malavasi and Guadagnini, 2003). During severe flood events, the water level may exceed the elevation of the deck low chord with consequent pressurization of

the bridge; the deck may even be overtopped for extreme events. Moreover, also a culvert may flow full in particular conditions, for example when the outflow is submerged (Chow, 1959). The occurrence of these flow conditions is defined as high flow, as opposed to low flow, which indicates that free-surface conditions occur below the structure (HEC, 2010). The characteristics of the flow through this kind of constrictions are in general very complicated due to the large number of hydraulic and geometrical variables involved. For this reason, a number of studies in the literature focused on this topic, especially on high flow conditions, from both an experimental and a numerical point of view (e.g. Martín-Vide and Prió, 2005; Picek et al., 2007; Kara et al., 2015). In particular, detailed experimental and numerical flow patterns around a submerged bridge with overtopping are reported in Kara et al. (2015). Other authors concentrated on the assessment of the backwater effect (sometimes referred to as *afflux*) in partially or totally submerged conditions, relying on the application of energy or momentum equations between two selected sections upstream and downstream of the bridge (e.g. Malavasi et al., 2006; HEC, 2010), or on empirical formulas derived from non-dimensional analysis and experimental data (e.g. Biery and Delleur, 1962; HR Wallingford, 1988; Seckin, 2004; Picek et al., 2007).

The integration of hydraulic structures which may be submerged or overtopped (such as bridges and culverts) in 1D numerical models is useful in water flood management applications, but is not straightforward. Actually, the effect of these structures is often modeled in a simplified way in the practice. As regards the effect of a bridge, Natale et al. (2004) separated the open channel in two reaches, one upstream and one downstream of the bridge, and linked them through suitable internal boundary conditions. Catella and Bechi (2006) imposed energy and continuity relations across the bridge in submerged conditions. Ratia et al. (2014) considered the head loss induced by the presence of a bridge as an additional source term in a 2D shallow water model. However, none of these

models consider the possibility of bridge overtopping. Moreover, the models previously mentioned cannot be applied for near-field simulations and cannot be extended to the case of flow through culverts, due to the fact that the bridge is modelled as a junction element, and thus its length is neglected. Among the commercial packages, HEC-RAS (HEC, 2010) is able to model high flow conditions with overtopping by exploiting either the energy equation method or the pressure and weir flow method. In particular, the pressure and weir flow method uses distinct hydraulic equations for pressurized flow (below the deck) and weir flow (above the deck). However, also within HEC-RAS, the bridge is modelled as a point element (although represented by four user-defined cross-sections) in which a special computational treatment is applied.

This chapter presents a 1D mixed flow model, based on shallow water approximation, which is able to effectively handle the effect of bridges and culverts on the flow field. The pressurized flow potentially occurring under these structures is modelled by means of the Preissmann slot approach. Internal boundary conditions (IBCs) are introduced as coupling mechanism (see Steinebach et al., 2004) to link free-surface flow upstream and downstream of the bridge, and potentially over the bridge, with pressurized flow under the bridge for high flow conditions. The use of these coupling conditions enables the numerical model to predict overtopping in an efficient way. Actually, IBCs are already widely used in the literature to simulate the flow changes induced by gates or other thin internal structures employed in open channel systems for operational and regulation purposes (e.g. Jafaar and Merkley, 2010; Morales-Hernández et al., 2013; Cozzolino et al., 2015).

Several simulations of laboratory and field-scale test cases are performed here to verify the effectiveness and the robustness of the numerical model proposed.

4.2 Topological discretization

The simple configuration of a rectangular channel with uniform width B, crossed by a bridge deck with no lateral contractions, is considered in this work. The bridge low and top chord elevations above the channel bed are D and Z, respectively, and its length is L (Fig. 4.1). A similar configuration was considered in Malavasi and Guadagnini (2003), Catella and Bechi (2006), and Picek et al. (2007).

The channel system including the bridge is modeled as composed by four distinct channel reaches linked at the two junctions (see Fig. 4.1): the first reach starts at the upstream end of the channel and ends immediately upstream of the bridge; the second represents the closed "conduit" below the bridge, while the third spans from immediately downstream of the bridge to the end of the channel; finally, the fourth reach acts as an open channel for modelling overtopping: it corresponds to the region above the deck, which obviously remains dry as long as the water surface elevation is below the top chord of the bridge. In short, in

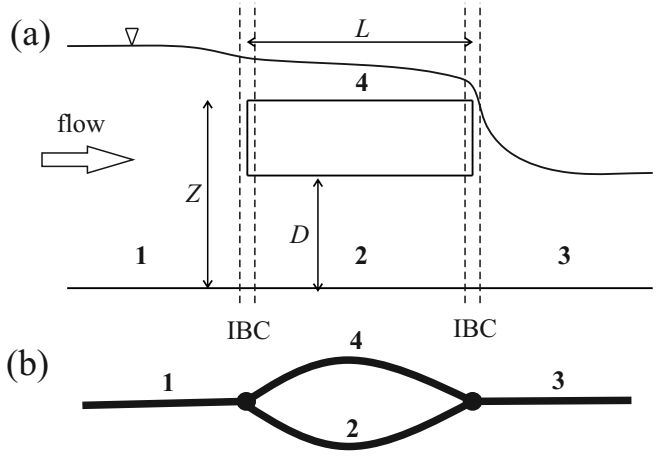

FIGURE 4.1 – Definition sketch of flow through a bridge with overtopping: (a) lateral view; (b) topological model representation using branches and junctions

the case of bridge overtopping, the pressurized flow under the bridge and the free-surface flow above it are modelled as two parallel flows (see Fig. 4.1). IBCs are implemented at junctions in order to link together the flow conditions in the four reaches. Based on this topological discretization, a purely 1D model can be reasonably used to simulate the effect of bridge and culvert singularities in high flow conditions. In this way, flows under and over the structure can be modeled in detail, with significant improvement in model predictability, especially in the presence of structures characterized by long extension in the channel flow direction (such as culverts). The idea of dividing the channel system into separate reaches and linking them through IBCs has also been used by Natale et al. (2004) in the presence of bridges, and by Jafaar and Merkley (2010) in the presence of gates, although in these works the entire structure is considered as collapsed into a single junction element where suitable IBCs are applied.

4.3 Internal boundary conditions

In the model proposed here, the IBC at the upstream end of the bridge/culvert links the last computational cell in reach 1 to the first cell in reach 2 and, only in the case of overtopping, to the first cell in reach 4 (see Fig. 4.2). The IBC at the downstream end of the bridge/culvert links the last cell in reaches 2 and 4 to the first cell in reach 3.

The flow along each branch is modelled through the finite volume scheme presented in Chapter 1, which adopts the Preissmann slot approach to handle pressurization. Conversely, the unknown variables in IBC cells are not updated via the usual finite volume time advancing formula (1.9), but are computed by a special procedure which introduces a suitable set of physical conditions (mass conservation, energy balances, and characteristic equations) linking the neighbouring states at the first and last cell of adjacent reaches. The IBC cells act

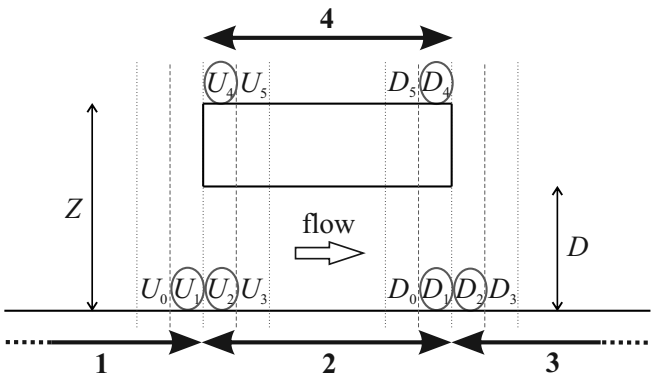

FIGURE 4.2 – Sketch of the topological discretization around the bridge with the indication of the computational cells involved in the IBCs (circled). Labels U and D refer to the upstream and downstream ends of the bridge

then as internal "ghost" cells located at the boundary of a physical domain. The flow states imposed at internal boundary cells via special updating formulas are employed in the subsequent time step to compute the intercell fluxes necessary to update the flow variables in the neighbouring cells inside each reach.

In the most general case, two flow variables in three cells need to be computed at each internal boundary, hence the system must include six equations. In the absence of overtopping, the system simplifies to only four equations, coupled with the trivial condition of zero depth and velocity in reach 4. The IBC system is non-linear and is solved iteratively in this work by using a modification of the Powell hybrid method implemented in the MINPACK package (Moré et al., 1980).

In the following, the internal boundary conditions at both upstream and downstream end of the bridge are explained in detail. The use of IBCs can be easily extended to the case of a flow through a culvert.

4.3.1 IBC at the upstream end of the bridge

The specification of IBCs at the upstream end of the bridge allows the computation of the flow variables $\mathbf{U}_{U1}$, $\mathbf{U}_{U2}$, and $\mathbf{U}_{U4}$ at cells U_1, U_2, and U_4 of Fig. 4.2 for each computational time step. Different cases can be distinguished as follows.

A If $\max(h_{U1}, h_{U2}) < D$, an undisturbed open-channel flow passes under the bridge. This case is trivial since no IBCs need to be applied. The numerical flux at the interface between cells U_1 and U_2 is computed with the selected flux evaluation method (the HLL solver in this work), and the flow states $\mathbf{U}_{U1}$ and $\mathbf{U}_{U2}$ are updated via the finite volume formula (1.9), as in the other cells of the computational domain. Cell U_4 remains dry.

B If $D < h_{U1} < Z$, no overtopping occurs: flow variables at cells U_1 and U_2 must be assessed by imposing suitable IBCs, while cell U_4 remains dry. Therefore, a set of four equations must be defined and solved to compute four unknown variables (h_{U1}, u_{U1}, h_{U2}, u_{U2}). In this case, two flow types can be distinguished depending on the downstream conditions:

B.1 sluice-gate flow, when the inlet is unsubmerged ($h_{U3} < D$);

B.2 pressure flow, when the inlet is submerged ($h_{U3} > D$) and the channel below the bridge flows full.

C If $h_{U1} > Z$, the bridge is overtopped and an open-channel flow occurs above the bridge deck. In this case, also cell U_4 is involved and the unknowns are six (h_{U1}, u_{U1}, h_{U2}, u_{U2}, h_{U4}, u_{U4}). Hence, the definition of a system of six equations is required.

Considering the most general case C, the steady flow continuity equation across the upstream end of the bridge is coupled with two steady flow energy equations connecting flow state $\mathbf{U}_{U1}$ to $\mathbf{U}_{U2}$, and flow state $\mathbf{U}_{U1}$ to $\mathbf{U}_{U4}$, respectively. To

close the system, the positive characteristic equation at the downstream boundary of reach 1 and the negative characteristic equations at the upstream boundary of reaches 2 and 4 are considered in the case of subcritical flow. The resulting non-linear system of equations (for a rectangular channel) reads:

$$u_{U1}^{n+1} A\left(h_{U1}^{n+1}\right) = u_{U2}^{n+1} A\left(h_{U2}^{n+1}\right) + u_{U4}^{n+1} A\left(h_{U4}^{n+1}\right) \tag{4.1a}$$

$$h_{U1}^{n+1} + \frac{\left(u_{U1}^{n+1}\right)^2}{2g} = h_{U2}^{n+1} + \frac{\left(u_{U2}^{n+1}\right)^2}{2g} + k\frac{\left(u_{U2}^{n+1}\right)^2}{2g} \tag{4.1b}$$

$$h_{U1}^{n+1} + \frac{\left(u_{U1}^{n+1}\right)^2}{2g} = Z + h_{U4}^{n+1} + \frac{\left(u_{U4}^{n+1}\right)^2}{2g} \tag{4.1c}$$

$$\left(u_{U1}^{n+1} + 2c_{U1}^{n+1}\right) - \left(u_{M1}^{n} + 2c_{M1}^{n}\right) = g\Delta t\left(S_0 - S_{f,M1}^{n}\right) \tag{4.1d}$$

$$\left(u_{U2}^{n+1} - 2c_{U2}^{n+1}\right) - \left(u_{M2}^{n} - 2c_{M2}^{n}\right) = g\Delta t\left(S_0 - S_{f,M2}^{n}\right) \tag{4.1e}$$

$$\left(u_{U4}^{n+1} - 2c_{U4}^{n+1}\right) - \left(u_{M4}^{n} - 2c_{M4}^{n}\right) = g\Delta t\left(S_0 - S_{f,M4}^{n}\right) \tag{4.1f}$$

in which k is a suitable loss coefficient. The variables labelled with the subscript M refer to an intermediate flow state at the previous time level t^n, which is evaluated through a numerical technique similar to the classical Hartree method (Cunge et al., 1980). For example, with reference to Eq. (4.1d), the flow variables in an intermediate point M_1, located between the centers of cells U_0 and U_1, at current time t^n must be derived. As shown in Fig. 4.3, the C^+ characteristic line projected backwards from the flow state $\mathbf{U}_{U1}^{n+1}$ intersects the time level t^n at the point M_1 (whose abscissa x_{M1} is unknown). The flow state at M_1 can then be predicted by linear interpolation of $\mathbf{U}_{U0}^{n}$ and $\mathbf{U}_{U1}^{n}$ states through the following

linear system which adopts a Euler first-order time discretization:

$$\begin{cases} x_{U1} - x_{M1} = \Delta t \, (u^n_{M1} + c^n_{M1}) \\ \dfrac{u^n_{U1} - u^n_{M1}}{u^n_{U1} - u^n_{U0}} = \dfrac{x_{U1} - x_{M1}}{\Delta x} \\ \dfrac{c^n_{U1} - c^n_{M1}}{c^n_{U1} - c^n_{U0}} = \dfrac{x_{U1} - x_{M1}}{\Delta x} \end{cases} \tag{4.2}$$

Similarly, M_2 state is interpolated from the known cell-centered states $\mathbf{U}^n_{U2}$ and $\mathbf{U}^n_{U3}$ (by projecting backward the C^- characteristic starting from the updated state $\mathbf{U}^{n+1}_{U2}$), and M_4 state is interpolated from $\mathbf{U}^n_{U4}$ and $\mathbf{U}^n_{U5}$ (moving backward along the C^- characteristic, starting from $\mathbf{U}^{n+1}_{U4}$). By adopting this procedure, the flow variables of the neighbouring cells U_0, U_3, and U_5 are also involved in the upstream IBC.

It is to be observed that characteristic equation (4.1e) concerning surcharged flow has the same formulation as the ones of free-surface flow (4.1d) and (4.1f), due to the fact that the Preissmann slot approach models a surcharged flow as an equivalent free-surface flow. Furthermore, Eq. (4.1c) assumes the conservation of total head between cells U_1 and U_4, in analogy with the case of a broad-crested weir flow. The only model parameter to calibrate is the head loss coefficient k in Eq. (4.1b), whose value depends in general on the entrance geometry and

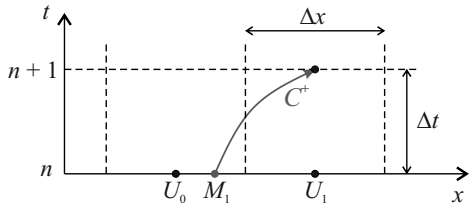

FIGURE 4.3 – Internal boundary condition at the upstream end of the bridge: sketch of the characteristics-based procedure for the estimation of the intermediate state M_1 at time level t^n

approach condition (Chow, 1959). Finally, in the special case of water at rest, the system has the trivial solution $h_{U1} = h_{U2} = h_{U4} + Z$ and $u_{U1} = u_{U2} = u_{U4} = 0$.

If the flow in reach 4 is supercritical ($Fr_{U4} > 1$), Eq. (4.1f) is no longer applicable since no C^- characteristic lines enter the reach 1 from U_4. In this case, it is assumed that $u_{U1}^{n+1} = u_{U4}^{n+1}$, and Eq. (4.1c) consequently simplifies to $h_{U1}^{n+1} = h_{U4}^{n+1} + Z$. Moreover, Eq. (4.1f) fails when reach 4 is initially dry (incipient overtopping): in this case, cell U_4 is updated via Eq. (1.9), by computing the numerical flux at the left intercell with the HLL solver for a Riemann problem with left state $(h_{U1} - Z, u_{U1})^n$ and right state ($h_{U4} = 0$, $u_{U4} = 0$). This special updating is applied until both cells U_4 and U_5 are wet.

Cases B can be considered as a simplification of case C when $h_{U4} = 0$ and $u_{U4} = 0$. In particular, for case B.2, only Eqs. (4.1a), (4.1b), (4.1d) and (4.1e) must be solved. Otherwise, for case B.1, if a free flow occurs, Eqs. (4.1a), (4.1b) and (4.1d) are coupled with the following relation:

$$h_{U2}^{n+1} = C_c D \tag{4.3}$$

where C_c represents the contraction coefficient, usually assumed depending on the ratio h_{U1}/D (Chow, 1959). In this case, negligible head losses are assumed at the inlet ($k = 0$). However, if cell U_3 is in subcritical free-surface conditions, Eq. (4.3) is substituted by the negative characteristic equation (equal to Eq. (4.1e)).

4.3.2 IBC at the downstream end of the bridge

As regards the IBC at the downstream end of the bridge, the flow variables at cells D_1, D_2, and D_4 of Fig. 4.2 must be assigned. Different situations can be distinguished also in this case.

A If $\max(h_{D1}, h_{D2}) < D$, the bridge outlet is unsubmerged and IBCs are not

applied.

B If $h_{D1} > D$, the bridge outlet is submerged and a pressurized flow occurs under the bridge. Four conditions are required in order to the specify the flow states $\mathbf{U}_{D1}^n$ and $\mathbf{U}_{D2}^n$ at cells D_1 and D_2.

C If $h_{D4} > 0$, the deck is overtopped and six equations are required to specify flow variables at three IBC cells D_1, D_2, and D_4. However, two possibilities must be considered:

C.1 unsubmerged flow (or free-flow), which occurs when the flow above the deck is not influenced by downstream conditions;

C.2 submerged flow, which occurs if the flow depth downstream exceeds a certain threshold, influencing the subcritical free-surface flow above the bridge.

For case B, flow states at cells D_1 and D_2 are linked by both the steady state continuity and energy equations. In the energy equation, it is advisable to introduce a minor head loss like the one due to a sudden expansion. In order to close the system, the positive characteristic equation coming from the interior of reach 2 and the negative characteristic equation coming from the interior of reach 3 can be added:

$$u_{D1}^{n+1} A\left(h_{D1}^{n+1}\right) = u_{D2}^{n+1} A\left(h_{D2}^{n+1}\right) \tag{4.4a}$$

$$h_{D1}^{n+1} + \frac{\left(u_{D1}^{n+1}\right)^2}{2g} = h_{D2}^{n+1} + \frac{\left(u_{D2}^{n+1}\right)^2}{2g} + \frac{\left(u_{D1}^{n+1} - u_{D2}^{n+1}\right)^2}{2g} \tag{4.4b}$$

$$\left(u_{D2}^{n+1} - 2c_{D2}^{n+1}\right) - \left(u_{M2}^{n} - 2c_{M2}^{n}\right) = g\Delta t\left(S_0 - S_{f,M2}^{n}\right) \tag{4.4c}$$

$$\left(u_{D1}^{n+1} + 2c_{D1}^{n+1}\right) - \left(u_{M1}^{n} + 2c_{M1}^{n}\right) = g\Delta t\left(S_0 - S_{f,M1}^{n}\right) \tag{4.4d}$$

As stated in Section 4.3.1, subscript M refers to intermediate flow state interpolated through first-order time discretization from two known cell-centered states at the current time level. In the case of overtopping (case C), the continuity equation (4.4a) becomes:

$$u_{D1}^{n+1} A\left(h_{D1}^{n+1}\right) + u_{D4}^{n+1} A\left(h_{D4}^{n+1}\right) = u_{D2}^{n+1} A\left(h_{D2}^{n+1}\right) \tag{4.5}$$

and the positive characteristic equation at the downstream boundary of reach 4 is added to the system:

$$\left(u_{D4}^{n+1} + 2c_{D4}^{n+1}\right) - \left(u_{M4}^{n} + 2c_{M4}^{n}\right) = g\Delta t\left(S_0 - S_{f,M4}^{n}\right) \tag{4.6}$$

As for the sixth equation required, for unsubmerged flow above the bridge (case C.1), two sub-cases may be distinguished as follows.

- If $Fr_{D5} > 1$, then supercritical flow occurs above the bridge, and the negative characteristic equation at the end of reach 4 is used:

$$\left(u_{D4}^{n+1} - 2c_{D4}^{n+1}\right) - \left(u_{M4b}^{n} - 2c_{M4b}^{n}\right) = g\Delta t\left(S_0 - S_{f,M4b}^{n}\right) \tag{4.7}$$

- else, cell D_4 identifies a control section with critical depth:

$$h_{D4}^{n+1} = \frac{\left(u_{D4}^{n+1}\right)^2}{g} \tag{4.8}$$

In both cases, Eq. (4.6) coupled with Eq. (4.7) or (4.8) is first solved explicitly to compute the flow variables in cell D_4 (h_{D4} and u_{D4}), and then Eqs. (4.4b)–(4.4d) and (4.5) are solved together.

Finally, in the case of overtopping with submerged flow above the bridge (case C.2), the sixth equation of the IBC system is provided by the energy balance

between cells D_4 and D_2:

$$Z + h_{D4}^{n+1} + \frac{\left(u_{D4}^{n+1}\right)^2}{2g} = h_{D2}^{n+1} + \frac{\left(u_{D2}^{n+1}\right)^2}{2g} + \frac{\left(u_{D4}^{n+1} - u_{D2}^{n+1}\right)^2}{2g} \tag{4.9}$$

No model parameters appear in the equations. The water at rest condition can be easily obtained for cases B and C.2.

From the previous discussion concerning the formulation of the IBCs to be imposed at both the upstream and downstream end of the bridge, it can be deduced that the resulting numerical scheme is not rigorously conservative at IBC cells. Indeed, considering the upstream IBC specified by Eq. (4.1), the intercell flux past the right boundary of cell U_1 does not equal exactly the sum of the fluxes past the two left boundaries of the adjacent cells U_2 and U_4. Moreover, the use of the energy approach in order to introduce physical equations between the flow variables at the IBC cells does not ensure that the momentum conservation principle is locally satisfied. Finally, it is expected that the adoption of steady state flow equations in IBCs introduces errors which can be significant for rapidly varied unsteady flows.

4.4 Numerical tests

4.4.1 Steady state test cases from Picek et al. (2007)

The model validation is first performed on the basis of a comparison with some of the experimental data presented in Picek et al. (2007). The profile measurements were provided by Prof. Picek.

The authors carried out a set of experiments in a laboratory flume with horizontal bottom and rectangular cross-section with width equal to 0.75 m. The deck low chord was positioned at an elevation D above the bottom, and its

thickness s was 0.075 m; hence, according to the notation adopted here, $Z = D + s$. The bridge was 0.3 m long and was placed 1.1 m from the downstream end of the channel. Different steady state subcritical conditions, all characterized by pressurized flow through the bridge, were realized by controlling the water level h_d at the downstream end of the flume. In this way, different flow conditions could be achieved above the deck:

- no overtopping (tests P1);
- overtopping with unsubmerged free-surface flow (tests P2);
- overtopping with submerged free-surface flow (tests P3).

The constant flow discharge and the longitudinal water surface profile along the channel centerline were measured for each experimental test. Table 4.1 reports the details of the test conditions here considered.

The computational domain was discretized by means of cells of size $\Delta x = 0.02$ m. Manning's coefficient was assumed equal to 0.01 $\mathrm{m}^{-1/3}$s, the Courant number was set at 0.9, and the Preissmann slot width was set at $0.01B$. Finally, the head loss coefficient k was assumed equal to 0.1.

TABLE 4.1 – Test conditions for the Picek et al. (2007) test cases

Test	$Q(\mathrm{m}^3/\mathrm{s})$	$D(\mathrm{m})$	$Z(\mathrm{m})$	$h_d(\mathrm{m})$	Type of overtopping flow
P1a				0.182	No overtopping
P2a	0.111	0.150	0.225	0.248	Overtopping – unsubmerged flow
P3a				0.334	Overtopping – submerged flow
P1b				0.243	No overtopping
P2b	0.155	0.225	0.300	0.325	Overtopping – unsubmerged flow
P3b				0.409	Overtopping – submerged flow
P1c				0.323	No overtopping
P2c	0.184	0.300	0.375	0.405	Overtopping – unsubmerged flow
P3c				0.522	Overtopping – submerged flow

In the numerical modelling of subcritical flows, the backwater effect induced by obstacles is one of the most important practical features which should be predicted. Figure 4.4 compares the experimental and numerical backwater levels (normalized to the measured tailwater depth) for the test cases detailed in Table 4.1. The results show that the numerical model proposed is able to reproduce the backwater effect of the bridge with good accuracy.

These test cases are also simulated with HEC-RAS (HEC, 2010). The distance between cross-sections is 0.2 m, and the bridge is inserted as a separate structure, whose presence is taken into account in the computations with the pressure and weir flow method. According to this approach, the full flowing orifice equation is used to compute the pressure flow discharge:

$$Q_{down} = C_Q DB\sqrt{2g\left(h_u + \frac{u_u^2}{2g} - h_d\right)} \tag{4.10}$$

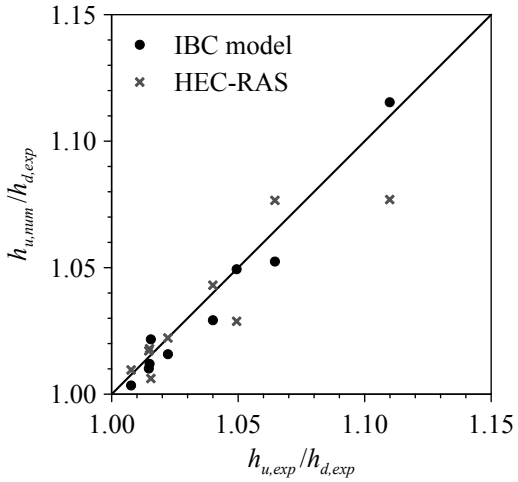

FIGURE 4.4 – Comparison between experimental and numerical dimensionless backwater levels for the laboratory test cases reported in Table 4.1: results from the proposed model and from HEC-RAS

while the standard weir flow equation is employed to compute the flow over the bridge:

$$Q_{up} = C_W B \left(h_u + \frac{u_u^2}{2g} - Z \right)^{1.5} \tag{4.11}$$

Two discharge coefficients need to be defined. Typical values of the coefficient of discharge C_Q in Eq. (4.10) are in the range $0.7 - 0.9$, usually 0.8 (HEC, 2010). However, these values were calibrated for a trapezoidal channel with side contraction in the bridge. Picek et al. (2007) showed that, for their deck geometry, the coefficient of discharge is in the range $0.8 - 0.95$ for partially submerged deck, and between 1.0 and 1.1 when the deck is entirely submerged (overtopped). In Eq. (4.10), C_Q is then assumed equal to 1.04. As regards Eq. (4.11), the coefficient C_W is assumed in the range of typical values for broad-crested weirs ($1.38 - 1.71\,\mathrm{m}^{1/2}/\mathrm{s}$, HEC, 2010), and in particular equal to the default value $1.4\,\mathrm{m}^{1/2}/\mathrm{s}$. The normalized backwater levels predicted by HEC-RAS are also reported in Fig. 4.4, which shows that the results provided by the two models are characterized by a comparable accuracy, even if the IBC model performs slightly better. In fact, the mean absolute deviation between numerical and experimental (normalized) backwater levels is equal to 0.0058 for the IBC model, and to 0.0095 for HEC-RAS.

The IBC model automatically splits the approach discharge Q into the discharge Q_{down} of the pressure flow through the bridge opening and the overtopping discharge Q_{up}. The three P2-labelled tests (characterized by an unsubmerged overtopping flow) are considered to analyze the model's suitability for predicting the discharge splitting. Due to the fact that Q_{up} and Q_{down} were not measured experimentally, reference values are estimated here using the method proposed by Malavasi et al. (2006), based on an energy equation approach coupled with the critical state assumption at the downstream end of the bridge. In the hydraulic computations, the same head losses as in the proposed model are considered for

consistency. Table 4.2 reports the computed values of Q_{up} and Q_{down} (normalized to the total discharge) provided by the IBC model, by the method of Malavasi et al. (2006), and by HEC-RAS simulations. The results obtained by using the three methods show differences within 2% of the total discharge.

Predicted water surface profiles along the channel centerline are analyzed for the test cases of type "a" (Tests P1a, P2a, and P3a), characterized by fixed total discharge ($Q = 0.111\ \mathrm{m}^3/\mathrm{s}$). Figure 4.5a shows the measured longitudinal water surface profiles, along with the results of the 1D numerical simulations. The profiles predicted by HEC-RAS are also reported. As expected, the characteristic near-field features of the flow in vicinity of the bridge are not reproduced accurately by 1D modelling, especially the local water surface upsurge at the upstream face of the deck and the flow expansion profile downstream of the bridge. Indeed, the flow through a bridge is in general rapidly varied in space, with significant accelerations in the vertical direction, which cannot be modeled adopting the 1D approximation. However, the backwater profile which develops upstream of the bridge is well caught. The local upswell at the entrance of the bridge opening can be reasonably related to the velocity head of the approach flow, and depends on the degree of submergence (Picek et al., 2007). For test P1a, the velocity head calculated at the computational cell located just upstream of the bridge opening provides a satisfactory estimate of the experimental upswell with a relative error

TABLE 4.2 – Comparison of the discharge splitting prediction performed by the IBC model, by the energy-balance method by Malavasi et al. (2006), and by HEC-RAS for the P2-labelled tests

Test	IBC model		Energy balance method		HEC-RAS	
	Q_{down}/Q	Q_{up}/Q	Q_{down}/Q	Q_{up}/Q	Q_{down}/Q	Q_{up}/Q
P2a	0.866	0.134	0.883	0.117	0.867	0.133
P2b	0.900	0.100	0.906	0.094	0.905	0.095
P2c	0.914	0.086	0.917	0.083	0.922	0.078

of roughly 2% of the total head. As regards the profile over the bridge deck, the numerical model predicts the expected decrease in the water surface elevation, but some discrepancies appear in comparison with the experimental profiles. In particular, for test P3a the 1D numerical results do not match the complex wavy profile over the deck, closely resembling an undular hydraulic jump.

The experimental pressure head profiles under the bridge are not available, hence no direct comparison can be performed. In order to obtain further data for comparison, the same tests are simulated by using FLUENT (FLUENT, 2011), a widespread commercial software for computational fluid dynamics based on the finite volume discretization. Actually, a 2D simulation in the x-z vertical plane is sufficient, due to the symmetry of the flow, if the side walls friction is neglected. The Volume of Fluid (VOF) approach (Hirt and Nichols, 1981) is adopted to predict the interface between water and air. According to this

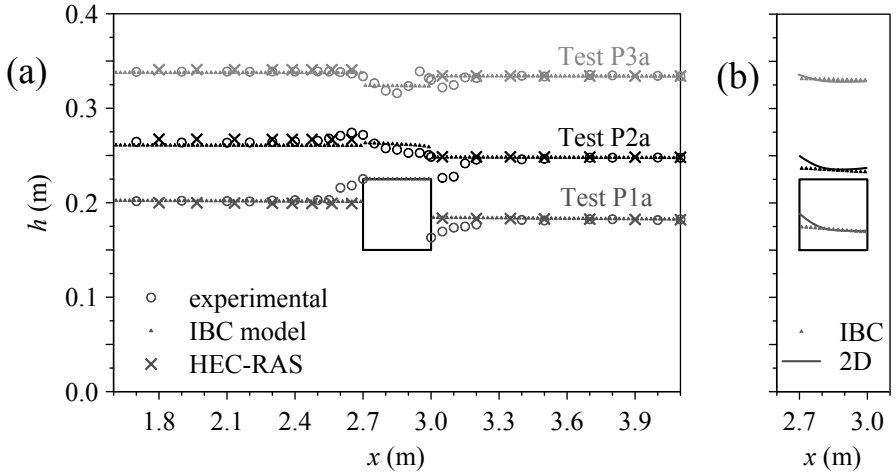

FIGURE 4.5 – (a) Experimental and numerical (1D and 2D-vertical) longitudinal water surface profiles for the three test cases P1a, P2a, and P3a. (b) Detail of the hydraulic grade lines of the pressurized flow through the bridge opening predicted by the 1D and 2D-vertical numerical models

method, the fluid is modelled as an immiscible two-phase system (water–air): a new variable is introduced to represent the volume fraction of water in each computational cell, and is used as a weighting factor to obtain volume-averaged fluid properties in each computational cell. The transport equation for the volume fraction must be added to the system of governing equations. Moreover, the realizable κ-ε model is selected for modelling turbulence. The flow field around the bridge is discretized through quadrilateral elements whose average size is 0.005 m, with some inflation near the bottom and around the deck. A mass flow inlet is assigned as upstream boundary condition, while a constant water depth is imposed downstream; moreover, a pressure outlet (with atmospheric pressure) is selected as boundary condition at the upper limit of the computational domain, and the no-slip wall condition with roughness height equal to 0.1 mm is specified on the channel bottom and around the deck. The simulations were run until steady state conditions were achieved. Static pressure at the channel bottom is used to derive the hydraulic grade line, by assuming a parallel flow with hydrostatic-pressure distribution. However, this assumption does not hold near the entrance of the bridge, given the substantial curvature of the streamlines (see Fig. 4.6).

Figure 4.6 shows that the 2D model accurately reproduces the flow features in the vicinity of the bridge on the vertical plane. Moreover, Fig. 4.5b shows a good agreement between 1D and 2D numerical results concerning the pressure head profile of the pressurized flow below the bridge, especially in the region from the middle to the downstream end of the bridge. In addition, the velocity maps in Fig. 4.6 show that the fluid accelerates passing through the bridge and that stagnation zones appear near the front and the rear faces of the deck (see for comparison the experimental data by Malavasi and Blois, 2007). It can be noticed that the 2D model wrongly predicts overtopping with very shallow water depths above the deck for test P1a (see Fig. 4.6a). In this case, the measured backwater

level is actually very close to the bridge high-chord elevation.

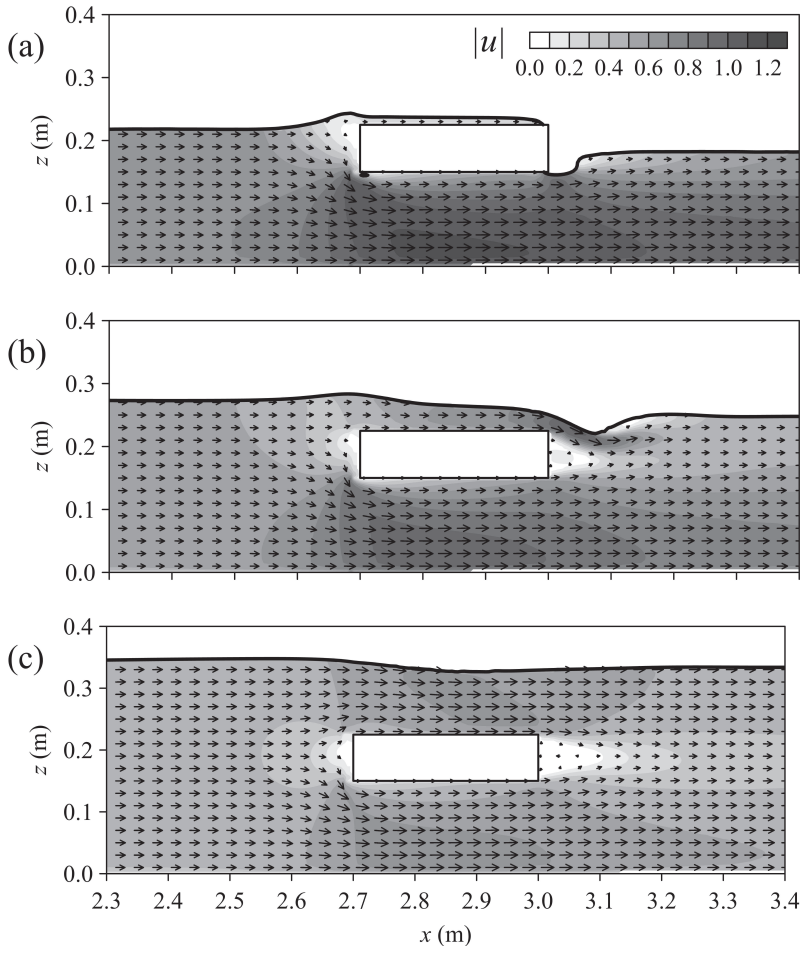

FIGURE 4.6 – Numerical velocity field on a vertical plane from 2D VOF simulations for tests P1a (a), P2a (b), and P3a (c). The thick black line indicates the water surface (estimated as the iso-surface with volume fraction equal to 0.5). The spatial frequency of velocity vectors is reduced for clarity

4.4.2 Steady and unsteady flow through a culvert with submerged outlet

The numerical model is applied here to the idealized case of the steady flow through a box tunnel placed in the middle reach of a 1000 m long and 3 m wide rectangular channel with 0.1% bottom slope. The culvert is 100 m long, with a 2 m high soffit. The flow rate is equal to 15 m^3/s. The downstream tailwater is assumed sufficiently high to submerge the outlet and induce a pressurized flow into the culvert.

The channel is discretized by means of $N = 100$ cells ($\Delta x = 10$ m), and Manning's coefficient is assumed equal to 0.015 $m^{-1/3}s$. A constant water depth of 2.5 m is imposed as the downstream boundary condition. Moreover, the Courant number is set at 0.9, while the non-dimensional slot width T_s/B is set at 0.01.

The same test case is also simulated with HEC-RAS. The culvert is inserted within the channel with the "lid-option" to represent the top of the pipe (HEC, 2010). For this configuration, the distance between the cross-sections is assumed equal to 50 m, except for the inlet and outlet of the culvert, where two cross-sections very close to each other (one with the lid and one without) are inserted to describe the abrupt geometry change in a more accurate way. At the culvert inlet, the contraction coefficient is set at 0.3 (instead of the default value 0.1) to increase the local head loss.

Figure 4.7 shows the hydraulic grade line (HGL) and the energy line (EL) along the channel obtained from the IBC model after the achievement of steady state conditions. Results from the steady flow analysis performed with HEC-RAS are also reported. The two models give very similar profiles, even if HEC-RAS predicts a slightly lower friction slope than the IBC model in the culvert.

The model is also tested for unsteady flow. Starting from a 1.2 m normal flow depth and a 5.79 m^3/s discharge, an incoming inflow hydrograph with 30 min

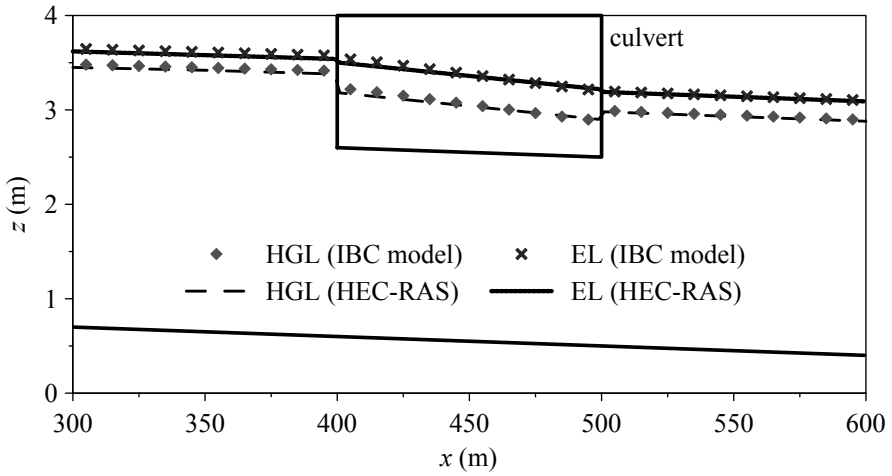

FIGURE 4.7 – Hydraulic grade line and energy line for a steady flow through a culvert with submerged outlet: comparison of the results predicted by the IBC model and by HEC-RAS

duration and 15 m^3/s peak discharge after 15 min is admitted from the upstream end of the channel. Downstream, a transmissive boundary condition is imposed. The same test is simulated with HEC-RAS, and the Preissmann slot option is activated.

Figure 4.8a shows the HGL along the channel at selected times. The culvert is pressurized starting from $t = 25$ min, and the maximum backwater is observed after approximately 35 min. During the falling limb of the hydrograph, the pressure head in the culvert decreases, until free-surface conditions are restored (after approximately 49 min). Figure 4.8 also reports the hydrograph of discharge (Fig. 4.8b) and of water depth (Fig. 4.8c) at selected sections. The two models predict very similar results, even if some discrepancies can be observed. In particular, the IBC model overestimates the water depth at the downstream end of the channel after the peak discharge.

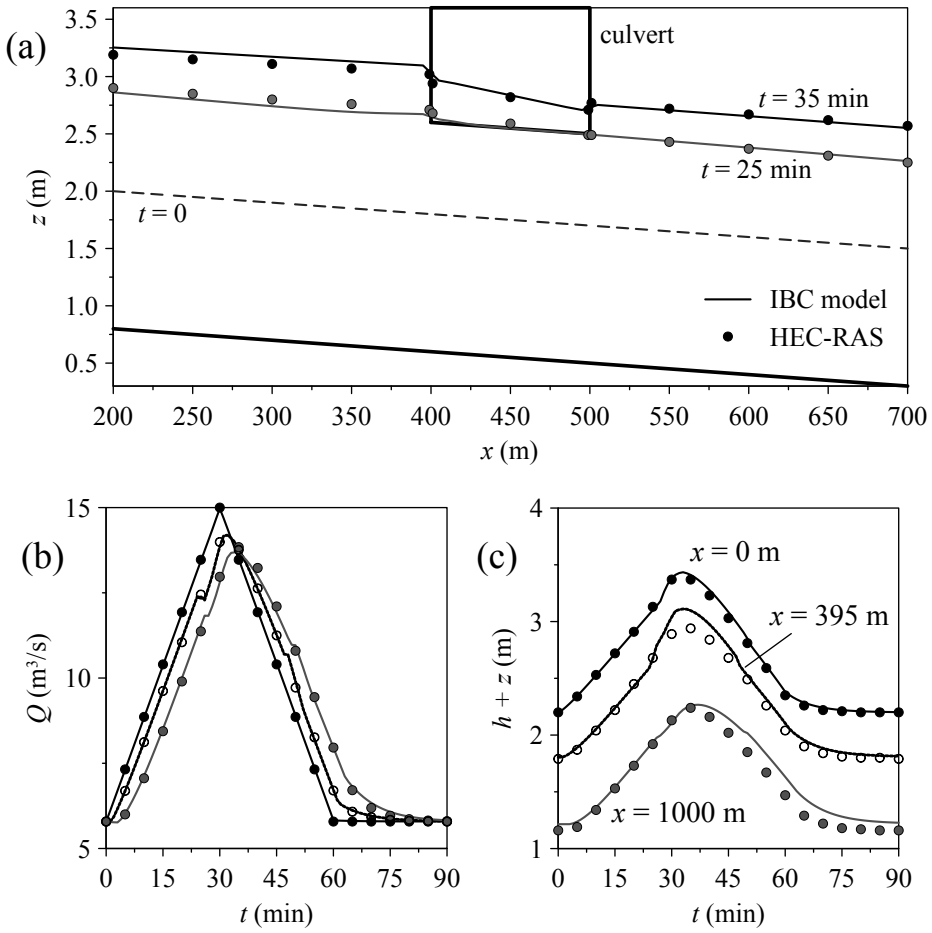

FIGURE 4.8 – Results of the IBC model (lines) and HEC-RAS (dots) for the simulation of the unsteady flow in a culvert undergoing pressurization: HGL at selected times (a), and hydrographs of discharge (b) and water level (c) at the channel ends and at the cross-section immediately upstream of the culvert inlet

4.4.3 Wave transmission through a submerged tunnel

One of the experimental test cases performed by Wiggert (1972) is used here in order to validate the IBC model in unsteady flow conditions. In particular, the transmission of a surge wave in a tunnel is examined. The tunnel remains in pressurized conditions during the whole experiment. Unfortunately, no experimental measurements concerning overtopping in unsteady flow conditions are available in the literature.

The experimental set-up consisted of a 30 m long, 0.51 m wide flume with horizontal bottom. In the middle reach of the flume, a roof was inserted in order to create a 10 m long and 0.15 m high culvert. The channel contained water at rest, whose elevation was approximately equal to 0.176 m. Hence, the tunnel was pressurized from the beginning. By manoeuvring a gate placed upstream, a surge wave was allowed into the channel, while the downstream level was controlled by a weir. Measurements of water depth and pressure head were taken at selected locations, whose positions are reported in Fig. 4.9.

The numerical simulation is performed by assuming Manning's roughness coefficient equal to 0.012 $\mathrm{m}^{-1/3}\mathrm{s}$, as indicated in the original paper. The domain is discretized by elements of size $\Delta x = 0.05$ m, and the Courant number is set at 0.9, while the non-dimensional slot width is assumed equal to 0.01. The lack of details about the gate manoeuvre and the weir height made the choice of boundary

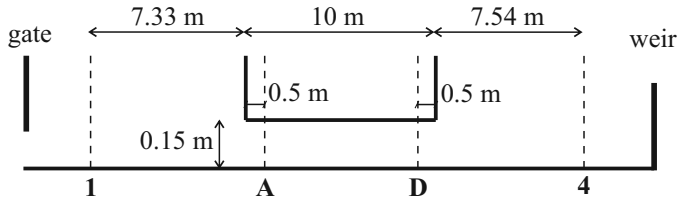

FIGURE 4.9 – Sketch of the experimental set-up for the test case reported in Wiggert (1972)

conditions difficult. The domain is restricted to the region of the channel between sections 1 and 4 (see Fig. 4.9), and water depth recordings at the same locations (digitalized from the original paper) are imposed as boundary conditions. These data are reported in Fig. 4.10.

Results of the numerical simulations are shown in Fig. 4.11 along with experimental data. Some discrepancies can be observed between the numerical and experimental results; these differences can be attributable to the uncertainty in the boundary conditions and in the digitalization of measurements. However, the general trend of the phenomenon seems reasonably well caught by the numerical model.

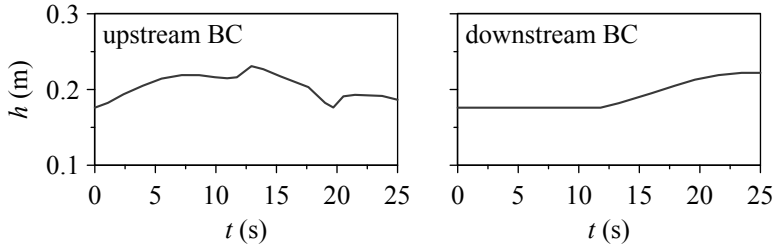

FIGURE 4.10 – Boundary conditions for the test case reported in Wiggert (1972)

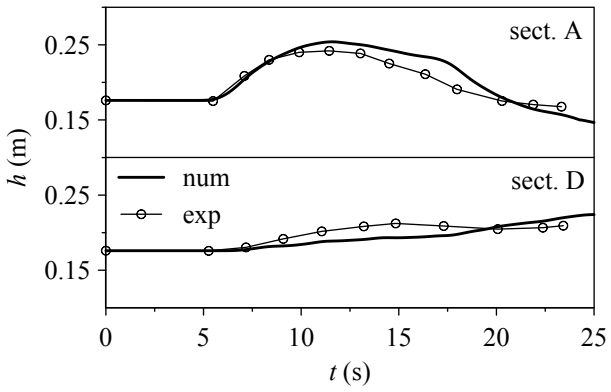

FIGURE 4.11 – Numerical and experimental data for the test case reported in Wiggert (1972) at sections labelled A and D

4.4.4 Unsteady flow through a submerged bridge with overtopping

In the present subsection, the numerical model is applied to the hypothetical case study of the transit of a flood wave in a rectangular channel crossed by a simple beam bridge. The channel is 1000 m long and 30 m wide, with 0.1% bottom slope. The bridge deck is 10 m long, and is positioned between $x = 490$ m and $x = 500$ m. It has the low chord at an elevation of 3 m above the channel bed, and thickness equal to 1.5 m. Manning's coefficient is assumed equal to 0.03 $\mathrm{m}^{-1/3}\mathrm{s}$. Initially, the flow is uniform with 92.4 m^3/s discharge and normal water depth equal to 2 m. An incoming flow hydrograph, characterized by a triangular shape with duration of 9 h and peak discharge equal to 450 m^3/s after 3 h, is imposed at the upstream end of the channel. This configuration gives origin to bridge overtopping. Downstream, a transmissive boundary condition is assumed.

The computational domain is discretized by means of $N = 1000$ cells ($\Delta x = 1$ m). The numerical simulation is performed by setting the Courant number at 0.9 and the non-dimensional slot width T_s/B at 0.01.

This test case is also simulated with HEC-RAS, by imposing the pressure and weir flow method for taking the bridge into account. The coefficient of discharge for weir flow is set at 1.5 $\mathrm{m}^{1/2}/\mathrm{s}$, while the coefficient of discharge for pressure flow is 0.85.

Figure 4.12a shows the longitudinal profiles of water surface elevation predicted by the two models at selected times, while Fig. 4.12b reports the discharge hydrograph at the bridge site, considering Q_{down} and Q_{up} separately. Moreover, Fig. 4.12c reports the time series of water surface elevation at the cross-section located at $x = 487$ m, immediately upstream of the bridge. Results show that the transit of the flood wave causes the bridge pressurization starting from a few minutes before $t = 1$ h until a few minutes before $t = 8$ h. Bridge overtopping

occurs between $t = 1.6$ h and $t = 6$ h, with a maximum at approximately $t = 3$ h. The two models provide similar results, except for slight differences in the discharge splitting at the bridge site (see Fig. 4.12b).

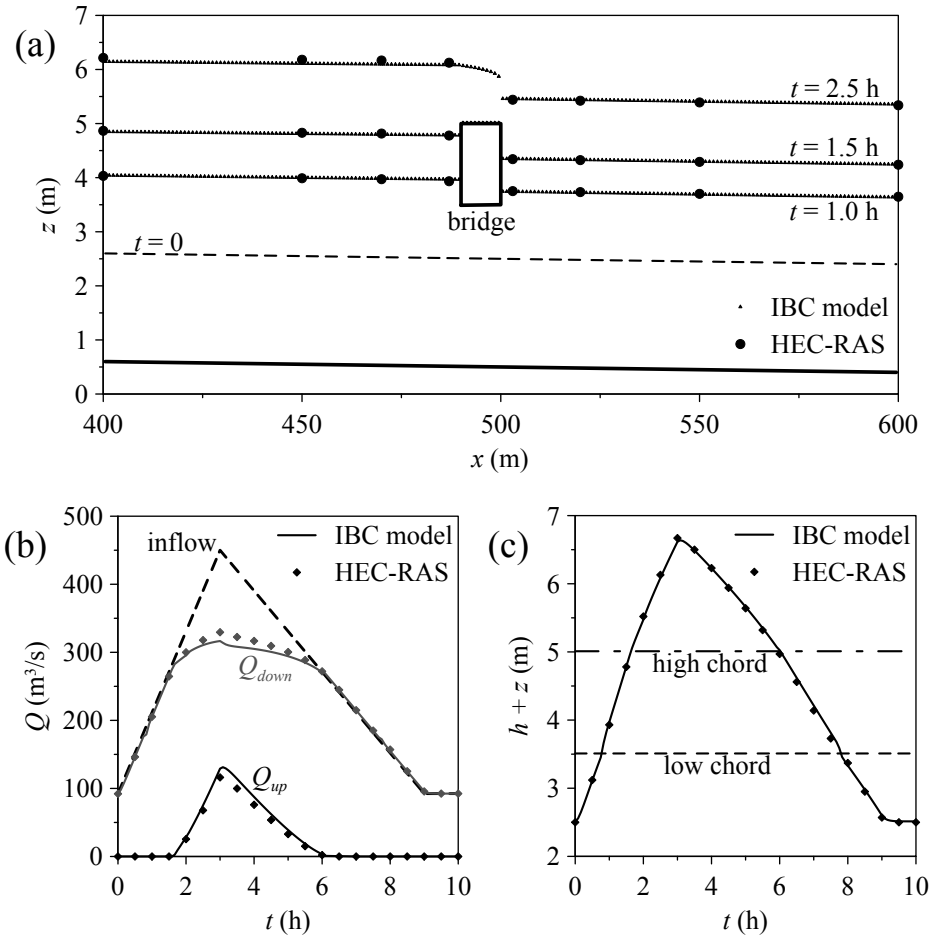

FIGURE 4.12 – Results of the IBC model and HEC-RAS for the case of unsteady flow through a bridge with overtopping: (a) longitudinal water surface elevation profiles at selected times, (b) discharge hydrographs at the bridge site, and (c) water surface elevation time series at $x = 487$ m

4.5 Discussion and concluding remarks

The method proposed herein for coupling a 1D mixed flow numerical scheme with a suitable formulation of IBCs yielded satisfactory results in the simulation of several test cases concerning both steady and unsteady flows through bridges and culverts. The model was validated by comparison with experimental data, and also with the results of numerical simulations performed with the widespread software HEC-RAS, which is often employed as a standard for 1D open channel flow modelling.

The model was found to be robust, even for the simulation of rapidly varied unsteady flows, such as the transit of a flood wave through a bridge with overtopping. The only source of instability was sometimes observed to be the iterative solution of the systems of equations for IBCs, especially when the water depth was very shallow above the deck. In order to overcome this problem, different methods for solving the non-linear system should be explored.

The use of IBCs is suitable to link in a simple and effective way the various reaches introduced in the topological discretization. The method can then be a useful tool for 1D modelling of high flows through bridges with potential overtopping and for predicting the related backwater effect. Nevertheless, local flow characteristics induced by significant vertical accelerations cannot be accurately reproduced by adopting the 1D approximation.

The particular topological schematization strictly requires that the bridge or culvert is discretized by at least 3 computational cells. The possibility of discretizing the crossing structure with a high number of computational cells makes the model effective in predicting the main features of the flow in detail, especially in the case of long culverts.

Although simple geometrical configurations were considered in all tests presented, the application of the model can be easily extended to cross-sectional

shapes other than rectangular, and even to non-prismatic channels, provided that the characteristic equations are re-written for the given geometry and that the head losses caused by contractions at the bridge/culvert inlet and expansions at the outlet are reasonably taken into account. The pressurized flow potentially occurring under the bridge/culvert was modelled by the classical Preissmann slot method, but alternative methods recently presented in the literature (such as the Two Pressure Approach and the dual model) can be used as well. Finally, the occurrence of pressurized flow restricts the allowable computational time step due to the stability condition, as already discussed in Chapter 2. The efficiency of the model can be improved if a local time stepping strategy is implemented in the scheme.

Conclusions

A number of different approaches to model mixed flows are available in the literature, two of which have been analyzed at the beginning of this work, in particular the classic Preissmann slot approach and the more recent dual model. Both models are governed by hyperbolic equations, which are discretized by means of a first-order accurate finite volume scheme. The simulation of an experimental test case confirmed that well-known post-shock oscillations originate at flow regime transitions when shock-capturing schemes are adopted. The comparison showed that both models are able to predict the main features of the flow dynamics correctly, despite the low pressure wave celerity assumed to minimize these spurious oscillations. However, due to its greater simplicity, the Preissmann slot model was preferred in the following development of this work, which addressed some issues related to the numerical modelling of mixed flows, not previously taken into consideration in the literature.

The coexistence of markedly different celerity values which characterizes the simultaneous occurrence of free-surface and pressurized flow also restricts the computational efficiency if explicit schemes are used, due to the CFL stability condition. In order to address this problem, the finite volume numerical scheme used to discretized the governing equations of the Preissmann slot model was coupled with a local time stepping strategy. The comparison with the conventional

global time stepping strategy, performed on the basis of different idealized and experimental tests, showed that the LTS speeds up the computations with a factor ranging between 1.4 and 6.5, without impairing overall solution accuracy and without deteriorating mass conservation. The speed-up factor is found to increase when the value of pressure wave celerity increases, and also when the percentage of pressurized cells in the domain is reduced, thus suggesting the suitability of this strategy for those applications where only a small region of the domain is surcharged.

The second part of the thesis focused on the integration of potentially pressurized hydraulic structures, i.e. bridges and culverts, in otherwise totally open channel domains. A 2D extension of the Preissmann slot model was proposed, so that transitions between free-surface and pressurized flow can be handled in a natural and straightforward way through an adaptation of the classic formulation of the shallow water equations with the addition of two orthogonal narrow slots above the ceiling of each computational cell. The results of numerical simulations of idealized tests and of cases involving partially pressurized arch bridges showed that the proposed model is suitable for the prediction of highly transient 2D mixed flows.

However, bridges and culverts might be overtopped for extreme events, and the 2D mixed flow model here presented cannot account for this possibility. Hence, this work also proposed a 1D model which allows for bridge/culvert overtopping by introducing internal boundary conditions at the upstream and downstream ends of the hydraulic structure considered. The Preissmann slot approach was used to model the flow under the deck, thus allowing its detailed simulation (and possibly the presence of flow regime transitions), which is particularly important in the case of long culverts. The model was validated by comparison not only with experimental data, but also with the results of numerical simulations performed with the widespread software HEC-RAS. The agreement between the results of

these two models showed that the IBC model can be a useful and effective tool for predicting overtopping and backwater effects related to the presence of bridges and culverts. At present, the IBC strategy is only implemented for a 1D geometry, but the integration of a similar strategy in a 2D shallow water model could extend its predictive capabilities in the case of the presence of hydraulic crossing structures in the flow field.

The presence of a small pressurized region in a wide open channel domain may increase the computational time prohibitively for real-field simulations. This is true for both the 2D Preissmann slot model and the 1D IBC model. The implementation of the local time stepping strategy in these schemes is an essential requirement for making these numerical tools effectively exploitable in the practice, and represents the most important future development of this work.

References

Alcrudo, F. and García-Navarro, P. (1993). A high-resolution Godunov-type scheme in finite volumes for the 2D shallow-water equations. *International Journal for Numerical Methods in Fluids* 16 (6), 489–505.

Aureli, F., Dazzi, S., Maranzoni, A., and Mignosa, P. (2015). Validation of single- and two-equation models for transient mixed flows: a laboratory test case. *Journal of Hydraulic Research* 53 (4), 440–451.

Aureli, F., Maranzoni, A., Mignosa, P., and Ziveri, C. (2008). A weighted surface-depth gradient method for the numerical integration of the 2D shallow water equations with topography. *Advances in Water Resources* 31 (7), 962–974.

Bashiri Atrabi, H., Hosoda, T., and Shirai, H. (2015). A two-dimensional depth averaged model for mixed flows simulations. *Proceedings of the 36th IAHR World Congress*. The Hague, The Netherlands.

Berger, M. J. and LeVeque, R. J. (1998). Adaptive mesh refinement using wave-propagation algorithms for hyperbolic systems. *SIAM Journal of Numerical Analysis* 35 (6), 2298–2316.

Biery, P. F. and Delleur, J. W. (1962). Hydraulics of single span arch bridge constrictions. *Journal of the Hydraulic Division* 88 (2), 75–108.

Bourdarias, C. and Gerbi, S. (2007). A finite volume scheme for a model coupling free surface and pressurized flows in pipes. *Journal of Computational and Applied Mathematics* 209 (1), 109–131.

Bousso, S., Daynou, M., and Fuamba, M. (2013). Numerical modeling of mixed flows in storm water systems: Critical review of literature. *Journal of Hydraulic Engineering* 139 (4), 385–396.

Capart, H., Sillen, X., and Zech, Y. (1997). Numerical and experimental water transients in sewer pipes. *Journal of Hydraulic Research* 35 (5), 659–672.

Cardle, J. A., Song, C. C. S., and Yuan, M. (1989). Measurements of mixed transient flows. *Journal of Hydraulic Engineering* 115 (2), 169–182.

Cataño-Lopera, Y. A., Tokyay, T. T., Martin, J. E., Schmidt, A. R., Lanyon, R., Fitzpatrick, K., Scalise, C. F., and García, M. H. (2014). Modeling of a transient event in the Tunnel and Reservoir Plan System in Chicago, Illinois. *Journal of Hydraulic Engineering* 140 (9), 05014005.

Catella, M. and Bechi, G. (2006). Conservative scheme for flow numerical modeling of submerged bridges. *Proceedings of River Flow 2006*. Lisbon, Portugal.

Chosie, C. D., Hatcher, T. M., and Vasconcelos, J. G. (2014). Experimental and numerical investigation on the motion of discrete air pockets in pressurized water flows. *Journal of Hydraulic Engineering* 140 (8), 04014038.

Chow, V. T. (1959). *Open channel hydraulics*. New York, USA: McGraw-Hill Book Company, Inc.

Coquel, F., Nguyen, Q. L., Postel, M., and Tran, Q. H. (2010). Local time stepping applied to implicit-explicit methods for hyperbolic systems. *Multiscale Modeling & Simulation* 8 (2), 540–570.

Cozzolino, L., Cimorelli, L., Covelli, C., Della Morte, R., and Pianese, D. (2015). The analytic solution of the shallow-water equations with partially open sluice-gates: The dam-break problem. *Advances in Water Resources* 80, 90–102.

Crossley, A. J. and Wright, N. G. (2005). Time accurate local time stepping for the unsteady shallow water equations. *International Journal for Numerical Methods in Fluids* 48 (7), 775–799.

Crossley, A. J., Wright, N. G., and Whitlow, C. D. (2003). Local time stepping for modeling open channel flows. *Journal of Hydraulic Engineering* 129 (6), 455–462.

Cunge, J. A., Holly, F. M., and Verwey, A. (1980). *Practical aspects of computational river hydraulics*. London, UK: Pitman.

Cunge, J. A. and Wegner, M. (1964). Intégration numérique des equations d'écoulement de Barré de Saint-Venant par un schéma implicite de différences finies. *La Houille Blanche* 1, 33–39.

Dazzi, S., Maranzoni, A., and Mignosa, P. (2016). Local time stepping applied to mixed flow modelling. *Journal of Hydraulic Research* (in press).

DEFRA (2004). *Afflux at bridges and culverts*. R&D Technical Report W5A-061/TR1. DEFRA & Environment Agency, UK.

DHI (2002). *MOUSE pipe flow reference manual*. Horsolm, Denmark: DHI software.

Dumbser, M. (2014). Arbitrary-Lagrangian-Eulerian ADER-WENO finite volume schemes with time-accurate local time stepping for hyperbolic conservation laws. *Computer Methods in Applied Mechanics and Engineering* 280, 57–83.

Dumbser, M., Käser, M., and Toro, E. F. (2007). An arbitrary high-order Discontinuous Galerkin method for elastic waves on unstructured meshes – V. Local time stepping and p-adaptivity. *Geophysical Journal International* 171 (2), 695–717.

Dumbser, M., Zanotti, O., Hidalgo, A., and Balsara, D. S. (2013). ADER-WENO finite volume schemes with space-time adaptive mesh refinement. *Journal of Computational Physics* 248, 257–286.

Erpicum, S., Kerger, F., Archambeau, P., Dewals, B. J., and Pirotton, M. (2009). Experimental and numerical investigation of mixed flow in a gallery. *Multiphase flow V*. New Forest UK: WIT Press.

Ferreri, G. B., Ciraolo, G., and Lo Re, C. (2014a). Flow hydraulic characteristics determining the occurrence of either smooth or abrupt sewer pressurization. *Journal of Hydraulic Research* 52 (5), 676–683.

Ferreri, G. B., Ciraolo, G., and Lo Re, C. (2014b). Storm sewer pressurization transient – an experimental inverstigation. *Journal of Hydraulic Research* 52 (5), 666–675.

Ferreri, G. B., Freni, G., and Tomaselli, P. (2010). Ability of Preissmann slot scheme to simulate smooth pressurization transient in sewers. *Water Science and Technology* 62 (8), 1848–1858.

FHWA (2012). *Submerged flow bridge scour under clear water conditions*. Report No. FHWA-HRT-12-034. U.S. Department of Transportation.

FLUENT (2011). *Fluent 14.0 User's Guide*. ANSYS Inc.

Fuamba, M. (2002). Contribution on transient flow modelling in storm sewers. *Journal of Hydraulic Research* 40 (6), 685–693.

García-Navarro, P., Alcrudo, F., and Priestley, A. (1994). An implicit method for water flow modelling in channels and pipes. *Journal of Hydraulic Research* 32 (5), 721–742.

Grote, M. J. and Mitkova, T. (2010). Explicit local time-stepping methods for Maxwell's equations. *Journal of Computational and Applied Mathematics* 234 (12), 3283–3302.

Guinot, V. (2000). Riemann solvers for water hammer simulations by Godunov method. *International Journal for Numerical Methods in Engineering* 49 (7), 851–870.

Guo, Q. and Song, C. C. S. (1990). Surging in urban storm drainage systems. *Journal of Hydraulic Engineering* 116 (12), 1523–1537.

Guo, Q. and Song, C. C. S. (1991). Dropshaft hydrodynamics under transient conditions. *Journal of Hydraulic Engineering* 117 (8), 1042–1055.

Hamam, M. A. and McCorquodale, J. A. (1982). Transient conditions in the transition from gravity to surcharged sewer flow. *Canadian Journal of Civil Engineering* 9 (2), 189–196.

HEC (2010). *HEC-RAS, River Analysis System Hydraulic Reference Manual, version 4.1*. Davis, California, USA: U.S. Army Corps of Engineers, Hydrologic Engineering Center.

Hirsch, C. (1990). *Numerical computation of internal and external flows*. Vol. 2. Chichester, UK: Wiley.

Hirt, C. W. and Nichols, B. D. (1981). Volume of fluid (VOF) method for the dynamics of free boundaries. *Journal of Computational Physics* 39 (1), 201–225.

HR Wallingford (1988). *Afflux at arch bridges*. Report SR182. HR Wallingford, UK.

Hwang, Y.-H. and Chung, N.-M. (2002). A fast Godunov method for the water-hammer problem. *International Journal for Numerical Methods in Fluids* 40 (6), 799–819.

Jafaar, H. H. and Merkley, G. P. (2010). High-resolution method for modeling hydraulic regime changes at canal gate structures. *Journal of Irrigation and Drainage Engineering* 136 (12), 795–808.

Kara, S., Stoesser, T., Sturm, T. W., and Mulahasan, S. (2015). Flow dynamics through a submerged bridge opening with overtopping. *Journal of Hydraulic Research* 53 (2), 186–195.

Kerger, F., Archambeau, P., Dewals, B. J., Erpicum, S., and Pirotton, M. (2012). Three-phase bi-layer model for simulating mixed flows. *Journal of Hydraulic Research* 50 (3), 312–319.

Kerger, F., Archambeau, P., Erpicum, S., Dewals, B. J., and Pirotton, M. (2011a). A fast universal solver for 1D continuous and discontinuous steady flows in rivers and pipes. *International Journal for Numerical Methods in Fluids* 66 (1), 38–48.

Kerger, F., Archambeau, P., Erpicum, S., Dewals, B. J., and Pirotton, M. (2011b). An exact Riemann solver and a Godunov scheme for simulating highly transient mixed flows. *Journal of Computational and Applied Mathematics* 235 (8), 2030–2040.

Kesserwani, G. and Liang, Q. (2015). RKDG2 shallow-water solver on non-uniform grids with local time steps: Application to 1D and 2D hydrodynamics. *Applied Mathematical Modelling* 39 (3), 1317–1340.

Kleb, W. L., Batina, J. T., and Williams, M. H. (1992). Temporal adaptive Euler/Navier-Stokes algorithm involving unstructured dynamic meshes. *AIAA Journal* 30 (8), 1980–1985.

Krámer, T. and Józsa, J. (2007). Solution-adaptivity in modelling complex shallow flows. *Computers & Fluids* 36 (3), 562–577.

León, A. S., Ghidaoui, M. S., Schmidt, A. R., and H., García M. (2006). Godunov-type solutions for transient flows in sewers. *Journal of Hydraulic Engineering* 132 (8), 800–813.

León, A. S., Ghidaoui, M. S., Schmidt, A. R., and H., García M. (2008). Efficient second-order accurate shock-capturing scheme for modeling one- and two-phase water hammer flows. *Journal of Hydraulic Engineering* 134 (7), 970–983.

León, A. S., Ghidaoui, M. S., Schmidt, A. R., and H., García M. (2009). Application of Godunov-type schemes to transient mixed flows. *Journal of Hydraulic Research* 47 (2), 147–156.

León, A. S., Ghidaoui, M. S., Schmidt, A. R., and H., García M. (2010). A robust two-equation model for transient-mixed flows. *Journal of Hydraulic Research* 48 (1), 44–56.

León, A. S., Gifford-Miears, C., and Choi, Y. (2013). Well-balanced scheme for modeling open-channel and surcharged flows in steep-slope closed conduit systems. *Journal of Hydraulic Engineering* 139 (4), 374–384.

LeVeque, R. J. (2002). *Finite volume methods for hyperbolic problems*. Cambridge, UK: Cambridge University Press.

Li, J. and McCorquodale, A. (1999). Modeling mixed flow in storm sewers. *Journal of Hydraulic Engineering* 125 (11), 1170–1180.

Liska, R. and Wendroff, B. (1999). Two-dimensional shallow water equations by composite schemes. *International Journal for Numerical Methods in Fluids* 30 (4), 461–479.

Malavasi, S. and Blois, G. (2007). Influence of the free surface on the flow pattern around a rectangular cylinder. *Proceedings of the Ninth International Symposium on Fluid Control, Measurements and Visualization*. Tallahassee, Florida.

Malavasi, S., Franzetti, S., and Macchi, S. (2006). Modellazione del rigurgito provocato da ponti fluviali parzialmente o totalmente sommersi. *Atti del XXX Convegno Nazionale di Idraulica e Costruzioni Idrauliche*. Rome, Italy.

Malavasi, S. and Guadagnini, A. (2003). Hydrodynamic loading on river bridges. *Journal of Hydraulic Engineering* 129 (11), 854–861.

Maleki, F. S. and Khan, A. A. (2016). A novel local time stepping algorithm for shallow water flow simulation in the discontinuous Galerkin framework. *Applied Mathematical Modelling* 40 (1), 70–84.

Malekpour, A. and Karney, B. W. (2015). Spurious numerical oscillations in the Preissmann slot method: origin and suppression. *Journal of Hydraulic Engineering*, 04015060.

Maranzoni, A., Dazzi, S., Aureli, F., and Mignosa, P. (2015). Extension and application of the Preissmann slot model to 2D transient mixed flows. *Advances in Water Resources* 82, 70–82.

Martín-Vide, J. P. and Prió, J. M. (2005). Backwater of arch bridges under free and submerged conditions. *Journal of Hydraulic Research* 43 (5), 515–521.

Morales-Hernández, M., Murillo, J., and García-Navarro, P. (2013). The formulation of internal boundary conditions in unsteady 2D shallow water flows: Application to flood regulation. *Water Resources Research* 49 (1), 471–487.

Moré, J. J., Garbow, B. S., and Hillstrom, K. E. (1980). *User guide for MINPACK-1.* Technical report ANL-80-74. Argonne National Laboratory.

Morel, A. T., Fey, M., and Maurer, J. (1996). *Multidimensional high order method of transport for the shallow water equations.* Research Report No. 96-09. ETH Zurich, Switzerland.

Natale, L., Petaccia, G., and Savi, F. (2004). Mathematical simulation of the effects of bridges and structures on flood waves propagation. *Proceedings of River Flow 2004.* Naples, Italy.

Noto, L. and Tucciarelli, T. (2001). DORA algorithm for network flow models with improved stability and convergence properties. *Journal of Hydraulic Engineering* 127 (5), 380–391.

Osher, S. and Sanders, R. (1983). Numerical approximations to nonlinear conservation laws with locally varying time and space grids. *Mathematics of Computation* 41, 321–336.

Ozmen-Cagatay, H. and Kocaman, S. (2010). Dam-break flows during initial stage using SWE and RANS approaches. *Journal of Hydraulic Research* 48 (5), 603–611.

Pervaiz, M. M. and Baron, J. R. (1988). Temporal and spatial adaptive algorithm for reacting flows. *Communications in Applied Numerical Methods* 4 (1), 97–111.

Picek, T., Havlik, A., Mattas, D., and Mares, K. (2007). Hydraulic calculation of bridges at high water stages. *Journal of Hydraulic Research* 45 (3), 400–406.

Politano, M., Odgaard, A. J., and Klecan, W. (2007). Case study: Numerical evaluation of hydraulic transients in a combined sewer overflow tunnel system. *Journal of Hydraulic Engineering* 133 (10), 1103–1110.

Ratia, H., Murillo, J., and García-Navarro, P. (2014). Numerical modelling of bridges in 2D shallow water flow simulations. *International Journal for Numerical Methods in Fluids* 75 (4), 250–272.

Sanders, B. F. (2008). Integration of a shallow water model with a local time step. *Journal of Hydraulic Research* 46 (4), 466–475.

Sanders, B. F. and Bradford, S. F. (2011). Network implementation of the two-component pressure approach for transient flow in storm sewers. *Journal of Hydraulic Engineering* 137 (2), 158–172.

Seckin, G. (2004). A simple formula for estimating backwater at bridge constrictions. *Canadian Journal of Civil Engineering* 31 (4), 561–568.

Shigematsu, T., Liu, P. L.-F., and Oda, K. (2004). Numerical modeling of the initial stages of dam-break waves. *Journal of Hydraulic Research* 42 (2), 183–195.

Song, C. C. S., Cardle, J. A., and Leung, K. S. (1983). Transient mixed-flow models for storm sewers. *Journal of Hydraulic Engineering* 109 (11), 1487–1504.

Steinebach, G., Rademacher, S., Rentrop, P., and Schulz, M. (2004). Mechanisms of coupling in river flow simulation systems. *Journal of Computational and Applied Mathematics* 168 (1), 459–470.

Syme, W. J., Pinnell, M. G., and Wicks, J. M. (2004). Modeling flood inundation of urban areas in the UK using 2D/1D hydraulic models. *Proceedings of the 8th National Conference on Hydraulics in Water Engineering*. Australia.

Tan, Z., Zhang, Z., Huang, Y., and Tang, T. (2004). Moving mesh methods with locally varying time steps. *Journal of Computational Physics* 200 (1), 347–367.

Toro, E. F. (1999). *Riemann solvers and numerical methods for fluid dynamics*. Berlin, Germany: Springer.

Toro, E. F. (2001). *Shock-capturing methods for free-surface shallow flows*. Chichester, UK: Wiley.

Trahan, C. J. and Dawson, C. (2012). Local time-stepping in Runge-Kutta discontinuous Galerkin finite element methods applied to the shallow-water equations. *Computer Methods in Applied Mechanics and Engineering* 217, 139–152.

Trajkovic, B., Ivetic, M., Calomino, F., and D'Ippolito, A. (1999). Investigation of transition from free surface to pressurized flow in a circular pipe. *Water Science and Technology* 39 (9), 105–112.

Trindade, B. C. and Vasconcelos, J. G. (2013). Modeling of water pipeline filling events accounting for air phase interactions. *Journal of Hydraulic Engineering* 139 (9), 921–934.

Van Leer, B. (1974). Towards the ultimate conservative difference scheme. II. Monotonicity and conservation combined in a second-order scheme. *Journal of Computational Physics* 14 (4), 361–370.

Van Nam, N., Erpicum, S., Dewals, B. J., Pirotton, M., and Archambeau, P. (2012). Experimental investigations of 2D stationary mixed flows and numerical comparison. *Proceedings of the 2nd IAHR Europe Congress*. Munich, Germany.

Vasconcelos, J. G., Klaver, P. R., and Lautenbach, D. J. (2015). Flow regime transition simulation incorporating entrapped air pocket effects. *Urban Water Journal* 12 (6), 488–501.

Vasconcelos, J. G. and Marwell, D. T. B. (2011). Innovative simulation of unsteady low-pressure flows in water mains. *Journal of Hydraulic Engineering* 137 (11), 1490–1499.

Vasconcelos, J. G. and Wright, S. J. (2005). Experimental investigation of surges in a stormwater storage tunnel. *Journal of Hydraulic Engineering* 131 (10), 853–861.

Vasconcelos, J. G. and Wright, S. J. (2007). Comparison between the two-component pressure approach and current transient flow solvers. *Journal of Hydraulic Research* 45 (2), 178–187.

Vasconcelos, J. G. and Wright, S. J. (2009). Investigation of rapid filling of poorly ventilated stormwater storage tunnels. *Journal of Hydraulic Research* 47 (5), 547–558.

Vasconcelos, J. G., Wright, S. J., and Roe, P. L. (2006). Improved simulation of flow regime transition in sewers: Two-component pressure approach. *Journal of Hydraulic Engineering* 132 (6), 553–562.

Vasconcelos, J. G., Wright, S. J., and Roe, P. L. (2009). Numerical oscillations in pipe-filling bore predictions by shock-capturing models. *Journal of Hydraulic Engineering* 135 (4), 296–305.

Wiggert, D. C. (1972). Transient flow in free-surface, pressurized systems. *Journal of the Hydraulics Division* 98 (1), 11–27.

Wright, S. J., Vasconcelos, J. G., Creech, C. T., and Lewis, J. W. (2008). Flow regime transition mechanisms in rapidly filling stormwater storage tunnels. *Environmental Fluid Mechanics* 8 (5-6), 605–615.

Zhang, X. D., Trépanier, J. Y., Reggio, M., and Camarero, R. (1994). Time-accurate local time stepping method based on flux updating. *AIAA Journal* 32 (9), 1926–1929.

Zhao, M. and Ghidaoui, M. S. (2004). Godunov-type solutions for water hammer flows. *Journal of Hydraulic Engineering* 130 (4), 341–348.

Zhou, F., Hicks, F. E., and Steffler, P. M. (2002). Transient flow in a rapidly filling horizontal pipe containing trapped air. *Journal of Hydraulic Engineering* 128 (6), 625–634.